POLITECNICO DI TORINO

Collegio di Ingegneria Chimica e dei Materiali

Master of Science Course
in Materials Engineering for Industry 4.0

Master of Science Thesis

Processability of recycled Aluminum alloy powders: A study of secondary AlSi10Mg and AlSi9Cu3 powders



Tutors:
prof. Diego G. Manfredi
prof. Marco Actis Grande
.....

.....

Candidate:

Eric Rossetto Stella

Settembre 2026

ABSTRACT

This thesis project was conducted in collaboration with the PoliTO Interdepartmental Center for Integrated Additive Manufacturing (IAM@PoliTo) and the Department of Chemistry of the Università degli Studi di Torino (UNITO).

Throughout the last decades, the request for high-performance Aluminum alloys has increased in tune with the growth of all industrial sectors around the Globe.
Despite its high recyclability, aluminum alloys suffer an important loss in mechanical properties after conventional recycling techniques (such as High Pressure Die Casting): recycled materials tend to introduce substantial amounts of impurities inside their composition which must be considered, since they could lead to the nucleation and growth of intermetallic compounds that could be detrimental inside the alloy, thus leading to a potential drop in the performance and mechanical properties of the final product.
At the same time, the production of primary aluminum brings high amounts of pollution and energy expenditure, making it an ineffective choice for most modern mass production lines.
For these reasons, in the last few years there has been an increase in interest in alternative recycling methods for aluminum alloys, especially in regards of advanced manufacturing techniques such as Additive Manufacturing (AM), with the final aim of reducing the loss in performance of the recycled material.

The aim of this thesis paper was to evaluate the feasibility of an AM technique, namely Laser Powder Bed Fusion (L-PBF), in using two different aluminum alloys from secondary metallurgy: an ingot made of AlSi10Mg alloy and a discarded automotive component made inAlSi9Cu3 alloy.
One of the main focuses of this study was to verify the use of both alloys in an AM powder-based supply chain. Firstly, they were produced in powders by gas atomization in the Alessandria campus of the Politecnico di Torino; the powders were characterized in terms of shape, mean size distribution and chemical composition by laser granulometry, Scanning Electron Microscopy (SEM) and X-Ray Diffraction (XRD). After that they were processed through L-PBF to obtain samples microstructurally characterized by optical microscopy to evaluate residual porosity, by XRD and by Field Emission SEM (FE-SEM) equipped with EDS and EBSD detectors, to evaluate the phases and their grain size and morphology. The XRD, EDS and EBSD analyses were conducted in collaboration with a research team of the Department of Chemistry of the Università degli Studi di Torino, led by Professor Alberto Castellero.
Finally, the mechanical behavior of the L-PBF secondary alloys was assessed by microhardness tests. alloys, their microstructure and their chemical composition at the end of the production process.

Table of Contents

Abstract
Abbreviations
1 INTRODUCTION
1.1 Aluminum Alloys and their market
1.2 Aluminum
1.3 Aluminum Alloys classifications
1.3.1 ASTM
1.3.2 UNI
1.3.2.1 Alphanumeric designation
1.3.2.2 Chemical symbols designation
1.4 Primary aluminum alloys
1.5 Secondary aluminum alloys
1.6 Al-Si alloys: typical alloyants and their behavior
1.6.1 Defects in Al-Si casting alloy
1.6.2 Intermetallic phases in cast Al-Si alloys
1.6.2.1 α-Fe intermetallic compounds
1.6.2.2 β-Fe and δ-Fe phases
1.6.2.3 π-Fe phases
1.6.2.4 θ-Al_2Cu and Q-phase
1.7 Solidification speed and the impact on Al -Si microstructure
1.7.1 Si morphology
1.7.2 α-Al morphology
1.7.3 Intermetallic phases morphology
1.8 Gas Atomization: a brief overview
1.8.1 Defects in Gas-Atomized powders
1.9 Laser Powder Bed Fusion (L-PBF)
1.9.1 Defects in AM components
2 AIMS OF THE STUDY
3 MATERIALS AND METHODS
3.1 Alloy feedstock
3.1.1 AlSi10Mg
3.1.2 AlSi9Cu3
3.2 Atomization and additional sieving
3.2.1 AlSi10Mg
3.2.2 AlSi9Cu3
3.3 Further Powder characterizations
3.4 L-PBF
3.4.1 Printed Sample Preparation
3.4.2 Microstructural analysis
3.4.2.1 Optical Analysis, Porosity
3.4.3 XRD Analysis
3.4.4 FE-SEM
3.4.5 Mechanical analysis: microhardness
4 RESULTS AND DISCUSSION
4.1 Powder Analysis
4.1.1 PSD
4.1.1.1 AlSi10Mg

4.1.1.2 AlSi9Cu3
4.1.2 SEM-EDS analysis
4.1.3 Rheological tests
4.1.4 XRD Analysis
4.2 Printed components
4.2.1 Microstructural analysis
4.2.1.1 Optical Analysis, Porosity: AlSi10Mg
4.2.1.2 Optical Analysis, Porosity: AlSi9Cu3
4.2.2 XRD Analysis
4.2.3 FE-SEM
4.2.3.1 EDS
4.2.3.2 EBSD
4.2.4 Mechanical analysis: microhardness
5 CONCLUSIONS
6 FUTURE DEVELOPMENTS
7 REFERENCES

Abbreviations

AA	Aluminum Association
AM	Additive Manufacturing
ASTM	American Society for Testing and Materials
BFE	Basic Flowability Energy
BJT	Binder Jetting
BSD	Backscatter Detector
CBD	Conditioned Bulk Density
DFSC	Differential Fast Scanning Calorimetry
DISAT	Dipartimento Scienza Applicata e Tecnologia
DTA	Differential Thermal Analysis
EBM	Electron Beam Powder Bed Fusion
EBSD	Electron Backscatter Diffraction
EDX /EDS	Energy Dispersive X-Rays
EELS	Electron Energy Loss Spectroscopy
EN	European Standard
FD	Feret Diameter
FEG	Field Emission Gun
FCC	Face-centered Cubic (cell)
FRI	Flow Rate Index
GHG	Greenhouse Gasses
GC/ GDC	Gravity Casting/ Gravity Die Casting
GSC	Gravity Sand Casting
HAGB	High Angle Grain Boundary
HIP	Hot Isostatic Pressing
HP	Hard Points
HPDC	High Pressure Die Casting
HV	Vickers Microhardness
IAM	Integrated Additive Manufacturing
ICDD	International Centre for Diffraction Data
LAGB	Low Angle Grain Boundary
L-PBF	Laser Power Bed Fusion
MFD	Maximum Feret Diameter
MIM	Metal Injection Molding
MP	Melt Pool
NIH	National Institutes of Health
OM	Optical Microscope
POLITO	Politecnico di Torino
PSD	Particle size distribution
RSD	Relative Standard Deviation
SALEMA	Substitution of Critical Raw Materials on Aluminum Alloys for electrical vehicles
SD	Standard Deviation
SDAS	Secondary Dendrite Arm Spacing
SEM	Scanning Electron Microscope
SE	Secondary Electrons OR Specific Energy
SI	Industry Standard (according to the AA) OR Stability Index
SSSS	Super Saturated Solid Solution
UNI	Ente Nazionale Italiano di Unificazione
UNITO	Università degli Studi di Torino
UTS	Ultimate Tensile Strength
VIGA	Vacuum inert gas atomizer
WDS	Dispersive X-ray Spectroscopy
XRD	X-Ray Diffraction
%CV	Relative Standard Deviation

1 INTRODUCTION

1.1 Aluminum Alloys and their market

Aluminum alloys are commonly found in most mechanical industries, spanning from Civil Constructions to the Aircraft Industry: the main field of use that will be referenced throughout this thesis will be the Automotive Sector. [1,2]

Aluminum alloys have been in use in the Automotive Industry for over a century: despite steel being in general more easily shaped and formed than wrought and cast aluminum alloys, the constant legislative push for weight reduction and higher fuel efficiency has steered the main automotive manufacturers towards lighter alloys.
Aluminum cast alloys are widely employed in modern automotive manufacturing, since they allow significant benefits towards both the reduction of weight-related pollution and performance enhancements: their density is only about one third of steel and particularly high strength aluminum alloys, based on both composition and thermal treatments, can satisfy the torsion and stiffness requirements of an automotive component. These materials also exhibit excellent resistance towards corrosion, excellent electrical and thermal conductivity, as well as considerable malleability.
However, it is also true that aluminum raw materials are more expensive than steel's: this is one of the main reasons that lead aluminum to be thought of as a solution solely in the premium segment of Automotive Manufacturing for several decades, at least before the current millennium. [2]

The three primary classes of aluminum alloys that are employed in the Automotive Industry are as follows:

• **Aluminum-Copper alloys**: these are mainly used for high-strength applications, like tension elements. Such alloys can offer superior mechanical properties after heat treating, thanks to their high Cu content.

• **Aluminum-Magnesium alloys:** they can offer high corrosion resistance paired with high ductility; they're employed in structural components, cast wheels, and chassis elements.

• **Aluminum-Silicon alloys**: this class of alloys is characterized by high thermal conductivity, good wear resistance and good castability; they are mainly chosen to cast engine blocks, cylinder heads and transmission cases. They're sometimes alloyed with elements such as Cu and Mg, rendering them heat-treatable and suitable for higher mechanical stress. [2,3]

Our study will focus on recycled Aluminum-Silicon alloys.

1.2 Aluminum

Aluminum (Al) is a metal that, in addition to Magnesium and Titanium, is the mainstay of the light alloys group: this category of materials is characterized by lower densities compared to other industrially relevant metals, such as the likes of copper (8.94 g/cm^3) and iron-based alloys (7.83 g/cm^3).
Aluminum alloys can achieve comparable specific properties, such as mechanical resistance, as compared to typical steel alloys while possessing much lower densities (2.70 g/cm^3): for this reason, they find widespread use in numerous industrial sectors, typically for the manufacture of lightweight mechanical components that are employed as replacement to heavier steel or cast-iron parts. [3,4,5]

Aluminum possesses excellent physical properties, especially in regards of both thermal and electrical conductivity (Thermal conductivity, 20-100 °C = 238 W/ m K; Electrical conductivity, 20 °C = 37.7 10^6 S/ m): for these reasons aluminum alloys are widely employed in the production of both thermal apparatuses (like heat sinks, heat exchangers and cooling systems) and electrical appliances (especially electrical cables). [3,5]

At the same time, due to its high thermal conductivity, aluminum alloys deteriorate quickly after being welded: heat propagates rapidly throughout the piece, significantly expanding the heat-affected zone. This problem is also enhanced by the steadfast formation of a surface oxide layer, that impedes welding due to its high melting point.
Cracks may also form afterwards because of the combination between thermal expansion and shrinkage that occur during solidification: since these aluminum alloys tend to have high thermal expansion coefficients, contraction and expansion must be considered during the structural design of mechanical components, especially if large temperature gradients and/or excursion are expected to take place. [3,4]

Al is a reactive species: it's an amphoteric metallic element that easily alloys with other elements in the likes of Cu and Si; Aluminum can also react with non-oxidizing acids, such as hydrochloric (HCl) or phosphoric acid (H_3PO_4), producing aluminum ions.
Aluminum possesses a strongly negative standard reduction potential, which increases its reactivity, especially towards air-bound oxygen. Despite this, aluminum can protect itself thanks to a phenomenon known as surface passivation. [3,5]

Pure Al has almost no industrial application, with the following exceptions:

- Food and pharmaceutical production
- Electrical Industry
- Chemical sector

In these cases, pure aluminum alloys are mainly used for capacitors, containers and heat exchangers.

Aluminum is commonly alloyed with other secondary elements such as Copper (Cu), Manganese (Mn), Silicon (Si), Magnesium (Mg), and Zinc (Zn); furthermore, aluminum alloys can contain impurities in the range of 0.15 wt.%. [4,5]
The mechanical, physical, and chemical properties of Al alloys vary wildly in accordance with their composition and manufacture; the Al -Si class will be further discussed in Chapter 1.6.

1.3 Aluminum alloys classifications

Aluminum alloys are classified under different industry standards based on both their composition and any applied heat treatment: the most employed designations for these alloys are the Aluminum Association (AA; United States classification, branched of the ASTM set of regulations) designation and the European designation (EN, which are a branch of the UNI set of industry regulations); Table 1 showcases a comparison between the two systems.

Table 1 - Comparison between the main EN and AA aluminum classes. [4,5]

EN (European)		**Aluminium Association (American)**	
1xxxx	> 99,50% Aluminium	*1xx.x*	> 99 % Aluminium
2xxxx	Al-Cu	*2xx.x*	Al-Cu
4xxxx	Al-Si / Al-Si-Cu / Al-Si-Mg	*3xx.x*	Al-Si-Cu / Al-Si-Mg
5xxxx	Al-Mg	*4xx.x*	Al-Si
7xxxx	Al-Zn-Mg	*5xx.x*	Al-Mg
8xxxx	Others (Al-Mg-Fe, Al-Li-Cu)	*7xx.x*	Al-Zn
9xxxx	Experimental	*8xx.x*	Al-Sn
		9xx.x	Others

1.3.1 ASTM

The ASTM standard(s) defines two main categories of aluminum alloys, each characterized by their main processing operations: these are wrought alloys and cast alloys.
The Aluminum Association (AA) system developed a different nomenclature for each category, in which the wrought ones are described by a four-digit system while the cast ones by a three-digit system followed by a decimal value. One has also to consider that in several cases commonplace commercial names are used in addition to the alloy's official denominations.

In the following Table a breakdown of both categories' nomenclature is showcased.

Table 2 - Classification of wrought (a) and cast (b) Al alloys given by the Aluminum Association according to their composition.[5]

Series for wrought alloys

1xxx	*Pure Al, ≥ 99.00%*
2xxx	*Cu as principal alloying element, other elements such as Mg may be specified*
3xxx	*Mn as principal alloying element*
4xxx	*Si as principal alloying element*
5xxx	*Mg as principal alloying element*
6xxx	*Mg and Si as principal alloying elements*
7xxx	*Zn as principal alloying element, other elements such as Cu, Mg, Cr, Zr may be specified*
8xxx	*Miscellaneous composition: may contain Sn, Li and Fe*
9xxx	*Reserved for future use*

(a)

Series for cast alloys

1xx.x	*Pure Al, ≥ 99.00%.*
2xx.x	*Cu as principal alloying element, other elements may be specified.*
3xx.x	*Si as principal alloying element, other elements such as Cu and Mg may be specified*
4xx.x	*Si as principal alloying element.*
5xx.x	*Mg as principal alloying element.*
6xx.x	*Unused series.*
7xx.x	*Zn as principal alloying element, other elements such as Cu, Mg may be specified.*
8xx.x	*Sn as principal alloying element*
9xx.x	*Other elements.*

(b)

In regards of heat treatments, the AA system employs a mixed number-and-letter system that is added after the alloys name to codify both the mechanical properties and the process through which they've been achieved.
The generic description of the alloy's treatment is indicated by the first letter in the code: H refers to a cold-worked alloy, while T describes a Heat-treated alloy. Other letters may be employed for light treatments or untreated alloys (see Figure 1).

F - As fabricated.

O - Annealed to obtain the minimum resistance to deformation. Wrought product only.

H - Cold-worked. Strain hardened to obtain specific mechanical characteristics for non-heat treatable alloys.

T - Heat treated (stable). Alloys that have undergone a solution heat treatment and aging to achieve the desired mechanical characteristics.

Figure 1- Heat treatment, ASTM code [5]

Figure 2 showcases a brief breakdown of the meaning behind the second part of the code: these numbers indicate the specific treatment the alloy underwent.

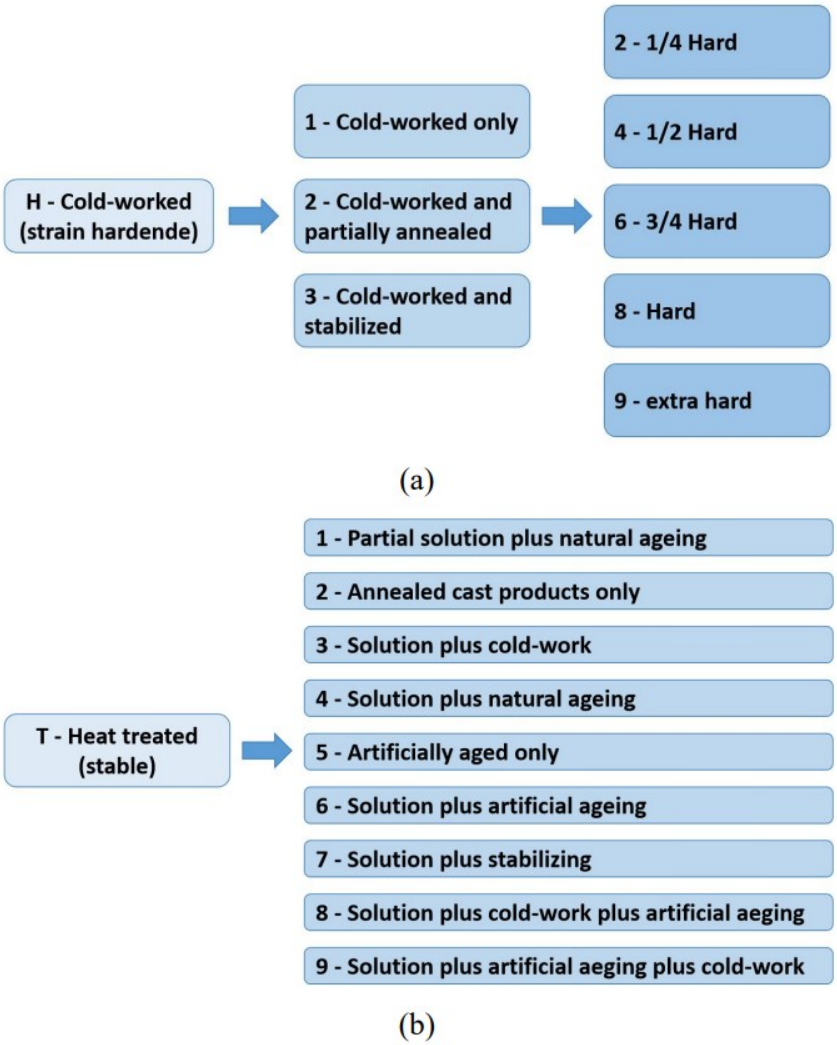


Figure 2 - Specific treatment, ASTM code [5]

1.3.2 UNI

The UNI standard naming system is commonly used in the description of commercial alloys for the industrial sector. There are 4 subcategories:

- EN 573-1 and 1780-1 standards (based on an alphanumeric designation)
- EN 573-2 and 1780-2 standards (based on chemical symbols).

1.3.2.1 Alphanumeric designation

The EN 573-1 code is employed for wrought alloys, while the EN 1780-1 is applied to foundry alloys: both designations use a simple code composed by letters and numbers to describe the specific alloy [5]. See Figure 3 for an example of the EN 573-1 standard.

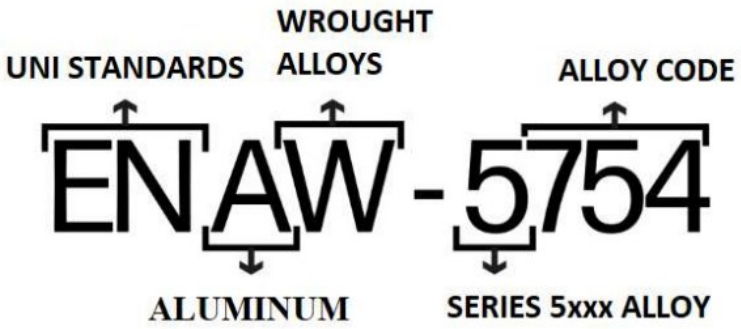


Figure 3 – Example of EN 573-1 standards alphanumeric designation [4]

The "EN" indicates the UNI reference standard. The following letter, A, indicates the base metal of our alloy (in this case aluminum), and the second letter indicates the production process for which that specific alloy is intended:

- **W** - Indicates plastic processing (all these alloys are listed in UNI EN 573-1).
- **B** - Indicates a foundry alloy used for remelting ingots.
- **C** - Indicates a foundry alloy intended for castings.
- **M** - Indicates a foundry alloy intended for master alloys (All foundry alloys are listed in UNI EN 1780-1).

The following characters possess different meanings depending on the production type of the alloy: for wrought alloys, the numerical code that defines the specific alloy is composed of 4 digits; the first number defines the series to which the alloy belongs to and corresponds to the ASTM classification (Table 1), while the remaining numbers indicate the code of the specific alloy.
With foundry alloys (EN AB, EN AC, and EN AM alloys) the applied principle is the same, with the only difference that the numeric code will be made up of 5 digits. The coding follows that of the ASTM classification but with several changes: the 3xx.x and 4xx.x series are grouped into a single series (4xxxx), and the 8xx.x is not present.
The series are 1xxxx (pure aluminum, no alloyants), 2xxxx (aluminum copper alloys), 4xxxx (aluminum silicon alloys), 5xxxx (aluminum magnesium alloys) and 7xxxx (aluminum zinc alloys); master alloys (i.e. EN AM alloys) fall instead in the 9xxxx series. [4,5]

The alloys that will be studied throughout this thesis are foundry alloys EN AC-43400 (AlSi10Mg(Fe)) and EN AC-46000 (AlSi9Cu3(Fe)).

1.3.2.2 Chemical symbols designation

These standards, EN 573-2 (for wrought alloys) and EN 1780-2 (for foundry alloys) rely upon chemical symbols to produce simple codes composed of letters and numbers that define the specific alloy. In Figure 4 an example of this designation is shown.

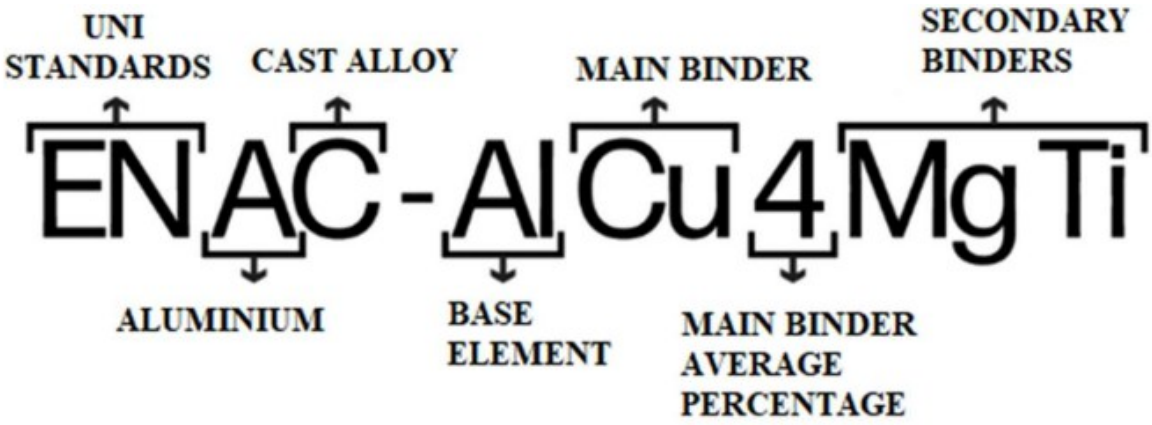


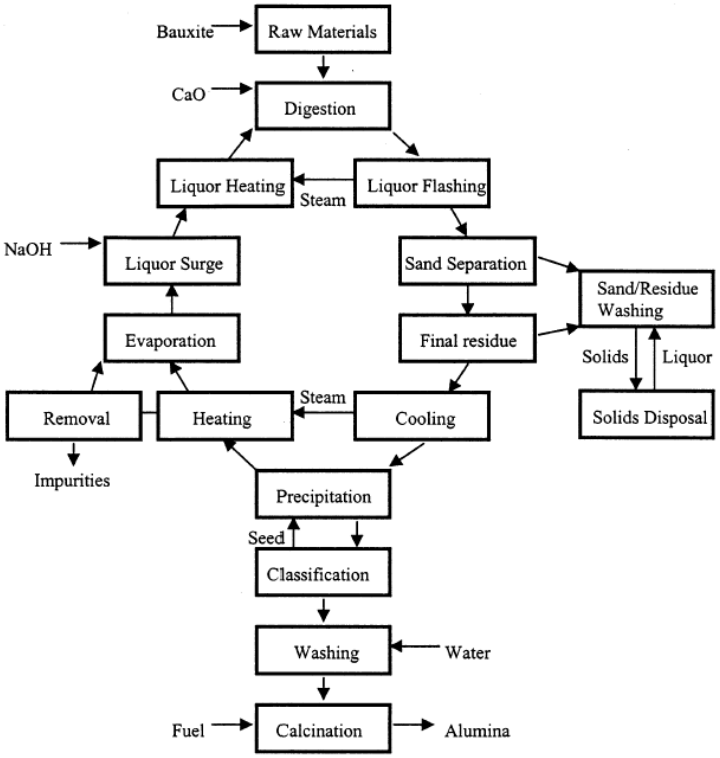
Figure 4 - Example of EN 1780-2 standards chemical symbols designation [4]

In regards of pure aluminum, it is described only by the percentage of its purity (i.e.: EN AB-Al 99.55 indicates 99.55 wt.% pure aluminum).
Since with aluminum chemical composition is not enough to know its mechanical characteristics, knowledge of the production processes the material has undergone is necessary to describe it correctly. Thus, the EN 515 and EN 1706 standards were created to define the complete state of the material.
These standards are in addition to the UNI standard naming systems and employ a code similar to what was previously used in the AA system for heat treatments (F, O, H, and T). There is also the W, which indicates a not aged solubilized material, which in an unstable state.
After the letter, an additional numeric defines the specific treatments and processes undergone by the specific material. The correlation between the numbers and the processes is indicated within the UNI standards tables. [4,5]

Finally, aluminum alloys are also classified based upon the origin of the material as either primary or secondary alloys (derived from recycled materials). [4]

1.4 Primary aluminum alloys

Primary alloys are manufactured from either newly mined/refined ores or pure metals. They may be combined with alloyants in order to reach a determined composition.
Despite being the third most abundant element (after oxygen and silicon) on planet Earth, constituting about 8% of the Earth's crust by weight, its content in most of the minerals is low. This is one of several setbacks behind the production of primary aluminum. [4,6]
The main primary production process for aluminum is given by the combination of the Bayer and Hall-Hérault processes, through which bauxite ores are employed to produce alumina (Al_2O_3) which in turn is used to produce aluminum.



Graph 1 - General scheme of the Bayer process [7]

The Bayer process was developed by Austro-Hungarian chemist Karl Bayer in 1888: it allows the direct synthesis of Al_2O_3 from bauxite ore (see Graph 1).
This procedure involves a complex chain of chemical reactions and physical separations that necessitate both a high number of chemical reagents and an elevated energy expenditure.
The process itself is very efficient, since it has a high yield of Al_2O_3, but it leads to the production of a high amount of a byproduct known as "red mud": this muddy mixture is composed mainly of iron oxides (which give it the typical reddish color) and also contains silica, titanium oxides, and heavy metals traces. This sludge is difficult to recycle/dispose of and its improper storage can easily cause significant environmental damage: this is due to its highly alkaline pH and the fact that, in the event of spills, it can seriously alter the normal chemical balance (especially considering the heavy metal content) of water and soil, thus destroying the local fauna and flora and representing a risk to human health.
Considering the hazardousness of red mud, its correct disposal represents one of the most important infrastructural challenges in the primary aluminum industry: safe stowing of the

slag and preventive neutralization processes are required, thus increasing the overall costs of the Bayer process [6,7]. Figure 5 depicts an open-air red mud containment field.



Figure 5 - Red mud near Stade (Germany) [8]

The Hall-Héroult process was developed independently 1886 by American chemist Charles Martin Hall in conjunction with French scientist Paul Héroult. This process employs as a starting material the alumina synthetized through the Bayer process described above and produces pure aluminum, using an electrochemical reduction process (see Figure 6). [9]

The main drawback of the Hall-Hérault process is very energy-intensive nature, thus requiring a significant amount of electricity; this, paired together with the consumption of carbon electrodes, leads to the emission of large quantities of greenhouse gases (GHG), particularly CO_2: primary aluminum production generates about 12–16.5 t of GHG per ton of metal produced. [10]

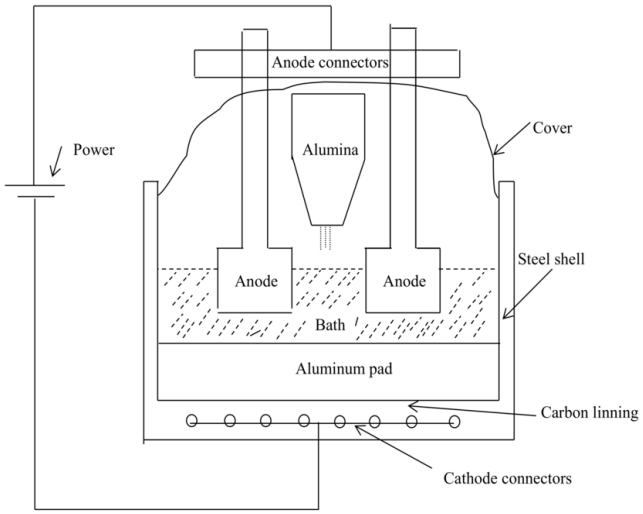


Figure 6 - A simple schematic of a Hall-Hérault cell [9]

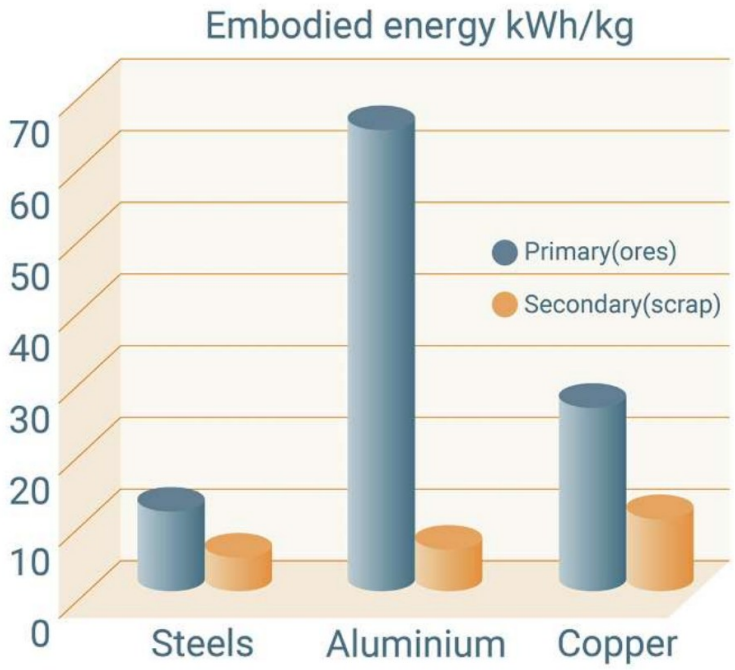
The ingots produced with this process are employed industrially as a pure aluminum base for more complex alloys. [6]

In conclusion, although the Bayer and Hall-Héroult processes historically have led to lowering the production costs of aluminum and have allowed its diffusion and use on a large scale, these processes pose a significant environmental impact.

To bypass both energy consumption and environmental concerns, secondary aluminum alloy production has experienced a surge in growth in the last few decades. [10]

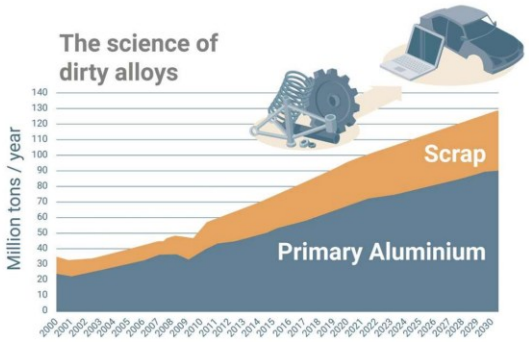
1.5 Secondary aluminum alloys

Secondary aluminum alloys are manufactured using either completely or partially recycled materials: this category of alloys has garnered an increasingly important role in the context of ecological preservation and sustainable, economical and environmentally sound manufacturing.
This class of materials enjoys a sizable energy saving as compared to primary alloys: according to data from the Aluminum Association, recycled aluminum requires up to 95% less of the energy required for primary production. Having such low energy consumption guarantees lower production costs, thus making recycled aluminum alloys palatable for mass manufacturers all around the Globe [11]; see Graph 2 for an energy consumption comparison between several primary and secondary metals.



Graph 2 - Aluminum alloys made entirely from scrap can reduce energy consumption and GHG emissions by > 90% compared to alloys made by primary synthesis [10,14]

Aluminum scrap can be obtained from various sources, such manufacturing offcuts, end-of-life products (such as automotive and aeronautical wrecks), and industrial waste.
Scraps are commonly referred to as “new scrap” if they are production waste, or “old scrap” if they are an end-of-life artifact [12]. The scrap itself is typically collected through recycling programs, from scrap yards and manufacturing facilities. [13]
These alloys use both industrial and commercial scrap as a source of aluminum: according to a study from the International Aluminum Institute, the 2022 yearly global aluminum production reached around 65 million metric tons; of this total, recycled aluminum accounted for 30%. [13]
Graph 3 describes the current trend in aluminum production, comparing yearly primary production to the secondary’s.



Graph 3 - Growth trend of aluminum demand in recent years, and forecasts for the near future [11]

An important fraction of the source materials for these recycled alloys comes directly from both governmental and privately led scrap collection efforts, which have been increasing in land coverage and yearly yield throughout the last decades: in the European Union, for example, the recycling rate for aluminum beverage cans exceeds 75%. [15,16,17]
The recycling processes through which these secondary alloys' base materials are obtained are varied and can be divided into differing categories based on several factors, such as the source of the material, the yield of the final product, and the processes employed.
In the following paragraphs, a description for each of the main categories of these processes is provided.

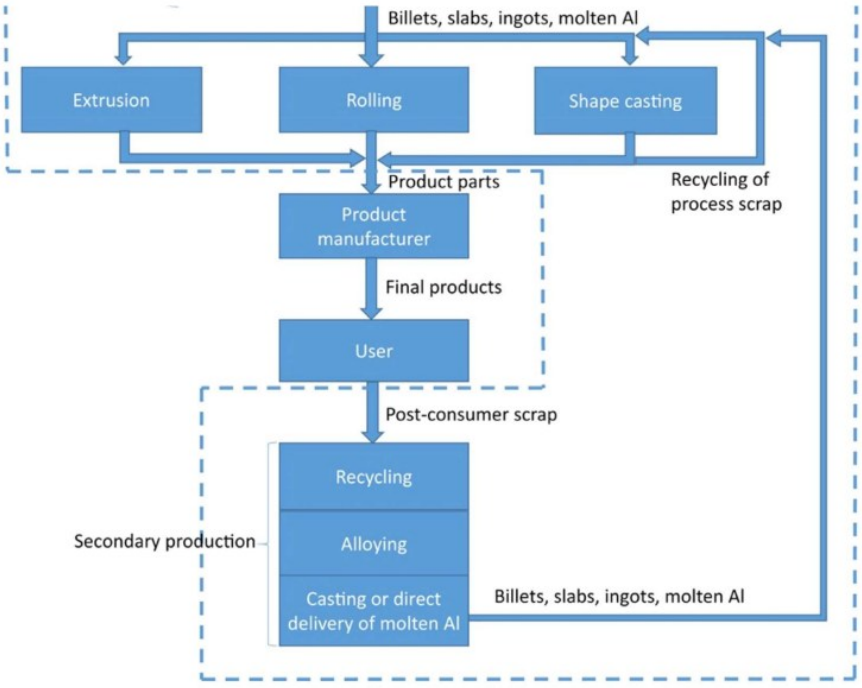


Figure 7 - General scheme of the secondary aluminum production process [5,18]

• **Closed recycling method**: it's a sustainable and efficient production process. The scrap is recycled within the same production process of which it was a byproduct and gets reused for the same original purpose, without a significant loss of quality.
• **Open recycling method**: this process category consists in reusing the material for a purpose other than its original one. This process allows for a convent way to reduce waste since it also allows for the reuse of materials that do not maintain their original properties.

• **Secondary recycling (remelting**): in this process class scrap is employed to produce new alloys, with the addition of alloyants in order to correct the chemical composition. The use of master alloy has a cost and often requires the use of metals obtained from primary sources.
• **Mechanical recycling:** in this case aluminum is recovered through physical means, such as magnetic separation, that doesn't impact the initial chemical composition.
• **Chemical recycling:** this category includes innovative processes that employ chemical compounds to dissolve and recover pure aluminum from waste without altering its properties.
See Figure 7 for a scheme of a typical production process of aluminum secondary alloys. [5]

Despite requiring a lower quantity of energy than primary aluminum, thus being a more economically and environmentally sustainable alternative, secondary aluminum alloys may contain pollutants that can reduce significantly their mechanical performance: the possible presence of these microstructure-modifying impurities is the main drawback of these materials as compared to the primary ones. Thus, the use of recycled Al requires that it must not compromise the properties of the final product, especially at a microstructural level.

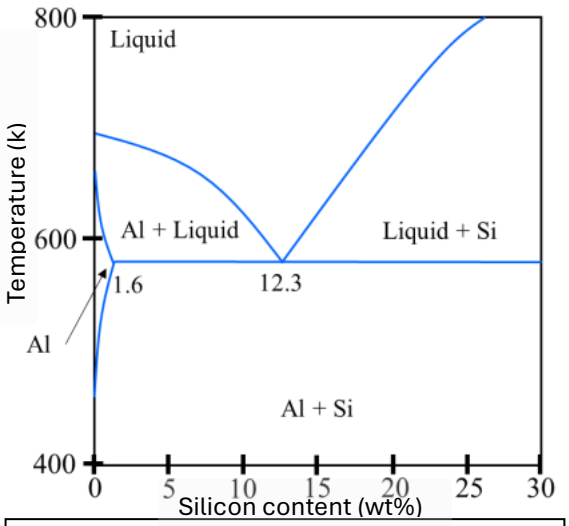
Several studies have been conducted throughout the last few decades with the aim of analyzing the impact of recycled content on the properties of secondary alloys; as part of the European Union's research program "Horizon 2020", the SALEMA ("Substitution of Critical Raw Materials on Aluminum Alloys for electrical vehicles") project ran from 2021 to 2024: the aim of this research was to evaluate the most mechanically efficient, yet cost effective, balance between recycled content and primary content inside a set of aluminum alloys used in the automotive industry [5,19]. SALEMA's highlighted how different percentages of recycled content had different impacts on the component's properties and microstructure, considering traditional secondary aluminum techniques:

- **<40 wt.%:** good compromise between production efficiency and mechanical behavior. The number of inclusions has a slight to none impact on the alloy's properties.
- **Around 60 wt.%: (**most employed percentage used in the automotive industry) the increased content of inclusions and oxides impacts the microstructure, without compromising entirely the alloy's properties.
- **80 wt.%:** high amounts of oxides and inclusions, several criticalities in both the workability and castability of the alloy. Traditional production processes start to be ineffective in coping with the increased number of inclusions.
- **100 wt.%:** the upper limit of recyclability, the logistics behind the stockage of the scraps impact negatively the bottom-line of the production plant; another important factor is the high variability in the composition of the raw materials (scraps), which might lead to a product of uncertain composition, possibly containing great amounts of impurities and unwanted residual substances.

The SALEMA study highlighted that, despite impacting the traditional production processes (melting and casting), the increase in inclusions never represented a major, intolerable impact on the mechanical properties of the recycled alloy.
An important factor to evaluate is the impact of the recycled content on the shape of the eutectic: the SALEMA report showed that an increased content of recycled material caused the eutectic to swell up and distribute itself less homogenously, thus explaining the change in the castability of the alloy.
As previously discussed in chapter 1.3, aluminum alloys are characterized based on their composition class: in the following chapter a more detailed description of the impact of the most common alloyants will be provided, specifically in regards of al -Si alloys.

1.6 Al-Si alloys: typical alloyants and their behavior

Al-Si alloys are the most diffused aluminum cast materials; this class of metal typically contains between 3 and 25 wt.% silicon content and displays a unique set of properties, making it a common choice for automotive applications (such as engine blocks and pistons): they're lightweight, mechanically strong, wear-resistant and thermally stable. [2,3,4]
These alloys are commonly employed as replacements of steel components, especially in the context of fuel-efficiency measures and vehicle design.
Al-Si alloys are employed in both casting and additive manufacturing, and their silicon content characterizes the process' ease and optimal parameters: recent innovations in AM have allowed the production of intricate parts with optimized microstructures, improving overall performance and expanding the fields of potential applications of this class of alloys.



Graph 4 - Portion of the Al-Si phase diagram [20]

In Graph 4 a typical Al-Si phase diagram is showcased: the graph highlights the eutectic point at a concentration of 12.3 wt.% Si.

Al-Si alloys possess a microstructure consisting mainly of a primary α-Al phase, paired with the following phases: [24]

- Primary Silicon (hypereutectic alloys, with a Si content up to 13 wt.%)
- Al-Si eutectic phase
- Cu-rich phases (if Cu is present)
- Mg_2Si phases
- Fe and Mn phases (depending on Fe and Mn content)

The images represented in Figure 8 highlight the microstructure of a massive Al-Si sample.

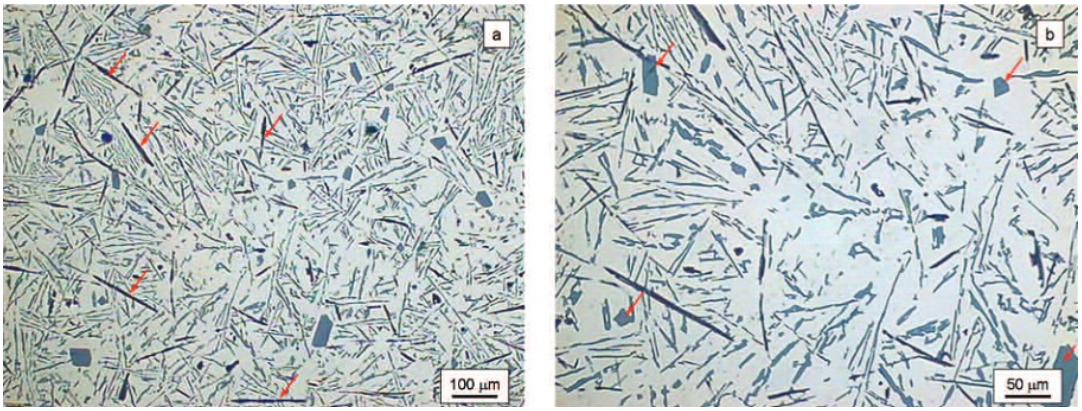


Figure 8 - Microstructure of Al-Si 12 alloy after etching with 0.5 vol%. HF aqueous solution: (a) α-Al primary dendrites. Si-cuboids, eutectic phase and the intermetallic compounds of AlFeSi marked with arrows in the micrograph. The last two features exhibiting an acicular morphology in the plane of sectioning; (b) at higher magnification it is indistinguishable the interphase between the aluminum in the eutectic and that in the dendrites. Primary dendrites are pointed out with arrows. [21]

The aluminum-rich phase α-Al (which forms as face-centered cubic (FCC) cell) is commonly found as part of a eutectic structure, paired together with solid Silicon: both Si and α-Al constitute the typical matrix of the Al-Si alloy, in which the intermetallic particles are distributed throughout. [24]
As mentioned in both Chapters 1.2 and 1.3, pure aluminum possesses much fewer uses than its alloys. Many alloyants are employed industrially, each with different effects on both the microstructure and the properties of the metal; these elements are added either directly as in small quantities during melting or through the use of master alloys: master alloys are employed whenever the added element(s) showcases a slow dissolution rate in the molten aluminum, while direct addition is chosen with elements that possess a lower melting point than Al.
The alloyants can be divided in three classes:

- Major alloying elements: these are elements that characterize the alloy, determining its physical, mechanical and technological properties. These are Cu, Mg, Zn and Ni.
- Minor alloying elements: these elements get added in modest quantities that tend to improve both structural and physical characteristics, with a moderate impact.
- Impurities (Cr, Fe). [24]

In the following paragraphs a brief showcase of each of the main alloyants will be provided, with a focus on their impact on Al-Si alloys: [3,5,6,24]

- **Silicon (Si)**: is the most commonplace alloyant (and, in certain cases, impurity) that's added to aluminum cast alloys. It's a minor alloyant that significantly impacts, depending on its morphology, the tribological behavior of the alloy (wear resistance): its overall effect is also influenced by its particle's distribution, heat treatments and the presence of other alloyants, like copper, magnesium, nickel and zinc.
  Si content must be considered while evaluating the production process at hand: its presence greatly improves the alloy's castability and its ability to fill the die, allowing for the molding of more complex shapes; at the same time, lower Si percentages enhance both the alloy's elongation and ductility.
  Silicon also reduces metal shrinkage during solidification, easing even further the process.
  The Al-Si system showcases a eutectic point at 12.3 wt.% of Si content.

As for the case of Al-Si hypereutectic alloys, and sometimes in eutectic and near eutectic alloys, the first phase to nucleate is primary silicon.
Primary Si takes the form of large polyhedral crystals, which can then flow inside melted alloy since the silicon solubility in the aluminum matrix is negligible.
Afterwards, the Al-Si eutectic phase solidifies. In Al-Si hypoeutectic and eutectic alloys, the first phase to solidify is the α-Al matrix followed by the Al-Si eutectic, which is characterized by a fibrous Silicon shape.
Primary Silicon's geometry is harmful for the alloy as it might act as a concentrator of stress: for this reason, alloyants (like Sr, Na, Ba) and heat treatments are employed in order its morphology.

- **Magnesium (Mg)**: is a major alloyant that's regularly added to improve some mechanical properties, while also improving corrosion resistance: this is due to an increase in affinity with oxygen, allowing for an easier formation of the passivation layer.
  In foundry alloys, Mg is often employed to refine the microstructure, to improve the particle's distribution and to also optimize the mechanical and tribological properties of the material: this is thanks to the precipitation of Mg_2Si, which happens after a T6 heat treatment.
  Despite being a lighter metal, Mg gets added in quantities that don't significantly impact on the alloy's weight.
  This alloyant can improve both the ductility and workability of the alloy, although its presence can be a net negative for the melting process: this is due to the increase in the oxidizability of the alloy, which leads to an increase in oxide inclusion inside the molten metal. Further on, the addition of Mg could cause an increase in porosity (due to the low boiling point of Mg, which might evaporate at high casting temperatures), shrinkage, brittleness (due to the formation of brittle compounds like Al_3Mg_2), possibly lowering the quality of the molten alloy. These negative effects can be greatly reduced by employing lower amounts of the alloyant.

- **Titanium (Ti)**: is a minor alloyant that's added to improve mechanical behavior, thermal stability and wear resistance. One of its main purposes in foundry alloys is as a grain refiner, since it allows for greater homogeneity of the microstructure and an increase in mechanical resistance without negatively impacting ductility. The formation of intermetallic compounds, such as Al_3Ti, helps with the formation of smaller grains; this helps with an increase in tensile strength.
  With components that are subjected to cyclic loads, Ti helps in hindering crack propagation.
  Titanium helps in improving oxidation and corrosion resistance, by enabling the formation of stable titanium oxides on the component's surface.

- **Copper (Cu)**: as an alloyant has a much higher solubility in Al, as compared to SI. It helps with high-temperature mechanical resistance and hardness performance, thanks to the formation of coherent reinforcing precipitates that hinder the movement of dislocations inside the alloy's matrix (i.e. Al_2Cu and $Al_5Cu_2Mg_8Si_6$).
  Cu helps with castability, due to its lower affinity with oxygen (less slag), and impacts workability: the presence of high amounts of copper in alloy leads to higher force requirements in the shaping process, leading to a loss in surface uniformity.
  Homogenous distribution of the precipitates helps with increasing fatigue resistance, leading therefore to higher performances for high cyclic stresses.

Copper impacts corrosion resistance negatively; to compensate for this problem other alloyants are often added, like Mn, coupled with specific surface heat treatments.

- **Nickel (Ni)**: as a major alloyant, nickel helps with the formation of several stable intermetallic phases (like Al_3Ni, Al_3CuNi, and Al_7Cu_4Ni); these compounds allow for an improvement in high-temperature mechanical resistances of the alloy. Their presence is not always preferrable though, as they might act as corrosion trigger points.
  Ni impacts microstructural stability, thanks to the inhibition of grain growth during heat treatments; this behavior helps directly with fatigue resistance.
  Nickel also leads to an improvement in wear resistance and surface hardness of the metal, thus leading to both suitability towards prolonged high stress and high temperature use, while also negatively impacting mechanical processing (by increasing brittleness).
  Ductility and workability are negatively affected, especially if Ni is paired with a high percentage of Cu: despite this fact, nickel is usually a complementary alloyant to copper.

- **Calcium (Ca)**: it's a minor alloyant that's often employed as a microstructure modifier; it allows for a reduction in grain size paired with the formation of intermetallic precipitates, like Al_4Ca and Al_2Ca, which help in improving the alloy's mechanical resistance.
  Calcium can inhibit the eutectic phases' formation inside the grain boundaries by both increasing the elastic limit of the alloy and its corrosion resistance.
  An excess of Ca can lead to the formation of brittle phases that negatively impact both ductility and workability.

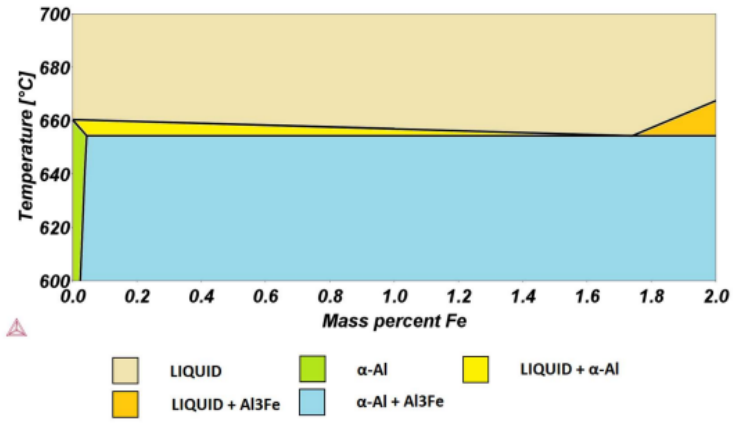
- **Strontium (Sr)**: as an alloyant, strontium modifies directly the eutectic Si form from a coarse plate structure to fine and fibrous structure; this leads to an improvement to both mechanical behavior and the alloy's ductility. This happens because Sr aggregates within the eutectic Si structure, modifying its crystallographic growth behavior, thus leading to greater fatigue resistance and greater microstructural stability over time; all in all, these factors lead to higher alloy toughness and less crack propagation under cyclic stresses.
  Excessive strontium leads to the formation of intermetallic compounds which may act as "hard points" (HP), that can damage the alloy's workability. [24]

- **Manganese (Mn)**: is an alloyant that can improve the alloy's mechanical properties, its corrosion resistance and microstructural stability. It's capable of inhibiting the formation of brittle ferrous intermetallic phases (like β-AlFe), favoring the formation of
  the less harmful specie α-AlFeMnSi (Chinese-script intermetallics).
  Limiting the formation of β phases helps with improving the alloy's performance, more specifically by increasing the yield and tensile strength without modifying its ductility/workability.
  Intermetallic phases containing manganese are thus used to reinforce the alloy's matrix, mainly by enhancing its wear resistance and reducing the propagation of fatigue cracks; manganese additions also enhance the alloy's hardness and tensile strength.

Mn leads to improvements in the alloy's thermal stability, enhancing welding processes and prolonged thermal exposure by preventing microstructural degradation. [24]
Excessive use can lead to problems in traditional metallurgy: when typical secondary cast alloys containing Fe are tried to be corrected with manganese, a new problem arises due to the so called "sludge formation", meaning large intermetallic particles which may form at early stages in the casting process and influence the mechanical properties crucially. [22]

- **Chromium (Cr)**: it's considered an impurity for aluminum alloys.
  Cr influences the phases' distribution inside the metal matrix, thus modifying the alloy's hardness and microstructure.
  High amounts of chromium lead to a sharp decrease in ductility; it also impacts on the alloy's corrosion resistance, by enabling the formation of passive surface films.
  In addition, if paired with Mn and Mo, it promotes the formation of the α-AlFeMnSi intermetallic; these precipitates can strengthen the alloy and give it better resistance towards mechanicals stresses.

- **Iron (Fe)**: it's the most common found aluminum impurity, outside of silicon, and the crux of our study.
  Separating iron from aluminum is both complicated and uneconomical, especially during the disassembly of vehicle wrecks and/or spent machinery; thus, recycled aluminum tends to contain high amounts of ferrous impurities as compared to primary alloys.
  Iron negatively impacts the alloy's mechanical properties, although it might help during die-casting processes as an inhibitor of mould adhesion.
  Despite being highly soluble in molten Al alloys, it has a very low solubility cap in the solid matrix (0.05 wt.%, see Graph 5): this is the main drawback of iron as an impurity, since it leads to the formation of numerous intermetallic phases together with other elements present in traces in the system.



Graph 5 - Al-Fe phase diagram, obtained by Thermo-Calc [5]

Some of these species can help in strengthening the alloy, especially during high temperature use, while others possess a brittle acicular shape. If we consider a traditional die-cast process, these phases can precipitate both in the injection chamber/channels and the mould cavity: in the former case, the compounds will

possess compact yet coarse morphologies, while in the latter finer and even more compact morphologies are formed (thanks to a faster cooling process).
The main intermetallic phases are the following: [24]

- **α-AlFeMnSi**: it's a compact, blocky phase that's less harmful to mechanical resistance as compared to the other ferrous species.
- **β-AlFe**: it's a needle-like phase that's both highly fragile and harmful to ductility.
- **α-AlFeSi (without Mn)**: it's a compact phase.
- **β-AlFeSi (without Mn)**: it's is needle-like species that's particularly harmful to the alloy's mechanical resistance.

These species will be discussed in further detail in Chapter 1.6.2.
Their presence can positively impact yield strength by increasing it, with a consequent reduction in break-point elongation. However, iron contents above 5 wt.% lead to a drastic decrease in tensile strength.

The eutectic silicon modification in casting alloys is an essential step in the production of high-quality casts. The eutectic silicon takes a platelike form that may impact mechanical properties; the modification treatment leads instead to the silicon's dissolution and spheroidization. Such spheroidization can be achieved through elements acting as modifiers (Sr, Na) or by heat treatment at high temperatures. [4]

1.6.1 Defects in Al-Si casting alloy

Both alloys that are studied throughout this thesis have been originally employed in casting processes: for this reason, studying the defects that might have been present in them before the atomization may help in further understanding the performance and behavior of the final printed products.
Casting defects inside Al-Si can significantly affect the quality and the mechanical performance of the final product. The most common classes are as follows: [4, 5, 6, 23,24]

- **Gas/air porosities and micro porosities**: either rounded or oval shaped; they are typically brought on by either hydrogen released from the molten alloy, gases entrapped by turbulences during the metal pour or by hydrogen freed from the mould/die surfaces during the casting itself.
- **Shrinkage and micro-shrinkage porosities**: these defects are mainly caused by an inadequately balanced contraction of the molten metal during solidification.
- **Oxide layer entrainment (also known as "bifilm")**: refractory particles originated from sources such as holding furnaces, tools or the crucible may be introduced inside the casting's structure during the pouring. Due to high oxygen affinity, Mg and Al oxides can form and subsequently be entrapped inside the alloy.
- **Filling-related defects:** these defects happen due to improper filling of the die space and are easily noticeable through visual inspections.
- **Metal/ Die interaction**: these interactions, like soldering, erosion, thermal cracking and adhesion happen during casting and might lead to the formation of defects.
  The complex chemical and physical interplay between the molten metal and the die's surface can lead to several different defects, such as iron Chinese scripts.
- **Solidification cracks:** also known as hot tears, these cracks are a result of tensile stresses that occur during the passage between solidification and cooling of the alloy, which lead to fractures whenever the metal's strength at high temperatures is exceeded.

To reduce the number of these defects several strategies are viable, such as:

- Selecting a proper die material for the chosen alloy
- Applying protective coatings/treatments to the die's surface
- Applying a proper lubricant layer
- Optimizing the toolset's design

In regards of solidification, porosities caused by air entrapment and solidification shrinkage can be reduced but never removed altogether; this impacts the variability in the alloy's mechanical properties. Regarding size, air entrapment porosities usually lie in the 10–2000 μm range. [23]
Oxide inclusions are particularly noteworthy since they might lead to the formation of dross during the alloy's holding process: this might lead, if coupled with improper handling, to the entrapment of dross inside the cast part.
To minimize these defects and to ensure a higher quality casting mould design, controlled design rates and a proper study of the alloy's behavior are required.
Other, less common, defects are Cold shuts: these are caused by the unproper solidification of two differing streams of molten metal, thus leading to the formation of weak seams. [23]

1.6.2 Intermetallic phases in cast Al-Si alloys

Al-Si alloys can contain a swathe of different intermetallic compounds, all based on the alloy's composition and heat treatment history.
These phases may be found in either the α-Al phase or the eutectic phase as a function of the alloy composition. [24]

1.6.2.1 α-Fe intermetallic compounds

These intermetallic phases are found in many Al-Si alloys due to the presence of relatively large amounts of both Fe and Mn (either originating from the recycling process or introduced as direct alloyants).
These species take a polyhedral form whenever they solidify as the primary phase, before the eutectic; different shapes are achieved subsequently in function of the alloyants, and the most important ones are as follows: [24]

- **Chinese scripts**: the main shape class, it involves low quantities of chromium paired with specific amounts of copper; several ratios are commonly reached, with the main forms being $Al_{15}Fe_3Si_2$, $Al_{15}(Fe, Mn)_3Si_2$ if Mn is present in the alloy or $Al_{15}(Fe, Mn, Cr)_3Si_2$ if Mn and Cr have been added to the system. See Figure 9 for a SEM scan of a series of α-$Al_{15}(Fe, Mn)_3Si_2$ phases.

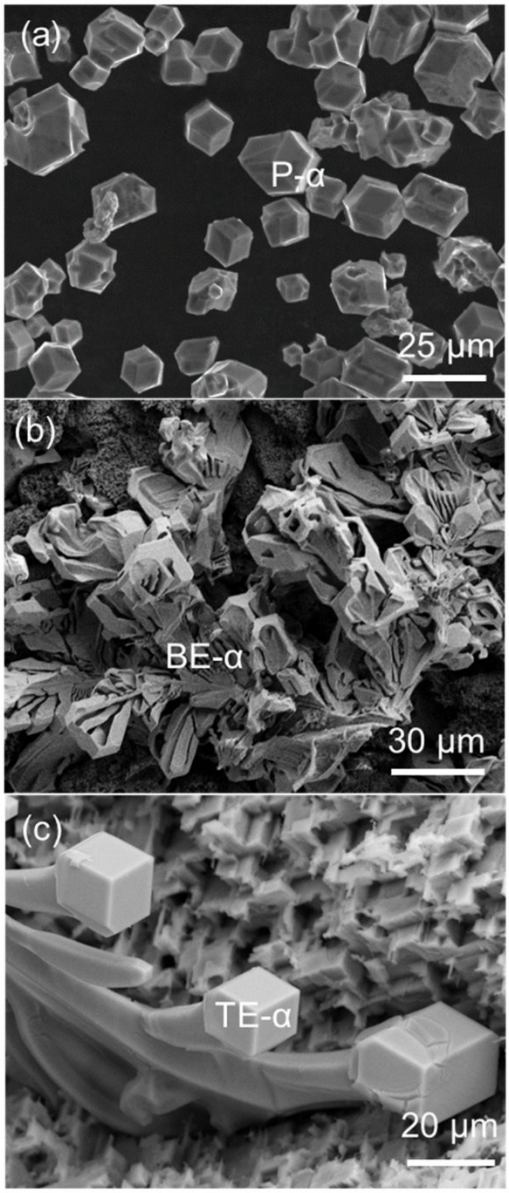


Figure 9 - SEM images taken from several different morphologies of α-Al_{15}(Fe, Mn)$_3Si_2$: (a) extracted primary α-Al_{15}(Fe, Mn)$_3Si_2$ (denoted as P-α) with a compact morphology in Al-5Mg-2Si-0.7Mn-1.3Fe alloy solidified at 3.5 K/s; (b) binary eutectic α-Al_{15}(Fe, Mn)$_3Si_2$ (denoted as BE-α) with a Chinese script morphology in Al-3Mg-2Si-0.7Mn-1.3Fe alloy solidified at 3.5 K/s. The sample was deep-etched; and (c) ternary eutectic α-Al15(Fe, Mn)3Si2 (denoted as TE-α) with compact morphology in Al-2Si-0.7Mn-1.3Fe alloy solidified at 0.01 K/s. [25]

- **Starlike polyhedral shapes:** this morphology class takes form whenever Cr content reaches a quantity above 0.1 wt.%; some typical examples of this class Al_{13} (Fe, Cr)$_4Si_4$ or Al_2(Fe, Cr)$5Si_8$.
- **Acicular shapes:** these fragile intermetallic phases nucleate whenever copper content is present. AI_7FeCu_2 is a typical compound.

Most commonplace compositions can be derived from the following formula:

$$Al_x(Fe,Mn,Cr,Cu)_ySi_z$$

Where: x= 11.7 – 16.5; y= 2.3 – 3.3 and z= 2.

Several substitutions between alloyants may be encountered: Mn can be replaced in part by Fe, while Cu can be partially replaced by Al, following the $(Al, Cu)_{15}(Fe, Mn, Cr)_3Si_2$ formula. Another typical Chinese script phase is AlFeSi, where the iron content is around 30 wt.%. [26]

1.6.2.2 β-Fe and δ-Fe phases

The β-Fe class is comprised of brittle needle-shaped, iron-rich intermetallic phases, of which the β-Al_5FeSi compound is the main species (see Figure 10 and Figure 11): these compounds act as stress concentration sites while under mechanical duress (especially uniaxial traction), thus leading to a sharp drop in the alloy's mechanical strength. In addition, this intermetallic class seems cause also the degradation of castability and an increase in porosity content. [24,27]

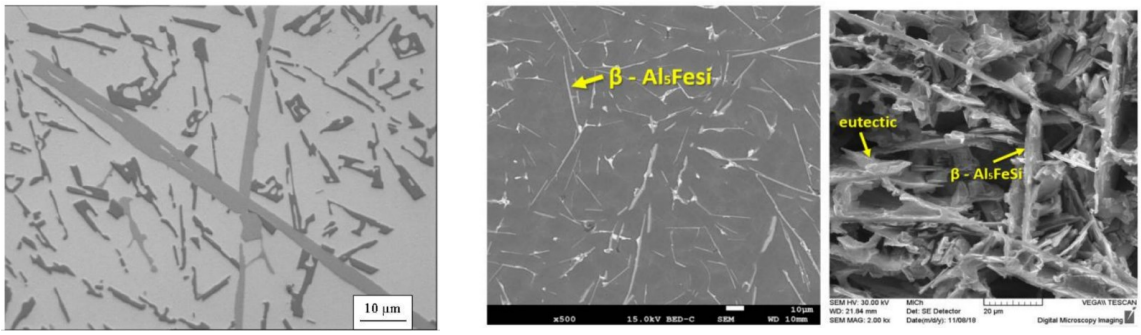


Figure 10 - SEM images taken from several different morphologies of β-Fe class phases [24,27]

The plate-like intermetallic AlFeSi phase δ-Al_3FeSi_2 is instead typical of Sr-modified alloys and is characterized by a Fe-Si ratio of 1:2: As a detrimental impurity, its presence in large, coarse, or plate-like morphologies can reduce castability, promote crack formation and reduce the system's mechanical properties, though its size can be modified by acting on the strontium content and by employing a rapid cooling [28]. Its morphology is still less damaging than the needle-like shape of the β-Fe class.

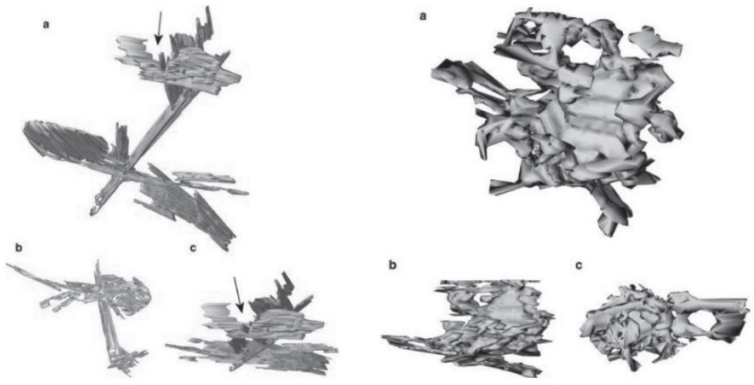


Figure 11 - 3D reconstruction of the intermetallic phases β-Al5FeSi (a), with platelet morphology, and (b) α-Al15(Fe, Mn)3Si2 with "script-like" morphology [29]

1.6.2.3 π-Fe phases

The π-Fe phase class (as pictured in Figure 12) is characterized by a Chinese-script shape, with a typical composition of π-$Al_8FeMg_3Si_6$; whenever the Fe amount falls below the Mg percentage, the π-Fe phase compositions switches to either $Al_{10}FeMg_4Si_4$ or $Al_5FeMg_8Si_6$. Other Fe intermetallic phases in this family can nucleate by adding other alloyants like Ni (producing Al_9FeNi) or Cu (leading to Al_7FeCu_2). [24]

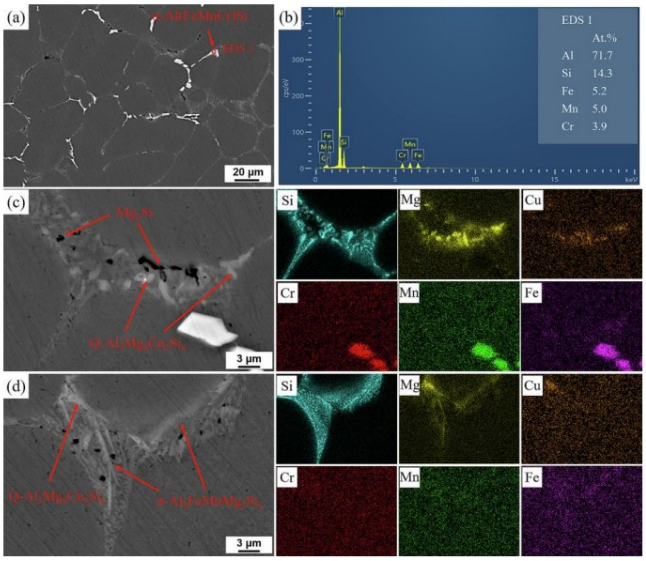


Figure 12 - π-Fe, Q-phase and Mg2Si phase observed in AlSiMgCu alloy [24,30]

These phases typically possess an acicular or plate-like shape.

1.6.2.4 θ-Al_2Cu and Q-phase

In the θ-Al_2Cu phase, Nickel addition can be considered beneficial or detrimental, depending both on the alloy's composition and the solidification behavior: for an example, Ni negatively affects strength in both as-cast and T6 heat treatment in A356 alloy (AlSi7Mg) while its able to increases the mechanical strength and wear resistance in other alloy compositions after the same heat treatment.
These phases' morphologies change depending on the solidification and aging processes, varying between lamellar shapes and rod-like structures based on the employed cooling speed. [31]

Q-phase composition varies a lot instead, following several different stoichiometries: $Al_3Mg_9Si_7Cu_2$, $Al_4Mg_8Si_7Cu_2$ and $Al_5Mg_8Si_6Cu_2$ are widely reported in the literature.

Both θ-Al_2Cu and Q-phase act as barriers against dislocation movements, increasing the strength of the alloy up to 300 °C. At higher temperatures ranges, such phases dissolve into the α-Al matrix. [24,31]

1.7 Solidification rate and the impact on Al - Si microstructure

The Solidification rate is one of the main factors driving morphology inside these aluminum alloys, together with their chemical composition and, eventually, their subsequent heat treatments.
The L-PBF process entails some of the highest cooling rates in metal production, with values typically falling in the 10^4 -10^7 °C/s range [32]; this is in stark contrast with more traditional techniques like sand casting (10 °C/s), investment casting (1 - 10^2 °C/s) and die casting (10^2 – 10^3 °C/s). [33,34]
In most cases, slower cooling rates increase the risk of large particle formation, while higher rates keep the particles small.
In the following paragraphs, a brief overview of this topic will be showcased, with a focus on both traditional casting techniques and newer production techniques.

1.7.1 Si morphology

Silicon morphology is strongly impacted by the applied cooling rate; Si in Al-Si alloys changes its shape radically based on the applied cooling speed: Table 3 reports a brief breakdown of the observed eutectic silicon phases obtained through a traditional gravity die casting process, highlighting how slight changes in cooling speed could affect the microstructure [35].

Table 3 - Impact of cooling-rate tampering on eutectic silicon microstructure, Al_7SiMg gravity die casting [35]

Cooling Speed (°C/s)	*Observed Microstructure*
0.2	Planar Snowflakes
9	Branching, continuous distribution

Lower cooling rates have been shown to lead to coarser silicon particles, while faster cooling speeds allowed the growth of finer grains, as shown in Figure 13

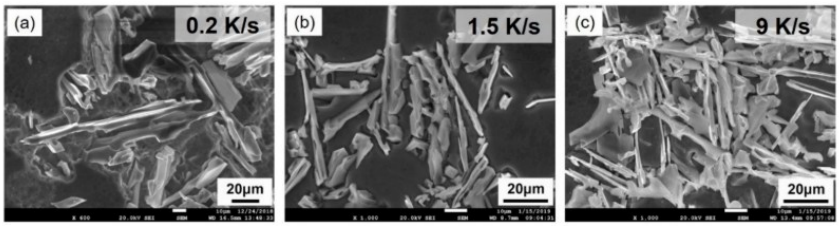


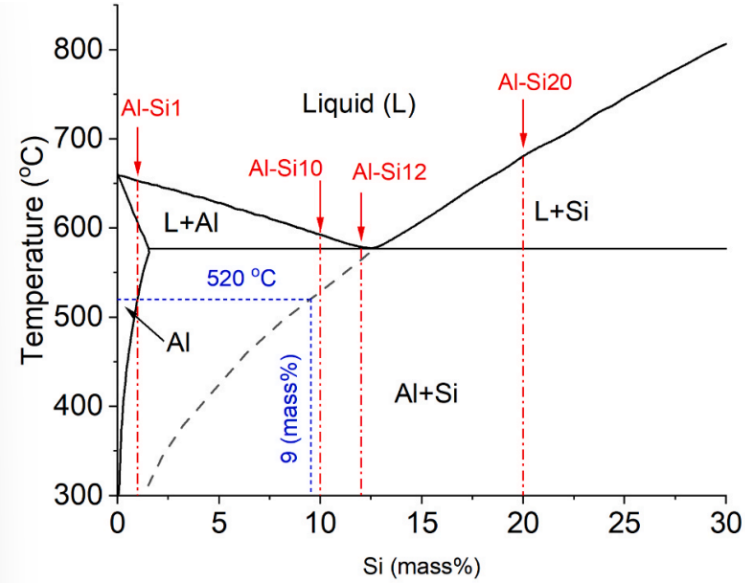
Figure 13 - 3D morphology of eutectic Si in (a - c) Al7SiMg.[35]

A research conducted by F. Alghamdi et al. (2020) on heat treated AlSi10Mg showed that at higher cooling rate ranges, such as between 10^6 and 10^8 °C/s, Si solubility in the Al matrix is extended up to 8 wt.%, instead of the 1.65 wt.% of the equilibrium condition: this means that novel production techniques, such as L-PBF, could lead to completely new microstructures as compared to lower cooling-rate techniques like traditional casting. [36]

1.7.2 α-Al morphology

It has been widely reported that α-Al phase changes its morphology depending on the applied cooling rate.

In a 2023 study by Q. Peng et al. differential fast scanning calorimetry (DFSC) was employed to conduct a series of thermal analysis on Al -Si alloys during rapid heating and cooling differentials, employing scanning rates above 10^4 °C/s [37]. DFSC has been utilized to study metallic (and intermetallic) materials' behavior in various situations, such as rapid heating and cooling processes (at speeds typical for AM) [38,39] and the associated nucleation and growth [40,41]. Due to its ability to control a wide range of scanning rates, DFSC is a reliable method for detecting phase transformations in metallic materials during rapid solidification.
By employing DFSC combined with electron microscopy characterization, the link between rapid cooling and the nucleation mechanism of the α-Al phase and the microstructural features of Al-Si alloy particles was studied, spanning from hypereutectic to hypoeutectic compositions (i.e. Al-Si alloys with 1,10, 12 and 20 wt.% Si content [37]; see Graph 6 for an Al -Si phase diagram highlighting the studied compositions)



Graph 6 - Al-Si phase diagram showing the investigated alloys. The black dashed line shows the metastable extension of the Si liquidus line [37]

The study highlighted how different α-Al phase nucleation mechanisms take place based on both composition and applied cooling speed: following a mathematical analysis of the theory behind the process, the paper reported that an increase in cooling rates lead to finer microstructures for the Al-Si alloy particles. The microstructures themselves formed during solidification, where higher cooling rates led to large nucleation undercooling, causing an increase in nucleation rate, shorter solidification times; this ultimately led to a generally finer microstructure. [37]
In Table 4, a brief description of the behavior of the α-Al phases for each of the studied alloy is provided, which are also represented in Figure 14 (the grey regions representing the α-Al phase, while the bright regions being the Si phase):

Table 4 - Impact of cooling-rate tampering on α-Al phases' microstructure [37]

Alloy (Si wt.%)	Behavior
20	The microstructure includes primary Si, α-Al dendrites, and (α-Al + Si) eutectic structures. The primary Si possesses a polygonal morphology (marked in Figure 14 by red arrows), which likely solidifies firstly from the surface of the particle, followed by the solidification of α-Al on the primary Si interface, and the (α-Al + Si) eutectics.
12	The microstructure is composed of α-Al dendrites and (α-Al + Si) eutectic structures. In this case the primary α-Al dendrites have formed from the surface of the particle. During cooling, the particle nucleated from the surface resulting in a finer microstructure of α-Al. However, as the solidification proceeded further away from the nucleation region, the microstructure of α-Al became coarser due to the influence of the recalescence effect within the particle
10	Like in the previous case, the microstructure is composed of α-Al dendrites and (α-Al + Si) eutectic structures In this case, α-Al dendrites have formed both on the surface and inside the particle inclusions simultaneously. The inclusions inside the particles could potentially be oxides or impurities. Considering the Al-Si10 particle with a diameter of 22 μm which solidified at 50,000 °C/s, α-Al dendrites have solidified from both the surface and an inclusion located in the middle of the particle (marked by a red circle).
1	Different microstructures can be observed in Figure 14 as the cooling rate increases. For instance, the size of α-Al dendrites reduces significantly at cooling rates exceeding 5000 °C/s. Tiny (α-Al + Si) eutectic structures are present at high cooling rates. It is noted that a lot of globular microstructural features can be observed in the Al-Si1 particle solidified at 500 °C/s, while fewer globular features can be observed with increasing cooling rate; these globular features are believed to form during a phenomena known as "recalescence": during this process, the temperature experiences an abrupt rise from the nucleation temperature to the maximum recalescence temperature, TR. Once TR exceeds the solidus temperature, the first solidified α-Al solid solution with a higher concentration of Si begins to remelt. Upon subsequent cooling, the remelted part solidifies again, resulting in a different structure with a high concentration of Si, as shown by the globular features in Fig. 4. As the temperature decreases, the solubility of Si in α-Al decreases, leading to the precipitation of Si. With increasing cooling rates, the significance of recalescence decreases. This is due to the decrease in nucleation temperature (i.e., increase in undercooling) and the increase in cooling effect, resulting in a decrease in TR. If TR is lower than the solidus temperature, no remelting occurs, and the globular features will not form.

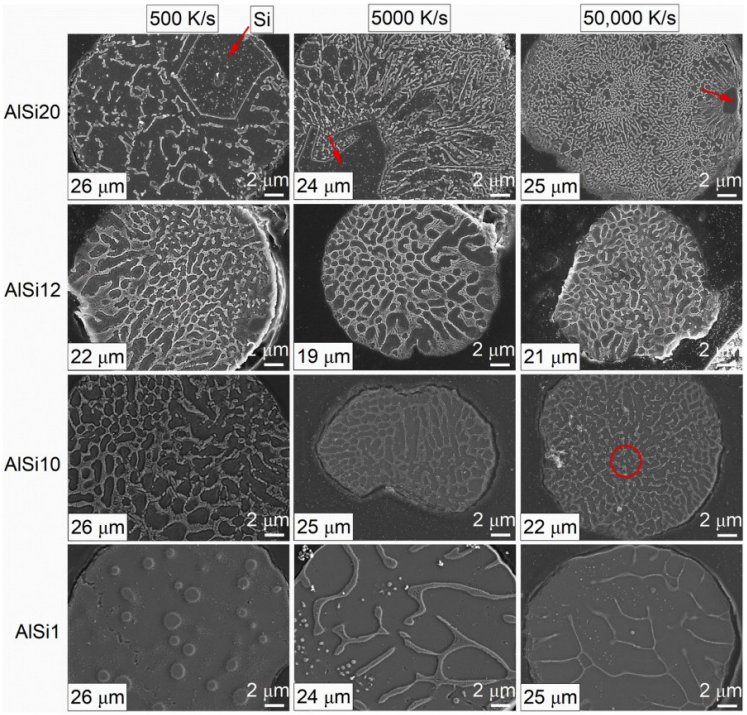


Figure 14 - SEM secondary electron images of single particles solidified at different cooling rates. Particle diameters and cooling rates are given, respectively. Red arrows indicate the primary Si with polygonal morphology in Al-Si_{20}. Red circle indicates a heterogeneous bulk nucleation site in Al-Si_{10} [37]. *Images of $AlSi_{12}$ particles are adapted from* [38]

1.7.3 Intermetallic phases morphology

An article by B. Yang et al. (2021), delved into the effects of the cooling rate on the microstructural evolution of a series of Al-Si recycled samples with the following composition (Table 5) [42]:

Table 5 - Composition of the recycled Al-Si alloy [42]

Element	*Al*	*Si*	*Fe*	*Mg*	*Cu*	*Zn*
Content (wt.%)	*Balance*	*9.96*	*1.52*	*0.33*	*0.09*	*0.07*

The paper focused on the size and morphology of the secondary intermetallic phases, to evaluate the impact of recycling by traditional means; the Al-10Si-1.5 Fe alloy investigated in this report was first obtained by melting Al-12Si and Al-20Fe scraps in a vacuum arc furnace under an argon atmosphere, only for it to be remelted under two different processes:

- For a low cooling rate sample, the ingots were remelted using an induction smelting method, during which the molten metal was poured inside a preheated 200 °C steel mould. The obtained cooling rate was 6.7×10^2 K/s.
- For high cooling rate samples, the secondary melting was carried out in a high-frequency induction smelting furnace and the smelt material was blown on a rotating, cooled copper roller. The obtained cooling rate was 2.4×10^4 K/s.

The obtained samples were then analyzed using XRD spectrum analysis, SEM imaging, Differential Thermal Analysis (DTA) thermography and uniaxial tensile testing.
The research highlighted several important details:

- The needle-like β-Al_5FeSi phase reached the size of ~80 µm after the conventional casting. As the cooling rate increased to ~10^2 K/s, the needle-like β-phase changed into the fishbone-like δ-Al_3FeSi_2 phase. At the higher cooling rate of ~10^4 K/s, the size

of the β-Al_5FeSi phase decreases to ~500 nm and the morphology changed to a granular, equiaxed form.

- The change in cooling rate reduced the eutectic temperature of Fe-rich Al–Si alloy and promoted the phase transformation of eutectic silicon. The DTA analysis results showed that the increase in the cooling rate contributes to forming the fishbone-like δ-Al_3FeSi_2 phase and plays an important role in modifying the structure of the eutectic Si.
- Fracture morphology analysis demonstrated that, while the platelet-like β phases were the initiation point of cracking and favored crack propagation, the fine Fe-rich particles are relatively helpful in improving both the tensile strength and elongation of the alloy.

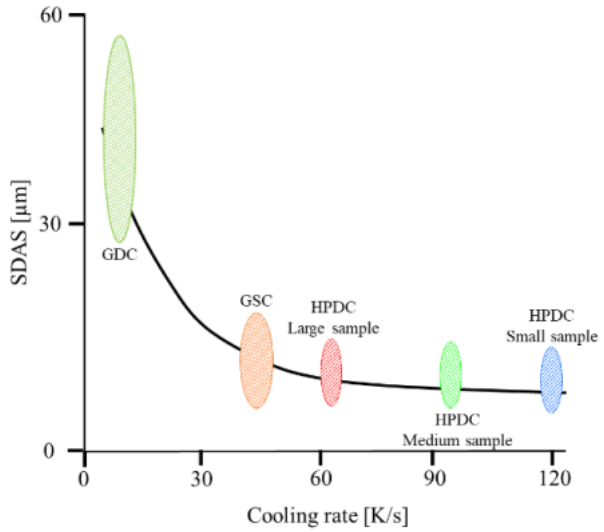
It was also proved that the melt spinning method (which entailed the faster cooling speed) transformed the previously brittle mechanical failure of the Fe-rich Al–Si alloy into ductile failure, which is indicative of potential recyclability of Fe-rich Al–Si alloys for use in mechanical, industrial settings if paired with a sufficiently fast cooling process during manufacturing. [42]

It has been shown that both increasing the Fe content inside an alloy and decreasing its solidification rate leads to a lengthening in the β-Fe platelets size: this phenomenon enhances the embrittling effects of this intermetallic phase class. [43]
In a paper by Wang et al. (1999) it was reported that higher Fe percentages (≈1.6 wt.%) generally favor the formation of needle shaped morphologies (i.e. β-Fe and δ-Fe phases), whereas lower Fe contents (≈ 0.7 wt.%) favor either polyhedral or Chinese script morphologies; higher cooling rates, such as the ones achieved in high pressure die casting, suppress the nucleation of β-Fe platelets by inhibiting the segregation of Fe and favor the formation of α-Fe Chinese scripts: this causes an overall reduction in both the size and number of these intermetallic phases inside the alloy's structure. [44]
In addition, increasing cooling rates have been shown to lower dendrite arm spacing: considering that β-Fe phases nucleate mainly in interdendritic spaces, this phenomenon leads to an even more reduced phase size.
Considering instead the secondary dendrite arm spacing (SDAS), it has been observed that in Sr-less A357-T6 alloys increasing the cooling rate greatly reduces the SDAS (see Table 6), even without reaching the typical cooling speeds associated with AM. [47]

Table 6 - Impact of cooling-rate tampering on SDAS value, Al-20%Si high pressure die casting [47]

Cooling Speed (°C/s)	*SDAS (μm)*
1.3	*32*
4.5	*22*
35	*11*

Lower SDAS values lower the size of both the Fe-rich and Si particles: having smaller particles greatly reduces the incidence of fragile cracking and therefore, a decreasing rate of particles cracking while under mechanical stress should be expected whenever the SDAS is decreased. Graph 7 showcases a typical set of casting processes and their associated SDAS values.



Graph 7 - Cooling rate vs Secondary Dendrite Arm Spacing (SDAS) with different casting processes for AlSi9Cu3 alloy. GDC, Gravity Die Casting; GSC, Gravity Sand Casting; HPDC, High-Pressure Die Casting; S, M, and L refer to different HPDC sample sizes [48]

In the case of Sr-modified alloys the refining effect of faster cooling rate has been observed inside Fe-rich intermetallic phases, while the size of the Si particles has been shown to be much more dependent on the Sr additions instead of the SDAS.
Damage accumulation has been proven to be directly linked to the sizes of both Si particles and the Fe-rich phases:

- If the Si particles are larger than the Fe-rich intermetallic compounds, cracking inside the alloy will accumulate inside the latter species. This happens mostly with alloys containing amounts of Sr that exceed 100 ppm [45,46]
- In the case of unmodified alloys, the impact of Fe-rich phases is less important.

However, the impact caused by rapid cooling depends as whole by the amount of Fe in the alloy and by extension, the amount of Fe-rich intermetallics: the higher the concentration of iron inside the secondary alloy and the higher the role of cooling speed on its microstructure. [47]

While this topic has been studied in the context of traditional casting techniques, the link between cooling rates and Al-Si alloy's morphology is still a topic of discussion both in the lenses of gas atomization and additive manufacturing techniques: several papers have been published throughout the last decade on the subject, mainly on focused on the microstructural evolution of primary alloys. [48,49,50]
This thesis will delve specifically into the effect caused by the cooling rate of both the gas atomization and the Laser Powder Bed Fusion for secondary aluminum, highlighting any possible difference between this case scenario and the more traditional production processes.

1.8 Gas Atomization: a brief overview

Gas atomization is one of the main powder atomization processes that are employed in the manufacture of metal powder: it involves the conversion of a molten metal batch into small, spherical particles by employing jets of high-pressure gas.
This technique can be employed for a wide variety of materials and batch sizes, allowing for both small laboratory-scale powder lots and large industrial-scale batches.
The obtained powders are mainly used in metal injection molding (MIM), hot isostatic pressing (HIP) and Laser Powder Bed Fusion (L-PBF). [24,51]
Figure 15 showcases a simplified scheme of a gas atomizer, highlighting its main components.

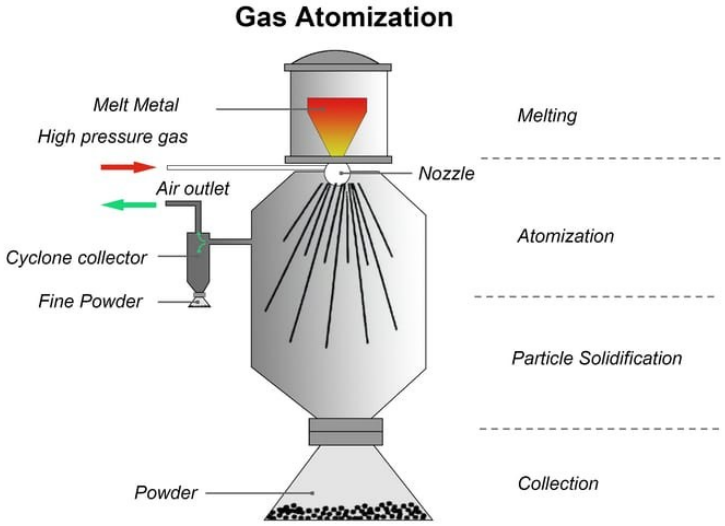


Figure 15 - A scheme of a typical Gas atomizer [51]

The production process initiates with the melting of the starting material: this might be done using either induction or electric arc furnaces. After the feedstock has crossed its melting point it is overheated, to ensure full liquification and the complete solubilization of any added alloyants/master alloys.
The molten alloy is then transferred from its ladle to a fusion chamber: this is typically an enclosed, tall, cylindrical chamber equipped with a nozzle at the bottom. The chamber's atmosphere is tightly controlled, either by being flushed using inert gases (such as Argon) or by being kept under a vacuum (VIGA systems, meaning "vacuum inert gas atomizer", employ both means); this is done in order to prevent oxidation of the molten metal's surface and to preserve its composition. The chamber itself contains a heating system, in order to modulate the melt's temperature in its last moments before the atomization: in smaller atomizers, such as the one employed during our research, all the heating is conducted inside the fusion chamber. [24,52]
As soon as the molten metal has satisfied a set of requirements (such as temperature and time spent overheated), it is forced (typically by re-introducing a pressure gradient) through the nozzle [52]: there are several types of this component, mostly divided between "confined" and "free fall" designs (see Figure 16); all of them are equipped with a series of small channels or jets through which a high-pressure gas, typically inert gas like either nitrogen or argon, is flushed. As the molten metal is forced through the nozzle, it encounters the high-pressure gas

jets, before entering what is known as the “atomization chamber”. Figure 17 showcases the scheme of a typical confined “ultrasonic” gas atomizer.

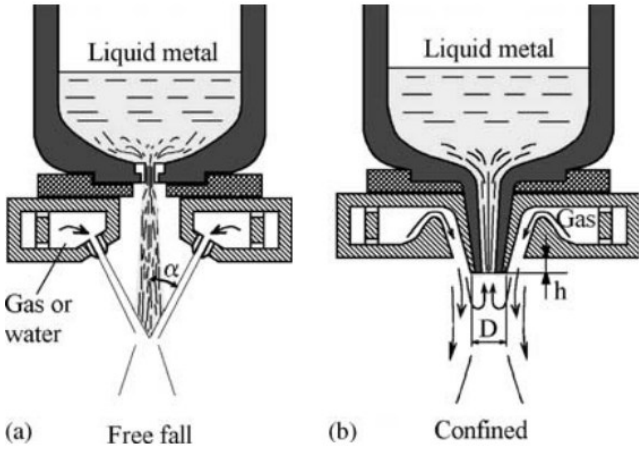


Figure 16 - Atomizer designs of two types: (a), free fall design (gas or water) and (b) confined nozzle design (only gas) [53]

Small droplets and particles form as soon as the metal flow encounters the gas jets: parameters such as the gas’ pressure and the nozzle diameter help in controlling the size and shape of the resulting metal particles.
As the metal droplets are atomized, they rapidly cool and solidify as they fall through the atomization chamber: this chamber is filled with an inert gas atmosphere, thus helping to prevent oxidation of the metal particles’ surface during cooling. The solidified metal particles accumulate at the bottom of the chamber, where afterwards they are collected.

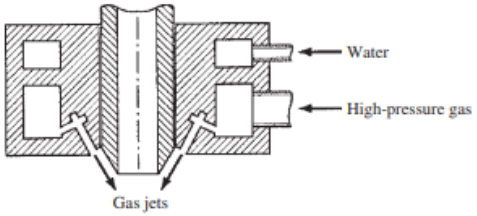


Figure 17 - diagram of an Ultrasonic gas atomizer [55]

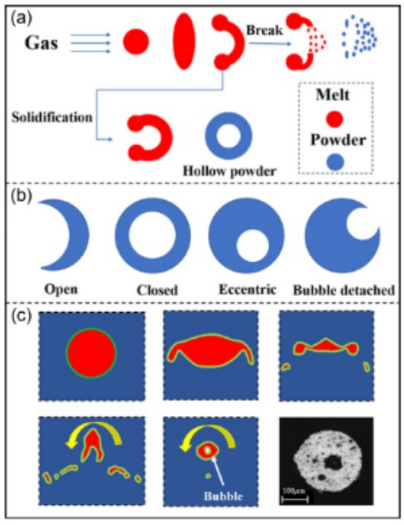
Sieving is often added as an additional step after atomization, in order to remove powders that fall outside the desired size ranges and shape class; another typical additional step is annealing, which is conducted to modify the powder’s mechanical properties.
Gas atomization yields metal powders with a relatively uniform particle size and shape: they are typically spherical in shape, which enhances aspects such as the flowability, packing density and sinterability of the metal.
The use of inert gases and vacuums allows the gas atomization process to produce powders of a high purity grade, with less impurities as compared to processes like water atomization; this, combined with the higher degree of complex equipment, also leads to higher production rate. [54].

For these reasons, gas atomized powders are employed in industries requiring high-purity feedstock, such as additive manufacturing, metal injection molding and high-performance alloy production: the production technique that is studied in this paper is the Laser Powder Bed Fusion (L-PBF) process.

1.8.1 Defects in gas-atomized powders

To be able to ascertain the quality of the atomization, the powder's morphology must be studied. [55]
Several commonplace defects may inhibit the efficiency of the printing process, leading to lesser mechanical properties; as an example, their sphericity is generally closely related to their fluidity, which impacts AM: for this reason, if gas atomization causes poor sphericity, the L-PBF process will be negatively impacted. [56]
The following table broadly describes these criticalities and their associated causes:

Table 7 - list of typical defects in gas-atomized powders

Defect type	Description
Satellite	Satellites significantly hinder the flowability of powders, thus hindering their utilization in 3D printing applications. The main cause of satellite formation has been pinned on collisions between either high-temperature droplets and solidified particles or between two high-temperature droplets. Since in gas atomization the particle size range tends to be relatively broad, this phenomenon is most often present. [57] A comparison between atomizing gases has shown that Helium yields the lowest number of satellites, while Argon is the highest: this is directly related to the gas' heat transfer coefficient.
Hollow powder	Hollow powders are the main source of cavities inside AM products Their formation mechanism is described in the following image:  *Figure 18 - The formation process of hollow powder.* [59] Two main subtypes of hollow powders can form, depending on the dynamics of the solidification process: these are the open and closed hollow powders. It's believed that the formation of hollow powder is caused by a high velocity difference at the gas–liquid interface during the primary atomization process, which is caused by the instability of Kelvin Helmholtz: this leads to the entry of gas into the liquid, in the form of bubbles, ultimately forming hollow particles upon solidification. [60]

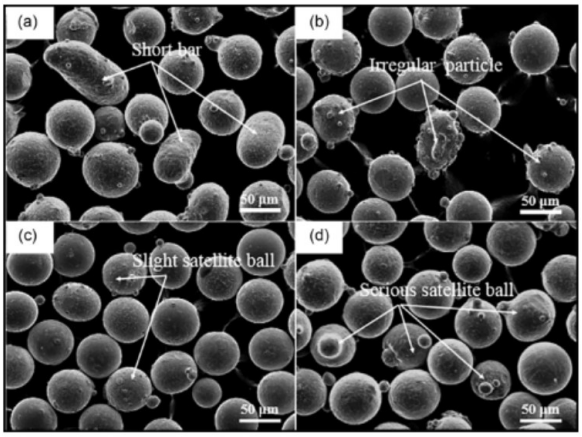
	Large-sized powders have been shown to be affected by cavities at a higher rate, while the proportion of small-sized hollow powders is generally lower (as an example, powders sized less than 50 μm generally showcase low degrees of porosity). [60] To decrease the proportion of hollow particles several strategies have been developed: - Reducing the melt's viscosity, by raising the melt's temperature - Enhancing the gas energy, by acting on its velocity - Reducing the particle's size
Irregular Powder	Irregular morphology significantly impacts flowability, which in turn impacts both the diffusion process during laser-selective melting and the powder feeding process during the powder's deposition. Irregular particles are mainly caused by the solidification time being shorter than the spheroidization time: this means that the melt will solidify before it can fully spheroidize, thus producing irregularly shaped powder. Greater powder sphericity can be obtained by employing higher atomization pressures, but excessive values lead to an increase in both gas resistance and the gas' cooling capacity: this elongates the particles, making them attain a needle-like shape (see Figure 19).  *Figure 19 - SEM images of 24CrNiMoY powder prepared under different gas pressures. a) 6.0 MPa, b) 7.5 MPa, c) 9.0 MPa, and d) 10.5 MPa.* [61]

Figure 20 sums up these defects and the associated formation mechanisms.

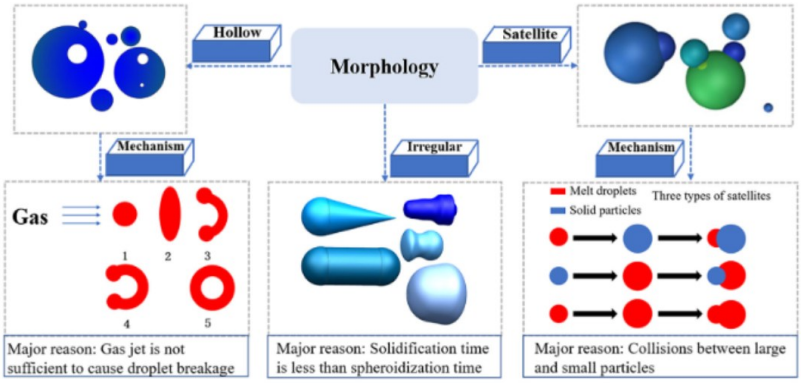


Figure 20 - Powder morphology and formation mechanism [55]

1.9 Laser Powder Bed Fusion (L-PBF)

Laser Powder Bed Fusion (L-PBF) is an AM process employed in the manufacture of high-precision metal and alloy components.
L-PBF allows for the creation of complex geometries and detailed parts that would be otherwise difficult or impossible to achieve by traditional manufacturing means.

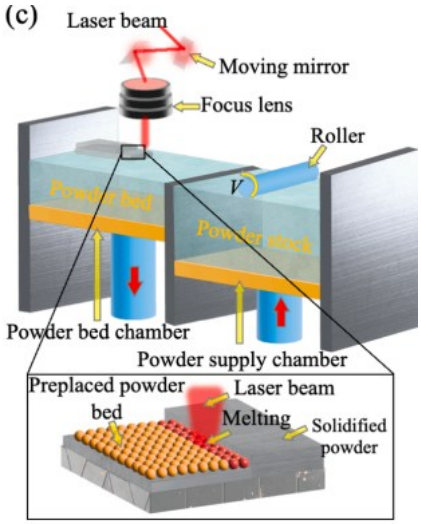


Figure 21 - Schematic diagrams of the Laser powder bed fusion process [62]

During this process, a component (or a series of) is built one layer at the time: a high-powered laser selectively melts and re-solidifies a pre-placed layer of the alloy's powder, over which the next layer is placed using a roller (also known as blade or recoater) that picks up the material from a powder supply chamber; the process is repeated, layer by layer, until the part is completed. Afterwards, the printed element is retrieved, and the excess powder is removed and sent to a sieving system to be recycled.
The system is enclosed in a chamber, allowing it to be filled by a inert gases (argon or nitrogen): this protects the powders from unwanted oxidation, ensuring higher quality in the final product, and from any possible problem of explosion considering reactive powders, such as Al and Ti alloys.
The printing process is conducted on a moving platform, which allows the printing layer to be in level with both the recoater and the powder supply chamber.

Both the laser's path, called scanning strategy, and the distance between layers must be defined by the operator in order to achieve the highest density.
To increase the adhesion between the platform and the powder layers, while also reducing the presence of residual stresses, the printing bed chamber can be pre-heated at a temperature dependent on both the machine's capability and the powders themselves.
The platform material has to be similar to the employed powder, both from a weldability behavior and from a chemical point of view; this requirement is crucial to prevent the following:

- The formation of brittle intermetallic compounds
- Insolubility between the two metals: this would lead to the detachment of the part from the substrate during printing, thus wasting the partial product.

The printed parts will showcase an anisotropic mechanical behavior: this is due to the innate differences in the microstructure that originate as a consequence of the highly directional printing process. For this reason, L-PBF parts are often subjected to thermal treatments to reduce their structural inhomogeneities. [24,62]
During this thesis project, no additional thermal treatment will be applied after producing samples by L-PBF.

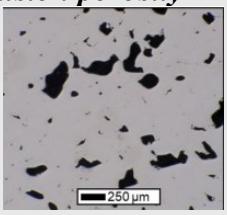
1.9.1 Defects in AM components

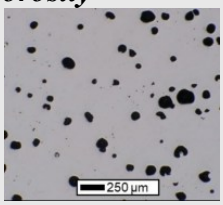
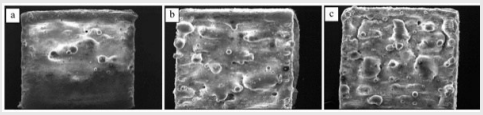
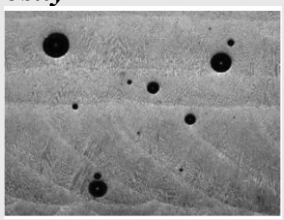
While evaluating the effectiveness of employing processes such as L-PBF for the manufacture of high precision mechanical components, its parameters must be studied thoroughly case by case in order to obtain the desired mechanical behavior: modulating laser settings, using powders of proper quality and tightly controlling the process' parameters is essential; regular checks on the printed part's microstructure must be performed to understand the impact of the enacted choices.
To do so, knowledge of the most common defects inside AM parts is essential; the most common irregularities are as follows: [24]

- Porosities
- Cracks
- Residual stress
- Balling
- Surface roughness
- Layer delamination

Table 8 briefly summarizes the most common defects found inside aluminum alloy L-PBF parts.

Table 8 - list of typical Microstructural defects in L-PBF printed parts

Lack-of-fusion porosity  *Figure 22 - Optical microscope image of polished cross-section a of cubic specimen, lack of fusion pores* [64]	This defect occurs whenever the laser fails to fully melt and fuse the metal powder particles. This results in voids or pores within the printed material. [24,66]

Keyhole porosity  *Figure 23 - Optical microscope image of polished cross-section a of cubic specimen, keyhole pores* [64]	This defect occurs when the laser energy input is too high, causing excessive melting and vaporization of the metal powder (especially in the context of light alloys like Al). This leads to the formation of keyhole-shaped voids. [64]
Balling  *Figure 24 - Optical microscope images, highlighting how the severity of the balling phenomena increases as the scan speed increases, as shown by the LPBF printed surface profiles with scan speeds of (**a**) 250 mm/s, (**b**) 500 mm/s, (**c**) 750 mm/s* [65]	This defect occurs when molten metal forms into spherical balls rather than spreading uniformly to create smooth layers. This can lead to the creation of pores and round-shaped irregularities in the final part. [65]
Gas porosity  *Figure 25 - Optical micrograph of a cross-section of a laser deposit showing high level of gas porosity* [66]	This defect is identified by either gas-filled voids or pores within the solidified material. There are two possible causes: - Entrapped gases within the powder particles either during their production or handling - Gases absorbed by the melt from the surrounding environment These defects are especially common whenever there's contamination or insufficient shielding gas inside the printing chamber. [66]
Distortion and residual stresses  *Figure 26 - Distortions and delamination during manufacturing process leading to process failure*	Rapid heating and cooling cycles during the L-PBF process create steep thermal gradients, leading to uneven expansion and contraction: this phenomenon can worsen if combined with unproper scanning strategies/speed. As the material solidifies and cools, it shrinks: if the shrinkage is not uniform, it can cause the part to warp or distort. [67]

While most porosities can be reduced through the tuning of the print parameters, they cannot be conveniently completely removed: for this reason, depending on the final application, a certain percentage content of regular pores is tolerated inside the final product.
The practical porosity content that is typically industrially tolerated falls in the 0.05 – 0.3 % vol. range, with studies showing that 99.9 % vol. density can be reached with optimized printing parameters and a stabilized melt-pool. [68]

Like described above, keyhole and lack-of-fusion porosities are less tolerable than the gas ones, due to their irregular jagged shapes.

2 AIM OF THE STUDY

As outlined in the previous chapters, aluminum recycling is supported by a general industry-wide push towards higher environmental protection, combined with lower energy costs related to its production. At the same time, conventionally recycled Al alloys can lack the high performances that are required in the manufacture of components of sectors such as the automotive and aerospace fields.
As is discussed in Chapter 1.7, faster cooling rates have been shown to reduce the criticalities associated with ferrous intermetallic phases for traditionally casted secondary alloys: for this reason, our research moved to see if such a trend was appliable to additive manufacturing, demonstrating a possible new avenue for the production of high-performing mechanical components from recycled Al-Si alloys.
Considering both the environmental impact and mechanical properties, this research's focus was to study the processability by AM of two commonly employed hypoeutectic Al-Si alloys: AlSi10Mg and AlSi9Cu3. Both alloys originated from the automotive industry, with one being provided as a remelted ingot and the other as scrapped automotive gearbox housing.

Both alloys were rendered into powders through a controlled gas-atomization process inside the Alessandria plant of the Politecnico di Torino: this ensured complete control over the material's size and granulometry in the resulting powders, which underwent a series of further tests.
Afterwards the powders were sieved separately, before being employed in the samples manufacturing by L-PBF.
Both alloys were then characterized at microstructural level: by optical microscopy, for density evaluation; by XRD and Field Emission Scanning Electron Microscopy, equipped with EDS and EBSD detectors, to evaluate the chemical composition and the phases distribution; and finally by means of a Vickers microhardness instrument for a first rapid mechanical response.

3 MATERIALS AND METHODS

The following sections describe the origin and characteristics of each feedstock and the preparation steps carried out before gas atomization.

3.1 Alloy feedstock

3.1.1 AlSi10Mg

Table 9 reports the nominal composition range of the AlSi10Mg(Fe) alloy according to UNI EN 1706; the corresponding EN designation is EN AC-43400.

Table 9 - EN AC-43400 composition ranges [69]

AlSi10Mg (Fe)								
wt.%	*Si*	*Fe*	*Cu*	*Mn*	*Mg*	*Zn*	*Ti*	*Al*
	9 - 11	*< 1.0*	*< 0.10*	*< 0.55*	*0.20 – 0.50*	*< 0.15*	*<0.15*	*Bal.*

The material was supplied as an ingot by 2A S.p.A. Foundry (Figure 27). It was a secondary recast alloy and was therefore selected to assess the feasibility of converting recycled aluminum feedstock into gas-atomized powder for subsequent L-PBF processing.

Several control samples were cut from the ingot to verify whether the chemical composition was consistent with the certified range and to monitor possible composition changes during the subsequent recycling steps.
The initial mass of the ingot was about 5 Kg. Its measured length and height were approximately 45 cm and 5 cm, respectively.

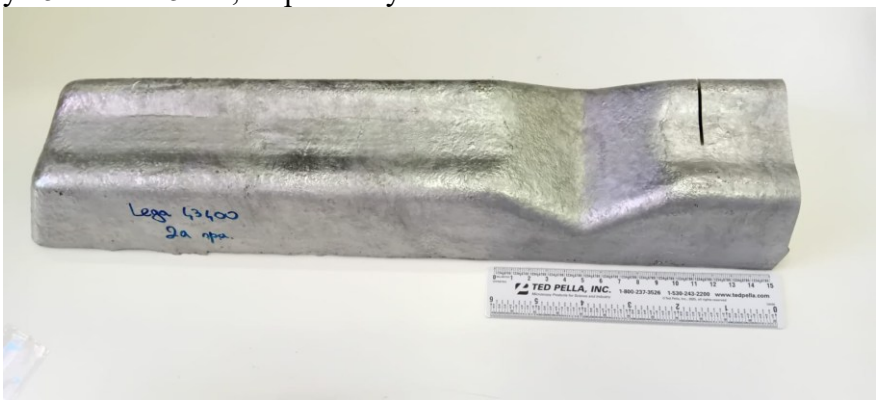


Figure 27 - AlSi10Mg Ingot, before main cuts

The bar was subsequently cut into smaller pieces to fit inside the melting crucible of the gas atomizer. The ingot was mainly cut into parallelepiped-shaped pieces, while the offcuts were approximately cubic or pyramidal. The cutting operation was performed using a table bandsaw, of the same model as that shown in Figure 28.



Figure 28 - MEP Bandsaw 281 ccs/MDE [70]

Representative examples of the resulting pieces are shown in Figure 29.



Figure 29 - several AlSi10Mg pieces: long cut, cubic cut and pyramid cut

3.1.2 AlSi9Cu3

Table 10 reports the nominal composition range of the AlSi9Cu3 alloy according to UNI EN 1706; the corresponding EN designation is EN AC-46000.

Table 10 - EN AC-46000 composition ranges [69]

AlSi9Cu3								
wt.%	*Si*	*Fe*	*Cu*	*Mn*	*Mg*	*Zn*	*Ti*	*Al*
	8- 11	*<1.3*	*2-4*	*< 0.55*	*0.05 – 0.55*	*< 1.2*	*< 0.25*	*Bal.*

The material was supplied as a scrapped cast automotive component, namely a gearbox housing from a medium-sized car model line (Figure 30). Owing to the volume limitations of the gas-atomizer crucible, only one half of the component was used in this study.

One half of an identical gearbox housing had previously been investigated in a previous PhD study by Elisa Fracchia [24]. Samples of the as-received metal were analyzed using the SEM-EDS system described in Section 3.3, and the resulting semi-quantitative composition is reported in Table 11.

To note, these composition data are taken from a previous study and refer to an identical component, but not necessarily to the exact same half examined in the present study; this limitation should therefore be acknowledged.

Table 11 - AlSi9Cu3 carter, EDS analysis results

AlSi9Cu3 (carter, as is)								
	Si	*Fe*	*Cu*	*Mn*	*Mg*	*Zn*	*Ti*	*Al*
wt.%	*11.67*	*1.04*	*2.49*	*0.31*	*Below the Probe' s sensitivity*	*0.90*	*Below the Probe' s sensitivity*	*Bal.*

Considering the origin of the feedstock as an internally scrapped automotive component, this alloy was selected to assess the feasibility of gas atomization and L-PBF processing for the internal recycling of foundry scrap.

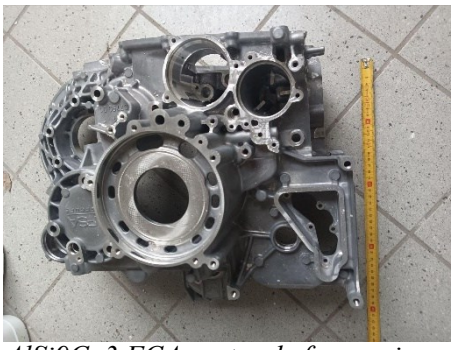


Figure 30 - AlSi9Cu3 FCA carter, before main cuts

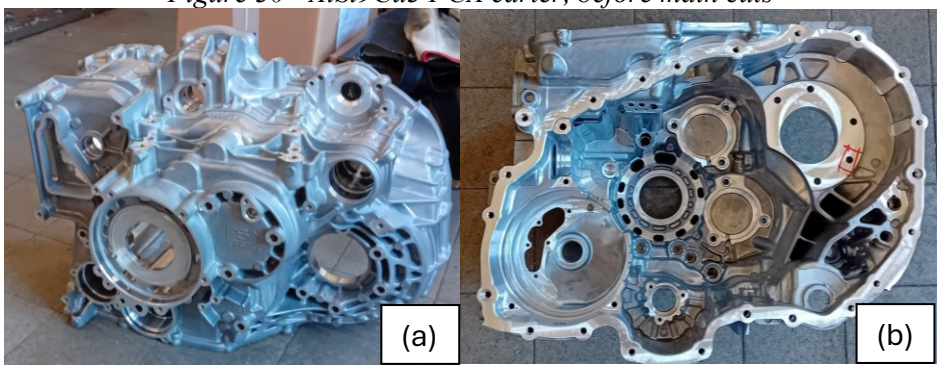
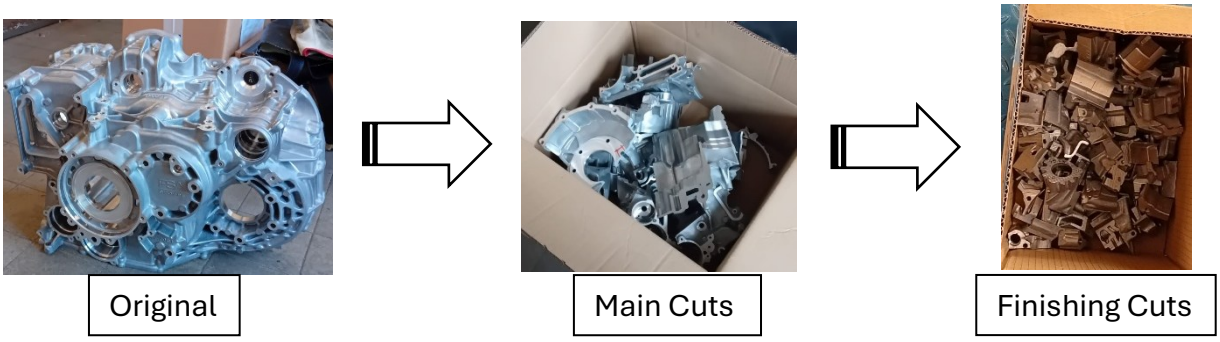


Figure 31 - AlSi9Cu3 FCA carter, before main cuts: external (a) and internal (b) detail.

The casting was subsequently cut into smaller pieces using the table bandsaw mentioned above. In this case, the cutting strategy aimed to obtain smaller and more regular pieces to improve crucible filling and reduce packing inefficiencies caused by the complex geometry of the original component. The final pieces were mainly parallelepipedal or cubic, with characteristic dimensions in the range of 5-10 cm.



Graph 8 - Showcase of the AlSi9Cu3 carter cut's evolution

3.2 Atomization and additional sieving



Figure 32 - Alessandria Plant, several upside-down alumina crucibles

Both alloys were converted into powders using the facilities available in the Additive Manufacturing laboratories of the Interdepartmental Center IAM, Alessandria Campus, Politecnico di Torino. The gas atomizer was a Phoenix Scientific Industries HERMIGA 100 VIGA system (Figure 35), with a crucible capacity of 4 -10 kg and the possibility of additional feeding through a lateral chute. The powders were collected in two containers:

• Primary hopper: main powder fraction, corresponding to the heavier fraction collected during atomization.
• Secondary hopper: finer and lighter fraction of the atomized material.

To limit the risk of contamination from powders remaining from previous atomization runs, only the material collected from the primary hopper was used for the subsequent analyses and processing steps.



Figure 33 - Sieve shaker AS200 by

Both alloys were melted in alumina crucibles (Figure 32) by induction heating.
The following vacuum sequence was employed: the inner portion of the atomizer (both the tower and melt chamber) were brought to a pressure state of was initially brought to a pressure of $6*10^{-2}$ mbar, after which the the feedstock was first heated until it reached 80% of its Melt Temperature at a pressure of 24 mbar; argon was then backfilled into both the furnace and atomization tower at 400 °C, to protect the melt and remove outgassed species, until the melt chamber reached room pressure (1013.25 mbar).
Melting started when the temperature reached approximately 580 °C. The temperature then was increased until the thermocouple reading reached up to 850 °C, held for 15 min to promote thermal homogenization, and the atomization chamber was subsequently pressurized to 1.25 bar.

The molten alloy was atomized through a De Laval nozzle using argon at an atomization pressure of 25 bar.
The argon mixture used for both atomization processes was of Grade 5.0 purity, corresponding to an argon content of at least 99.999%.

The atomized powders were retrieved the following day, after allowing sufficient time for cooling and for the settling of suspended particles. The atomization and post-processing steps for the two alloys are described in further detail in the following sections.
For this specific case of L-PBF processing, the target powder size range was 25-63 µm: this was chosen in order to subsequently produce the print using the EOSINT M270 model L-PBF printer present inside the IAM@PoliTo center (see Chapter 3.4). Therefore, sieving and particle-size distribution measurements were used to separate and verify the suitable powder fraction.
Sieving was performed under a fume hood using an AS200 Retsch sieve shaker (Figure 33). The sieves used had nominal mesh sizes of 120, 63 and 25.
Before sieving, the powders were dried to reduce moisture-related µm agglomeration and clogging of the sieves. A vacuum-assisted oven was used between consecutive sieving sessions: the oven itself was kept at 50 °C with a pressure in the low-to-medium vacuum range (1.3 to 1.3×10^{-3} mbar), kept using a rotary pump. The powders were kept inside an aluminum tray in this oven over the course of a 12-hour period, after which they were removed from the chamber and stored away into several sealed plastic containers at room conditions.

To evaluate the particle-size distribution (PSD) of the powder's fractions over the course of the sieving period, a Malvern Mastersizer 3000 laser-diffraction particle size analyzer was employed (see Figure 34); an Aero unit was employed to disperse the dry powders during the analysis.



Figure 34 – Malvern Panalytical Mastersizer 3000 [71]

3.2.1 AlSi10Mg



A mass of 2.794 kg of AlSi10Mg feedstock was loaded directly into the melting crucible.
After atomization, a grey solidified oxide-rich dross layer was removed from the inner surface of the crucible (Figure 36).
According to the literature [72], these residues are mainly related to surface oxides that remain on the melt surface (Figure 37) because of their higher melting temperature and are subsequently retained on the crucible surface after atomization.

Figure 35 - Alessandria Plant gas atomizer, sideview

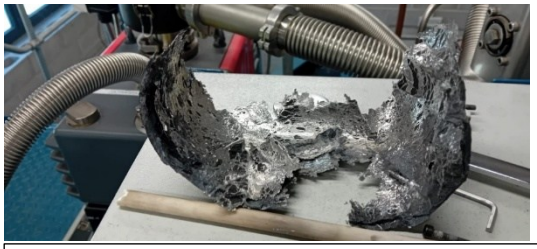


Figure 36 - AlSi10Mg dross layer, retrieved from the crucible after cooling



Figure 37 - Crucible during the melting process, AlSi10Mg dross layer

3.2.2 AlSi9Cu3

A mass of 2.863 kg of AlSi9Cu3 feedstock was loaded into the melting crucible. Because the irregular shape of the feedstock obstructed complete loading, the lateral chute was employed to add part of the feedstock material (834 g)
A higher amount of oxide-rich dross was observed for this alloy than for AlSi10Mg (Figure 38). This was tentatively attributed to the larger surface-to-volume ratio of the gearbox-housing scrap, which may have introduced a higher amount of surface oxides into the melt charge.



Figure 38 - Crucible during the melting process, AlSi9Cu3 dross layer

From this step onwards, only the powder fraction in the 25-63 µm range was used for both alloys.

3.3 Further Powder characterizations

The morphology, particle-size distribution, microstructure and flow behavior of the powders are critical for assessing their suitability as L-PBF feedstock. Therefore, additional tests were carried out on the sieved powders. Flowability and XRD analyses were performed according to ISO/ASTM 52907:2019(E) and ASTM F3049-14.
For microstructural characterization, powders from both alloys were mounted in a nonconductive epoxy resin (Figure 39), polished, and analyzed by scanning electron microscopy (SEM) equipped with energy-dispersive X-ray spectroscopy (EDS). The instrument was a Zeiss EVO 15 SEM equipped with an Oxford Ultim Max 40 EDS detector. EDS was used only for semi-quantitative analysis of the main phases.
Specimens for SEM-EDS were manually polished using the following sequence of sandpaper grits and polishing suspensions:

- 400
- 600
- 1000
- 2100
- 3 µm diamond suspension
- 1 µm diamond suspension
- Colloidal silica suspension



Figure 39 - AlSi10Mg sample, before metallization

After polishing, the upper surfaces of the mounted samples were coated with gold, and a strip of carbon tape was applied to the side to improve electrical conductivity during SEM observation; only after this process of metallization the polished samples were analyzed through EDS.
In addition to the polished cross-sections, two stubs containing unpolished sieved powders were analyzed using the same SEM-EDS system. These observations were used to assess

powder morphology and to compare the chemical response of the particle surfaces with that of the polished cross-sections.
Powder cross-sections were observed using a backscattered electron (BSE) detector, whereas the morphology of the unpolished powder particles was investigated using secondary electron (SE) imaging.

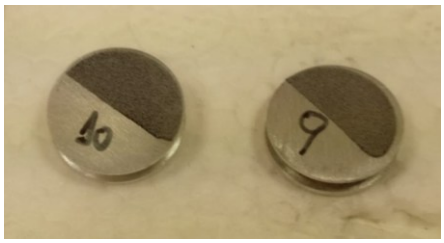


Figure 40 - AlSi9Cu3 (right) and AlSi10Mg (left) unpolished powder samples

Rheological measurements were performed using a Freeman Technology FT4 powder rheometer equipped with a shear-cell module (Figure 41). Tests were carried out on powder samples of both alloys in the 25-63 µm size range, following ASTM B331-20, ASTM B527-23, ASTM B212-21 and ASTM B964-23.



Figure 41 - Freemantech FT4

Before flowability testing, the powders were dried in a climatic chamber for 2 h. They were then conditioned in the FT4 test vessel, and the conditioned bulk density (CBD) was measured. The powders were gently mixed, loaded into the 25 mL test chamber, and the excess powder was removed using the instrument blade.
The machine evaluated the CBD's value with the following formula:

$$BSD = W/V$$

where:
W= measured weight of the loaded powder (g)
V= chamber's volume, 25 ml

The conditioning step is intended to standardize the initial powder state and improve repeatability when comparing different materials.

The test consisted of 11 measurements. In each measurement, the instrument blade moved through the powder bed at a controlled speed while the energy required for the motion was recorded. The first seven cycles were performed at a blade-tip speed of 100 mm/s, whereas the final four cycles were performed at progressively lower speeds, down to 10 mm/s. Changes in the required energy provide information on powder cohesion and flow-rate sensitivity.
The values obtained through the analysis are as follows:

- **Basic Flowability Energy (BFE)**: energy required to move the instrument blade through the conditioned powder under the specified test conditions. It is commonly used as a dynamic-flow descriptor.
- **Stability Index (SI)**: this value indicates change in flow behavior over repeated analysis cycles. It is evaluated by dividing the BFE value of the first cycle by the value for the seventh: value outside the range of 0.9 – 1.1 indicate powder instability.
- **Flow Rate Index (FRI)**: descriptor of the sensitivity of powder flow to changes in blade speed, evaluated from the final four test cycles.

- **Specific Energy (SE)**: Flow energy under low stress conditions. It's measured in the last 4 tests.
- **Conditioned Bulk Density (CBD):** bulk density measured after the FT4 conditioning step. It is related to, but not identical to, apparent density as measured by standard Hall or Carney methods.

The rheological results were subsequently compared with reference ranges reported in the literature and in technical documentation for powders intended for L-PBF processing.

The final powder characterization test was XRD analysis, aimed at identifying the phases formed during atomization. This analysis was performed by the Department of Chemistry of the Università degli Studi di Torino (UNITO), Electronic Microscopy Laboratory "Gianmario Martra".
This analysis is further described in Chapter 3.4.3.

3.4 L-PBF

The 25 – 63 μm range of powders is considered ideal for L_PBF and considering both the machine and recoating system, this fraction of the sieved powders was employed in the samples manufacturing for each alloy [74].
The L-PBF system used was an EOSINT M270 Dual Mode model produced by the company Electro Optical Systems (EOS), see Figure 42. The process for both alloys was conducted inside the Integrated Additive Manufacturing Interdepartmental Centre of the Politecnico di Torino (IAM@PoliTo).

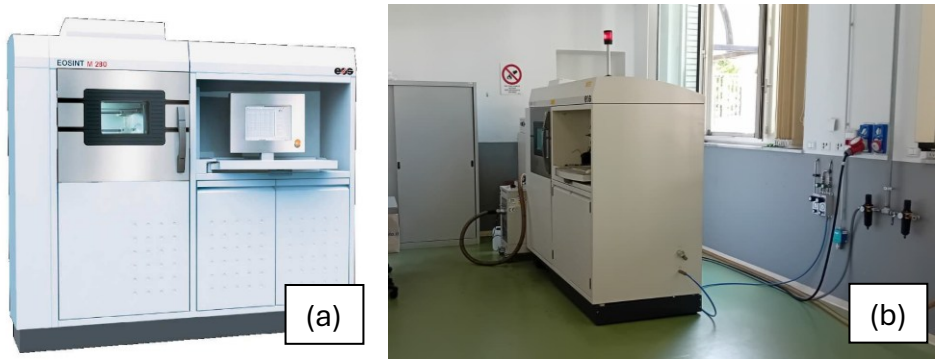


Figure 42 - EOSINT M270 model: as it appears in a commercial brochure [75] *(a) and as it is inside the IAM@PoliTo laboratory*

Simple cubic shapes were produced to evaluate both the printing quality of the powders and their mechanical properties; these samples were subjected to microstructural analyses and microhardness tests.
Six cubic samples of 1 cm per side were obtained from each alloy: three were to be studied as-built, while the other half was kept aside in order to conduct a subsequent series of thermal tests in a future work. See Figure 43.

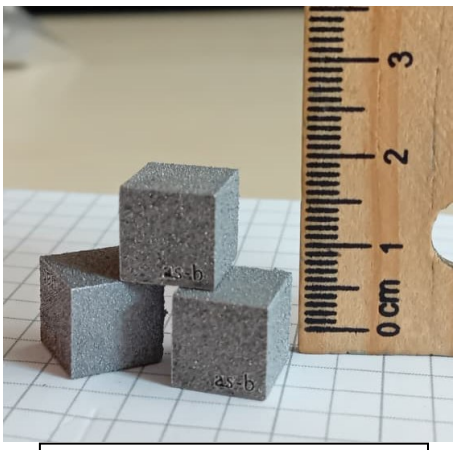


Figure 43 - three as-built AlSi10Mg cubic samples

The main L-PBF process parameters are summarized in Table 12 showcases the chosen parameters: all the samples were produced employing the same values.

Table 12 - EOS M270 main process parameters used in this study

Parameter	*Values*
Scanning strategy	5 mm stripes, 67° rotation between each layer
Hatching distance [µm]	0.17
Layer thickness [µm]	30
Laser power [W]	195
Laser Spot Size [µm]	100
Speed [mm/s]	800
Atmosphere	Argon
Platform Temperature [°C]	100 [76]

Below each cube, a support structure of 3 mm was fabricated; this structure, built using a scanning strategy that allowed it to be porous, was employed for a couple of reasons:

- By employing it, the removal of each printed part would not require the use of Electrical Discharge Machining (EDM); this is instead necessary with parts that have been built directly on the printer's baseplate.

- The support structures allow the production of components with a complex shapes: by employing it in this case study, the same parameters can be employed with more complex geometries without any crucial modification.

3.4.1 L-PBF Sample Preparation for characterization

The following picture (Figure 44) highlights the 3D Cartesian coordinate Scheme on a cube:

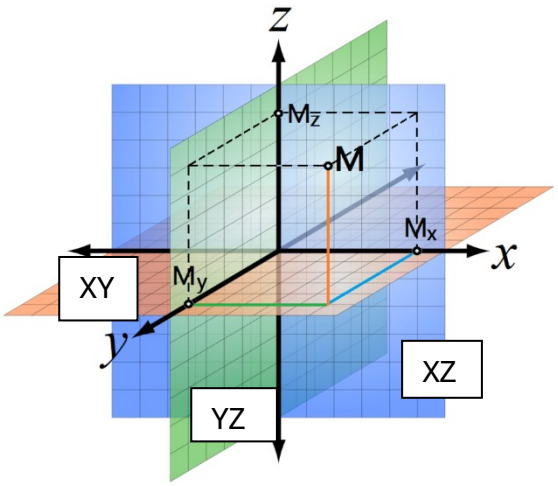


Figure 44 - 3D Cartesian coordinate model: plane names in the text boxes

To establish the impact of the building direction (z axis) on the component, two cubes of each as-is printed alloy were analyzed: they were cut to evaluate respectively the XY and the YZ planes of both alloys, as the L-PBF process produces innately anisotropic components.

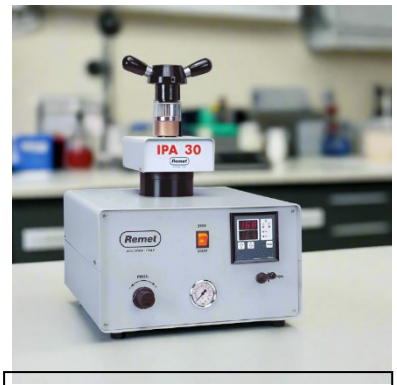


Figure 45 - IPA 30 model embedding press (by Remet) [77]

The cubes were cut using a Brillant 220 model cut-off machine, produced by QATM (see Figure 46): the machine was setup with a Presi-made CERMET blade (Type AOF II).

Afterwards, each half of each cube was embedded inside a conductive epoxy resin form, using an IPA 30 embedding press (see Figure 45).
These samples were manually polished using the following sequence of sandpaper grits and polishing suspensions:

- 400
- 600
- 1000
- 2100
- 3 µm diamond suspension
- 1 µm diamond suspension



Figure 46 - Brillant 220 model cut-off machine [78]

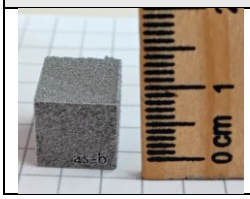
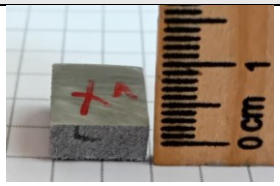
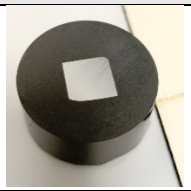
One half of the samples underwent optical Microstructural analysis, after which they were subjected to FE-SEM analysis: this batch of testing was conducted after the additional steps of regular colloidal-silica suspension polishing and super-finishing using a vibration polisher. The latter treatment was conducted using a Presi-made model VibroTech 300 automatic polisher paired with a 30 nm colloidal silica solution.



Figure 47 - VibroTech 300 automatic polisher [5]

Table 13 showcases the evolution of the surface appearance of the AlSi10Mg cubic samples throughout the polishing process.

Table 13 - Polishing stages for the mounted AlSi10Mg sample, XY plane

Initial as-built condition	*Cut sample*	*After 2400 grit paper*	*After 1 µm diamond suspension*
			

The other half of the samples were kept aside to conduct micro-hardness testing characterizations: these halves were again polished up to the 1 µm diamond suspension.

3.4.2 Microstructural analysis

3.4.2.1 Optical Analysis, Porosity

For each alloy's XY and YZ polished cross-section sample several pictures were taken using a combined optical microscope-camera set-up (DMI 5000 by Leica, see Figure 48) and its proprietary software suite (LAS X); the chosen standard was ASTM E1245.

Each picture was taken employing a combined magnification of 200x; afterwards, each image was ported to the image processing software ImageJ (by the National Institutes of Health (NIH) US agency; version 1.54t 16 May 2026).

Pictures were taken both along the cross-section's central area and shot closer to the edges of the sample.
Each image was evaluated as an 8-bit type, thus allowing us to employ the gray-scale gradient to differentiate actual porosities from other types of surface marks; Otsu's method was chosen as the



Figure 48 - DMI 5000 optical microscope [79]

thresholding technique, allowing us to produce a mask capable of differentiating the picture's pixels in two categories ("porosity" and "fill" pixels). See the Figures below.

The porosity was evaluated by the program by dividing the amount of "porosity" pixels by the total number of pixels present in the studied area.

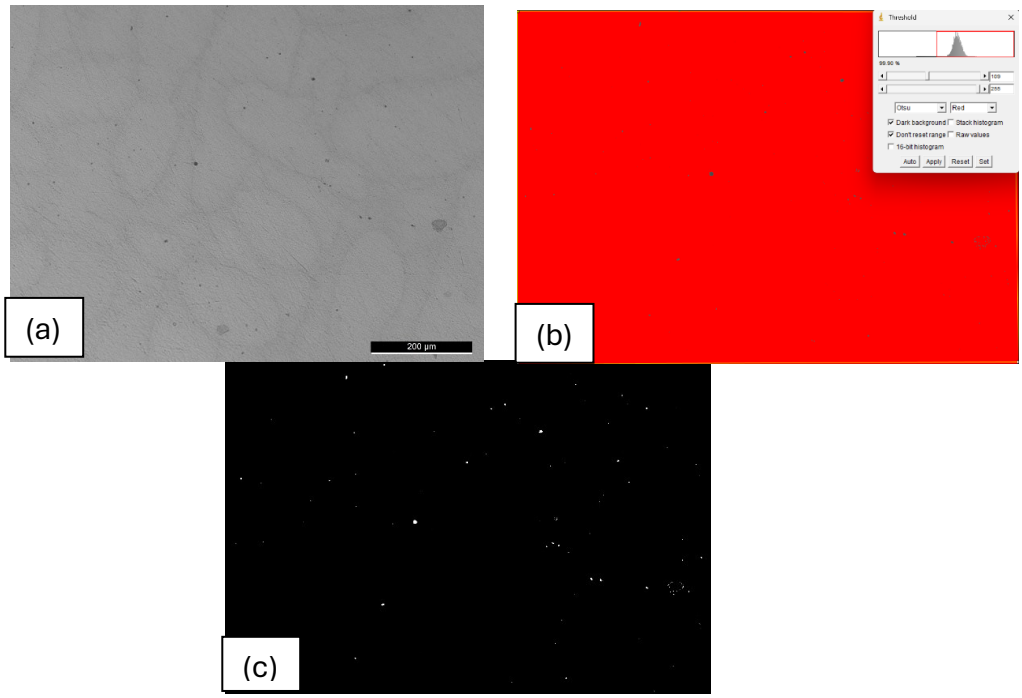


Figure 49 - *Example of image processing performed to evaluate the porosity of the AlSi10Mg XY plane. (a) Image obtained with the optical microscope. (b) A threshold level was set to differentiate the darker areas (porosities) from the lighter ones (AlSi10Mg). (c) The white areas correspond to the porosities. Using the ImageJ software, it is possible to calculate their area and pixel-percentage.*

For each set of measurements, the following values were also evaluated:

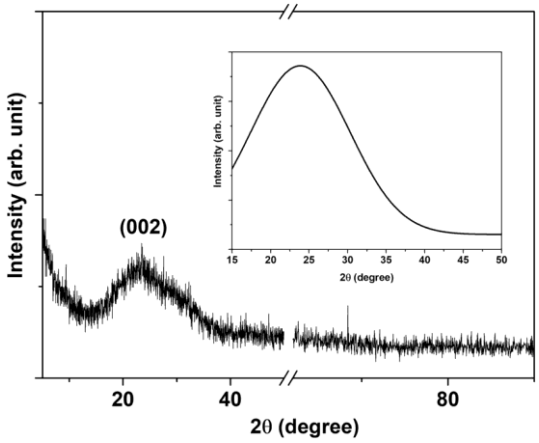
- Mean Value
- Standard Deviation (SD)

Each image was also analyzed, with the aim of finding abnormal features in the alloy's microstructure and to observe the melt-pools and layering of the samples structure.

3.4.3 XRD Analysis

The polished YZ samples of both alloys underwent a cycle of XRD analysis, to detect the crystalline phases present in both alloys and to compare them to what is found inside analogue secondary alloys produced with more traditional means (i.e. casting).
The analysis works by measuring the diffraction of X-rays (originating from an X-ray beam) along the sample surface and comparing the results to known-spectra tables: peaks are labeled following the datasets of the International Centre for Diffraction Data (ICDD).

The results of this analysis are usually provided as a plot diagram: the diffraction peaks are plotted as 2θ (theta) angles, which represent the angular position of the diffracted beam relative to the incident X-ray beam, typically using Cu Kα radiation (λ = 1.5406 Å) as the reference X-ray source. The peak positions (2θ) are characteristic of the crystal structure and are compared with reference patterns for phase identification (see Graph 9).
The typical information depth for this analysis encapsulates the 1 to 100 µm range, depending on the targeted material.



Graph 9 - XRD plot of pristine graphene [80]

The analysis was conducted by the Department of Chemistry of the Università degli Studi di Torino (UNITO).

3.4.4 FE-SEM

The FE-SEM microscope of Figure 50 was employed to conduct two types of analysis on both alloys:

- EDS
- EBSD

The EDS analysis (Energy-Dispersive X-ray Spectroscopy) is used to determine the elemental composition of a material by measuring the characteristic X-rays emitted when the sample is bombarded with an electron beam: this helps in determining whether the printing process itself caused a variation in the composition balance of the alloys. The information depth for this analysis is usually 1–2 µm.

The EBSD (Electron Backscatter Diffraction) measurements are used to determine the crystallographic orientation, grain structure, phase distribution, and texture of crystalline materials by analyzing electron backscatter diffraction patterns generated by the scanning electron microscope (SEM): this grants the ability to produce maps and images



Figure 50 - *S9000G model FEG-SEM (by Tescan)* [81]

clearly highlighting the microstructure of the samples' crystal lattice, thus enabling the comparison between the output of the L-PBF process and the one of more conventional casting strategies.
To perform the EBSD analysis, samples inside the SEM have been tilted by 70° and scanned using an electron beam set at 20 kV, using a step size of 1–2 µm. Each sample had an analyzed area spanning 500x750 μm^2.
To evaluate the grain boundaries, the following scale was employed: [82]

- **$1° \leq \theta \leq 10°$:** low angle grain boundaries, caused by misorientation between adjacent grains (LAGB)
- **$\theta > 10°$:** high angle grain boundaries (HAGB)
- **$\theta = 60°$:** twinning grain boundaries

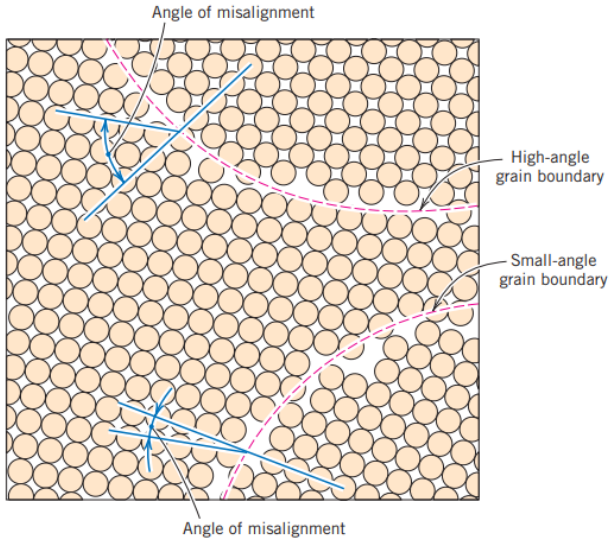


Figure 51 - *Schematic diagram showing small and high-angle grain boundaries and the adjacent atom positions.*[82]

The combination of EDS and EBSD measurements allow for a more comprehensive description of the sample's microstructure.
The information depth for this analysis ranges between 10 and 50 nm (reaching up to ~100 nm depending on material and beam conditions). [83]
Since the crystallization behavior for both alloys is strongly related to the printing parameters (especially the building direction), these analyses focused mainly on the YZ samples.

3.4.5 Mechanical analysis: microhardness

To better understand the mechanical qualities of the printed products, hardness was chosen as a useful analytical assessment: for each alloy's main direction (XY and YZ), two samples were prepared and tested. Afterwards, the obtained hardness values were compared to the ones found in literature, referring to both analogue cast secondary and primary L-PBF alloys.

The chosen standard was ISO 6507-1:2023, meaning the Vickers micro-hardness test: using a square-based diamond pyramid indenter, a fixed load is applied on a flat surface of the sample; to obtain an even surface, the samples were prepared following the guidelines previously described in Chapter 3.4.1.
After the load is applied for a certain amount of time (usually below 20 seconds), the indenter retracts, thus unloading the surface. See Figure 52.

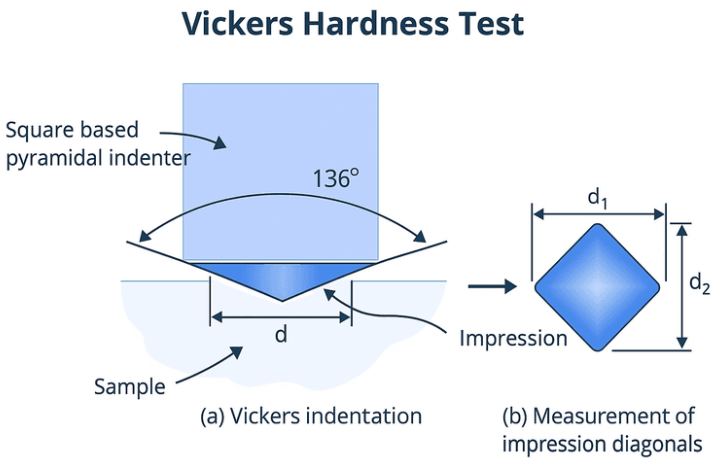


Figure 52 - Vickers Hardness, general scheme [84]

The surface is then analyzed, either by an operator using a set of lenses or by the machine itself: after a successful run, a diamond-shaped indent can be observed; by measuring the length of each of the diamonds diagonals and applying the formula written below, the material's microhardness Vicker can be retrieved:

$$HV = \frac{1.8544 * F}{d^2}$$

Where:

- HV = Vickers hardness number [kgf/mm^2]
- F = applied test force [kgf]
- d = average length of the two indentation diagonals [mm]



Figure 53 - HVS-1000 Digital Micro Vickers hardness tester

An HVS-1000 Digital Micro Vickers hardness tester was employed to conduct this analysis (see Figure 53).
The load was set at 200g, paired with an indentation time of 15 seconds.
To obtain repeatable values, each sample was analyzed 10 times: from this data set the mean value was obtained, coupled with the standard deviation.

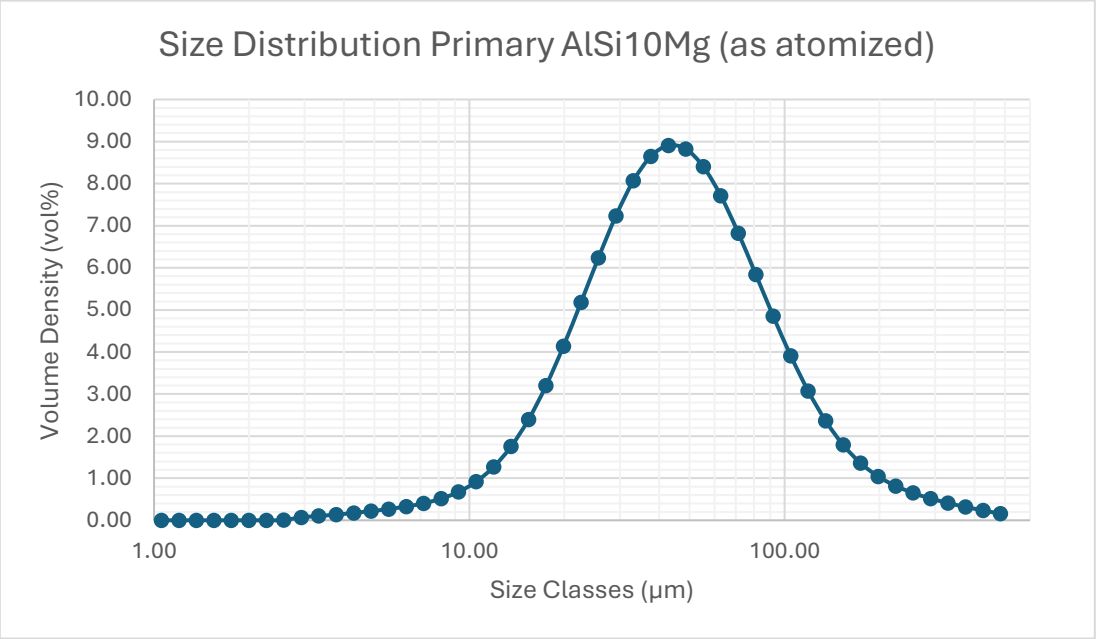
4 RESULTS AND DISCUSSION
4.1 Powder Analysis
4.1.1 PSD
4.1.1.1 AlSi10Mg
The atomization yield was calculated as the ratio between the total mass of atomized powder and the mass of feedstock loaded into the crucible. For AlSi10Mg, the resulting yield was 94.16 wt.%.

Table 14 - AlSi10Mg atomization, yielded weights

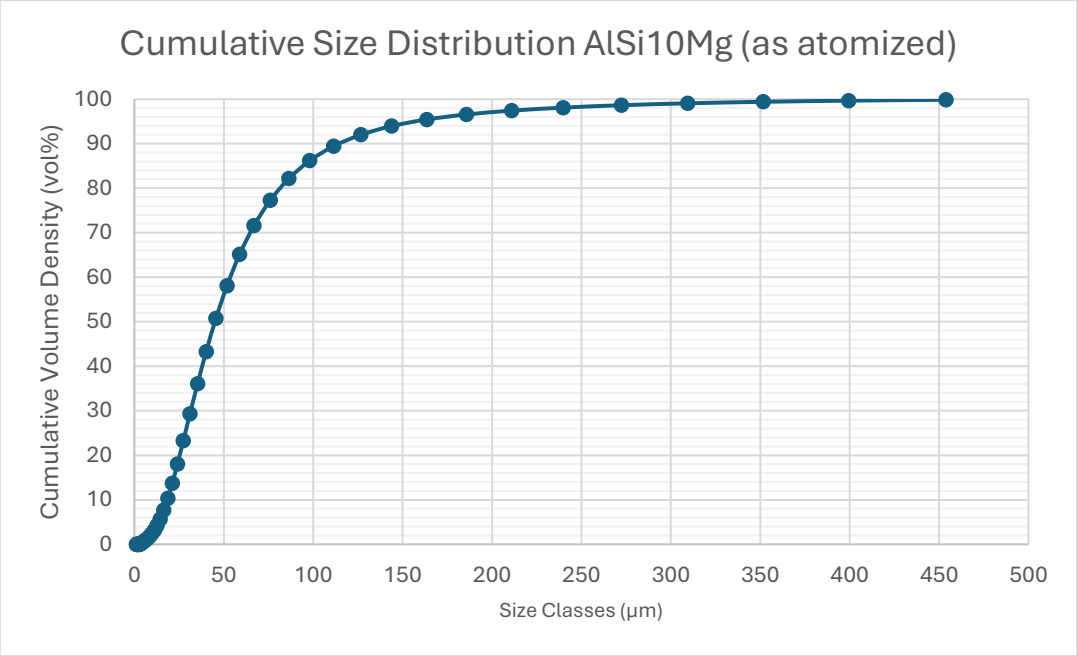
Type	*Weight (g)*
Primary Hopper	2261.5
Secondary Hopper	368.6
Total	2631
Slag	12.1

Table 14 summarizes the mass balance of the atomized material.
The particle-size distribution (PSD) of the primary-hopper powder was then measured, employing the Laser diffraction Particle Size analyzer mentioned in Chapter 3.2.

Three samples were analyzed and the mean volume-based size distribution, together with the cumulative distribution, is reported in Graphs 10 and 11.
The as-atomized powder contained a substantial fraction of particles both below and above the target size range, with D10 = 18.4 µm, D50 = 45 µm and D90 = 115 µm.



Graph 10 - Size Distribution of the primary AlSi10Mg, before sieving



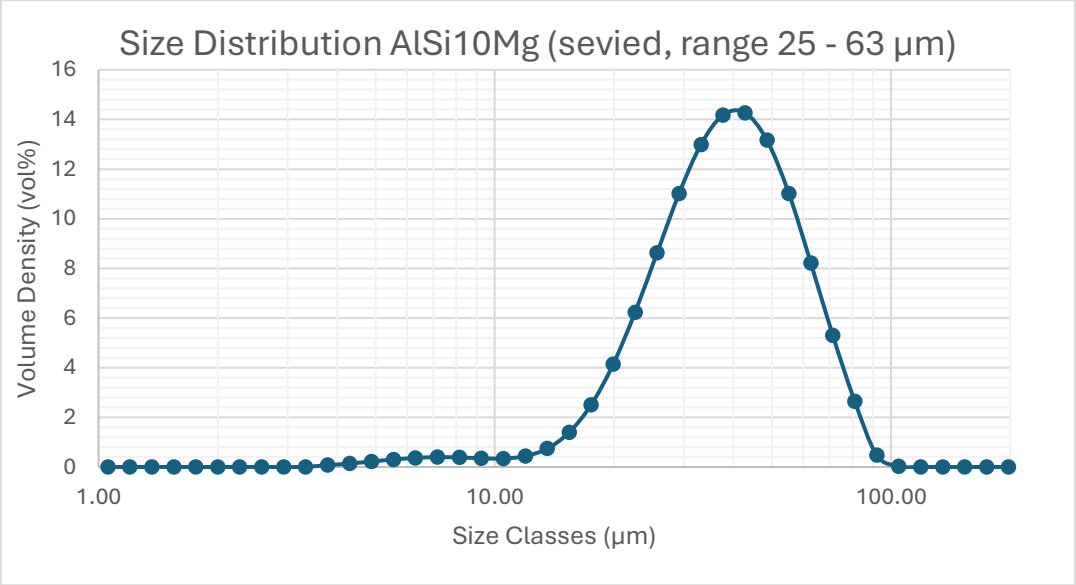
Graph 11 - Cumulative Size Distribution of the primary AlSi10Mg, before sieving

After sieving, the following powder ranges were obtained:

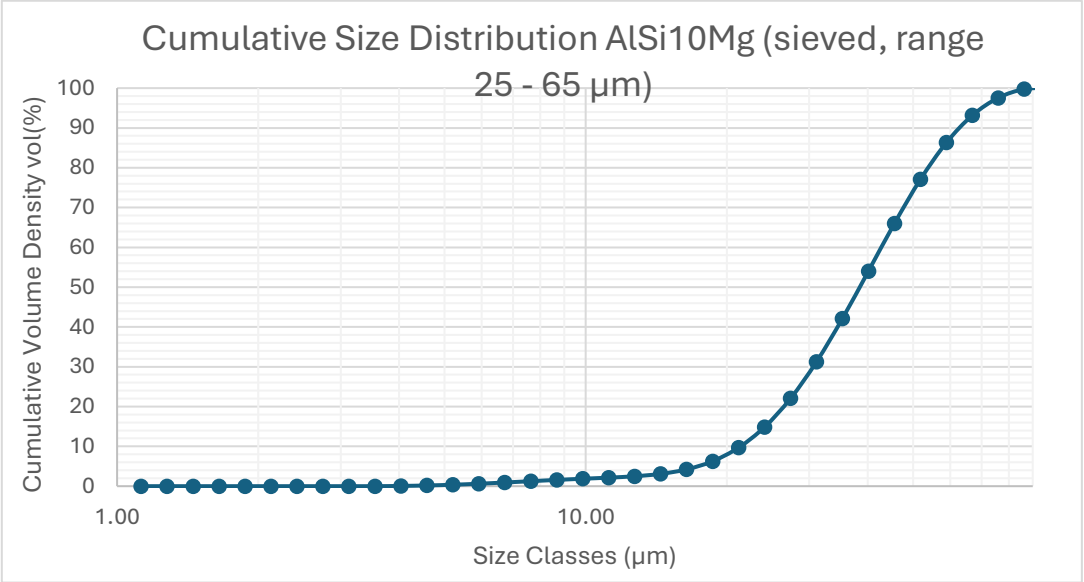
Table 15 - AlSi10Mg sieved powders, size ranges

Size Range (µm)	*Weight (g)*
>106	241.4
63 - 106	868.2
25 - 63	1227.4
<25	186.5

Based on the loaded feedstock mass, 43.92 wt.% of the material was recovered in the 25- 63 µm fraction suitable for L-PBF; considering the total amount of powder retrieved from the primary hopper, 54.26 wt.% fell inside this range instead. The remaining fractions were either unsuitable for the selected L-PBF process window or potentially usable in other powder-based processes, such as metal injection molding (MIM), which typically employs finer powders. [86]
The PSD measured for the sieved 25-63 µm fraction is shown in Graph 12 and 13.



Graph 12 - Size Distribution of the primary AlSi10Mg, after sieving



Graph 13 - Cumulative Size Distribution of the primary AlSi10Mg, after sieving

4.1.1.2 AlSi9Cu3

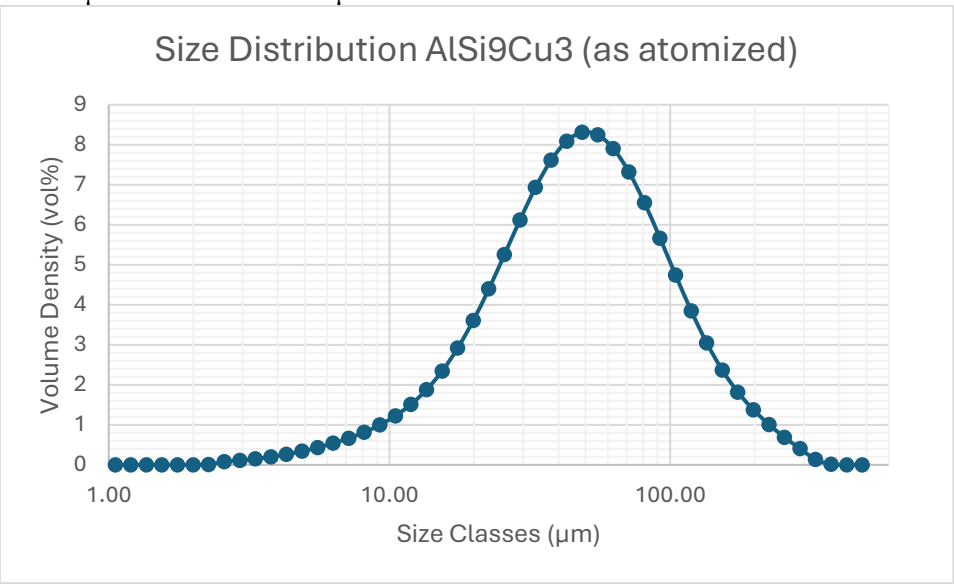
The following table breaks down the output of the atomization:

Table 16 - AlSi9Cu3 atomization, yielded weights

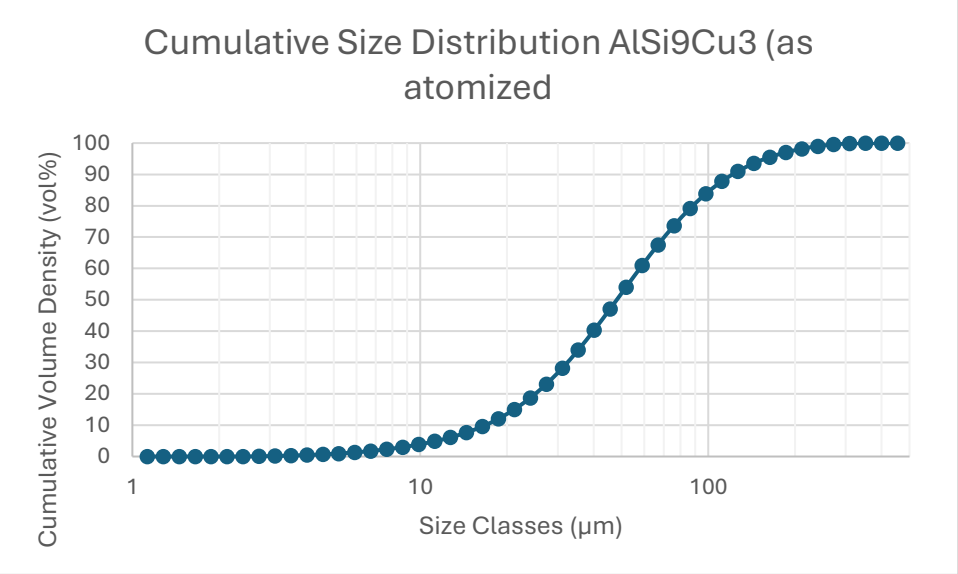
Type	*Weight (g)*
Primary Hopper	2450
Secondary Hopper	250
Total	2700
Slag	16.2

The atomization yield was 94.3 wt.%, slightly higher than that obtained for AlSi10Mg.

The as-atomized AlSi9Cu3 powder contained both fine and coarse fractions, with D10 = 16.8 µm, D50 = 48.1 µm and D90 = 122 µm.



Graph 14 - Size Distribution of the primary AlSi9Cu3, before sieving



Graph 15 - Cumulative Size Distribution of the primary AlSi9Cu3, before sieving

After sieving, the following powder ranges were obtained:

Table 17 - AlSi9Cu3 sieved powders, size ranges

Size Range (µm)	*Weight (g)*
>106	208.1
63 - 106	530.5
25 - 63	1305.6
<25	270

Compared with AlSi10Mg, the AlSi9Cu3 powder showed a lower mass fraction above 63 and 106 µm (Figure 55). A delay of approximately 1 s between melt flow initiation and inert-gas

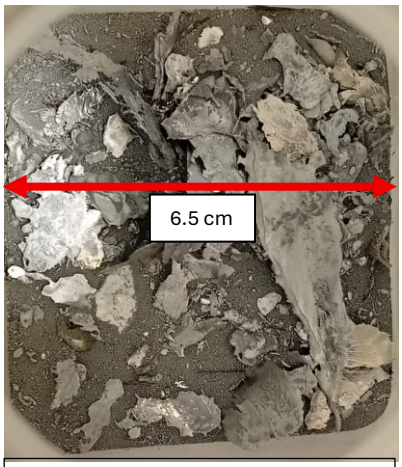
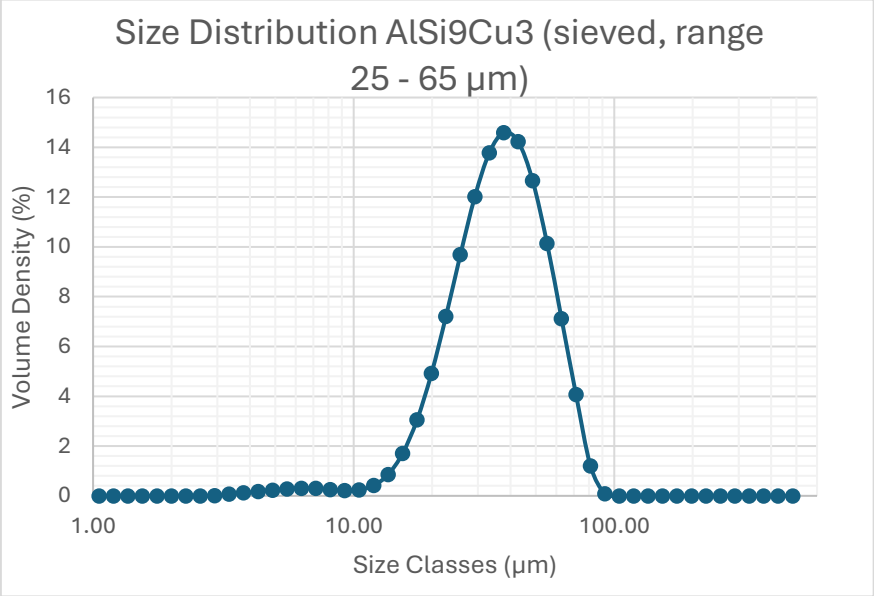


Figure 54 - top-down view of the >106 µm AlSi9Cu3

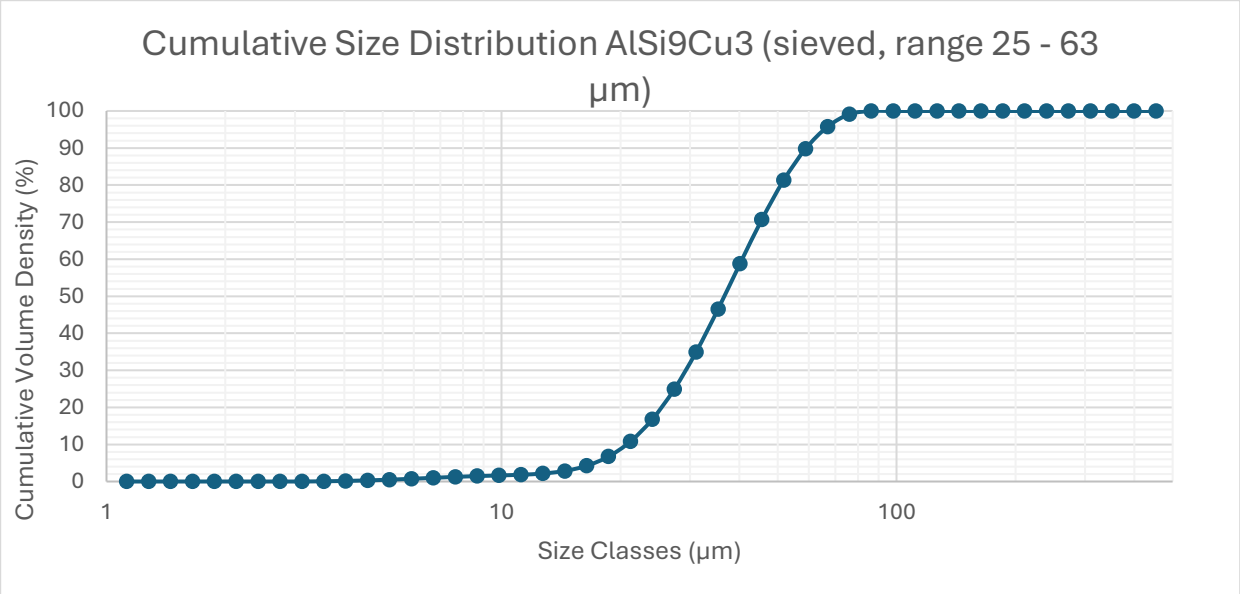
injection may have caused part of the melt to solidify as large splats; nevertheless, the main atomized fraction was broadly comparable to that obtained for AlSi10Mg.

Based on the loaded feedstock mass, 48.36 wt.% of the material was recovered in the 25- 63 µm fraction suitable for L-PBF. The remaining fractions were either unsuitable for the selected L-PBF process window or potentially usable in other powder-based processes, such as MIM.

The PSD measured for the sieved 25-63 µm fraction is shown in Graphs 16 and 17.



Graph 16 - Size Distribution of the primary AlS9Cu3, after sieving



Graph 17 - Cumulative Size Distribution of the primary AlSi9Cu3, after sieving

Table 18 lists a series of relevant granulometry markers for both alloys

Table 18 - Atomized powders; PSD results for as-is and sieved powders, both alloys

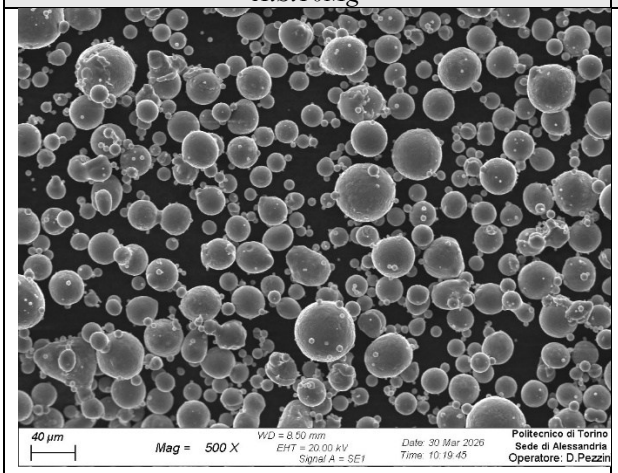
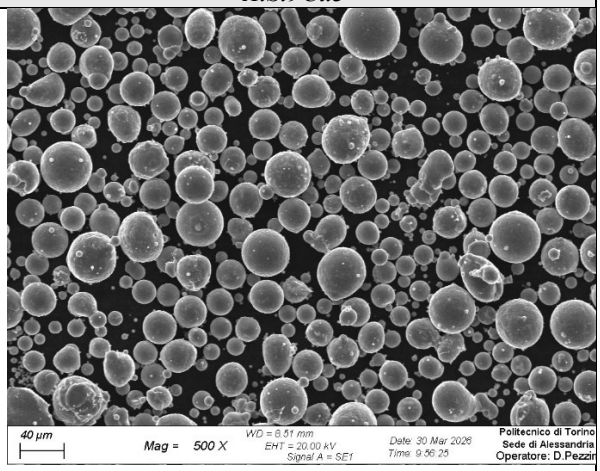
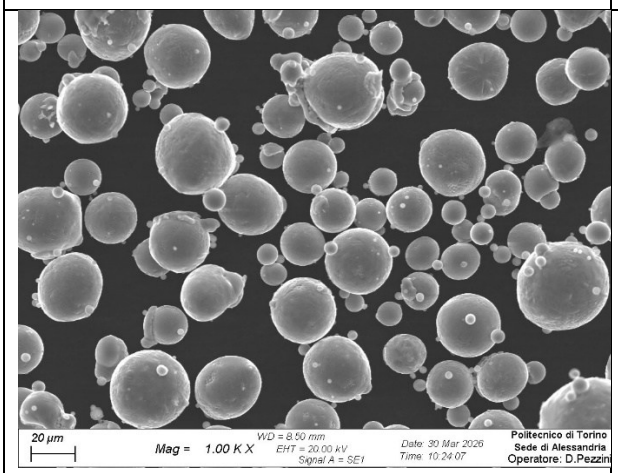
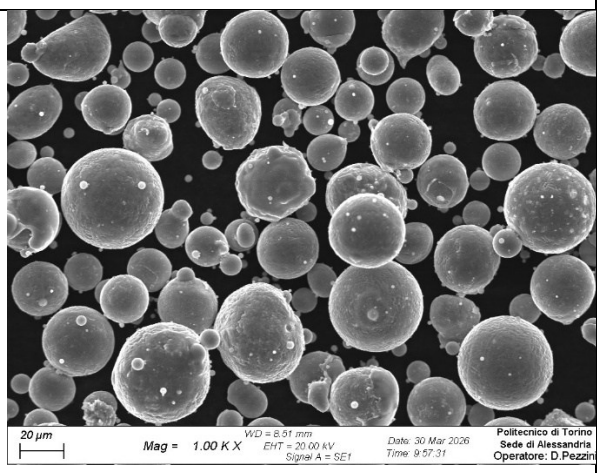
Sample	*Dx (10)*	*Dx (50)*	*Dx (90)*	*% In Range 25 -63 µm*	*% In Range 63 -125 µm*	*% Below 25 µm*	*% Above 125 µm*
AlSi9Cu3 Sieved; 25 - 63 µm	20.7	36.6	59.1	84	7.05	8.94	0
AlSi9Cu3 as Atomized	16.8	48.1	122	50.78	26.24	13.66	9.32
AlSi10Mg Sieved; 25 - 63 µm	21.4	38.4	63.1	81.82	10.06	8.12	1E-14
AlSi10Mg as Atomized	18.4	45	115	56.38	23.18	12.16	8.27

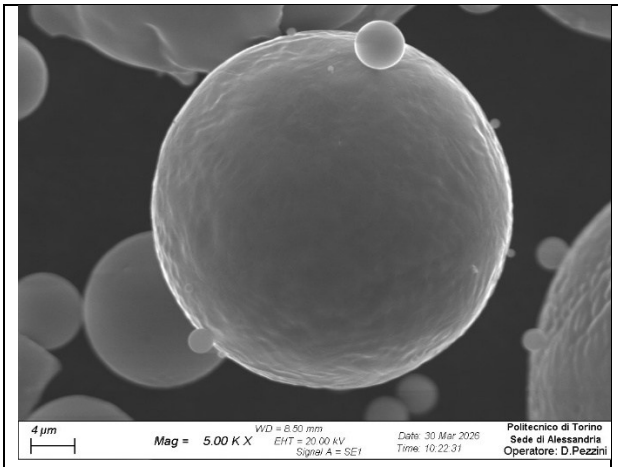
Both atomized alloys produced a substantial fraction within the L-PBF size range. AlSi9Cu3 gave a slightly higher atomization yield and a higher mass fraction in the 25-63 µm window than AlSi10Mg.
After sieving, the two powders showed similar size distributions. The AlSi9Cu3 powder was slightly finer.
For both alloys, the recovered 25-63 µm fractions were comparable with values reported for laboratory-scale gas atomization of aluminum alloys and with commercial AM powder-size specifications [87,88]. This suggests that the selected atomization parameters were reasonably suitable for the two feedstocks.

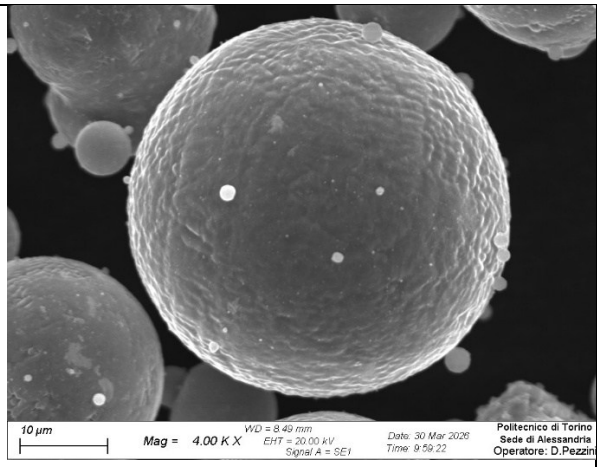
4.1.2 SEM-EDS analysis

Electron microscopy analysis of the sieved powders provided an initial assessment of the atomization quality.
The unpolished powders were observed by SEM using a BSE detector, which provided compositional contrast and allowed the general particle morphology to be assessed. In both alloys, most particles showed a predominantly spherical morphology, with satellites attached to the particle surfaces.
Only a limited amount of surface porosity was observed. This suggests acceptable atomization conditions. Table 19 shows representative SEM images acquired at different magnifications for the unpolished alloy powders.

Table 19 - SEM images of the powders

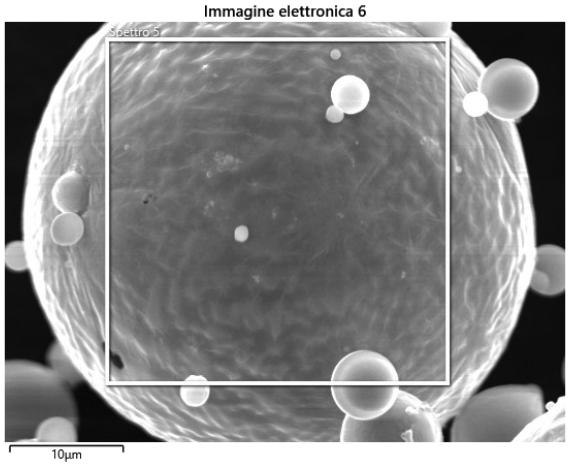
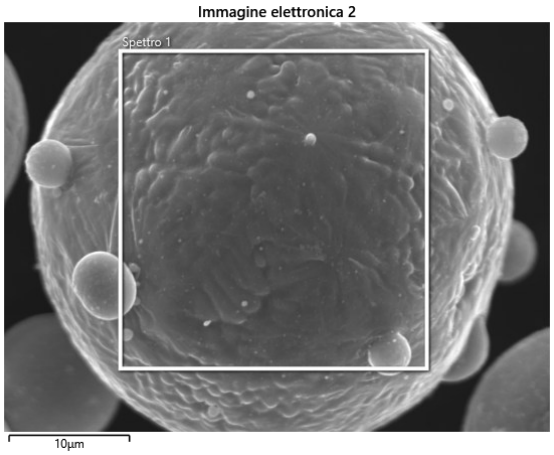
AlSi10Mg	*AlSi9Cu3*
	
	





SEM-EDS analysis of the powder surfaces indicated that the main alloying elements were broadly consistent with the UNI composition ranges. The results are reported in Table 20.

Table 20 - EDS analysis of the powders' surface

Image	*Composition*
 5500x AlSi10Mg	
 6000x AlSi9Cu3	

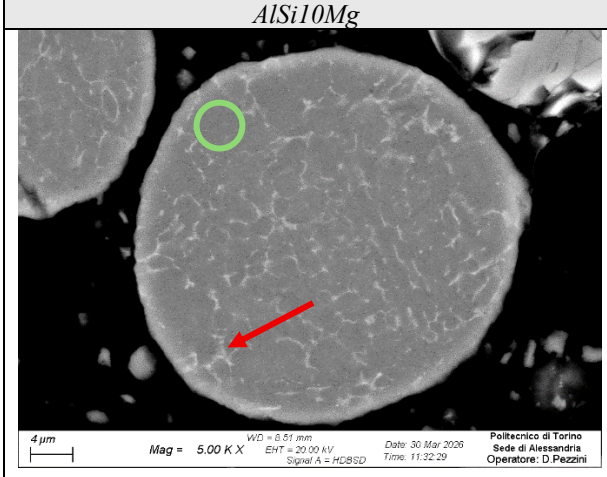
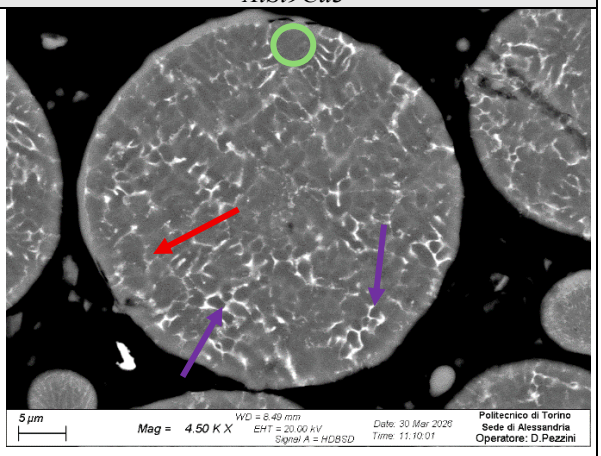
	Al	*Si*	*Fe*	*Mn*	*Mg*
wt.%	88.7	9.6	0.7	0.6	0.4
σ	0.2	0.1	0.1	0.1	0.0

	Al	*Si*	*Cu*	*Zn*	*Fe*	*Mn*	*Mg*
wt.%	85.3	9.2	3.0	1.3	0.9	0.6	0.4
σ	0.2	0.1	0.1	0.1	0.1	0.1	0.0

This analysis could not reliably quantify light elements such as O, N and H. The detection of Fe and Mn on the powder surfaces suggests that Fe- and Mn-containing phases may be present; however, phase identification requires cross-sectional EDS, XRD and/or higher resolution analysis.
The microstructure of the polished powder cross-sections was examined by SEM and EDS (Table 11). BSE imaging was used to enhance compositional contrast among phases with different average atomic numbers.
The images in Table 21 show the distribution of the main alloying elements in each alloy. In BSE imaging, brighter contrast generally corresponds to phases with higher average atomic number [89], although topography, detector settings and sample preparation can also affect the observed contrast.

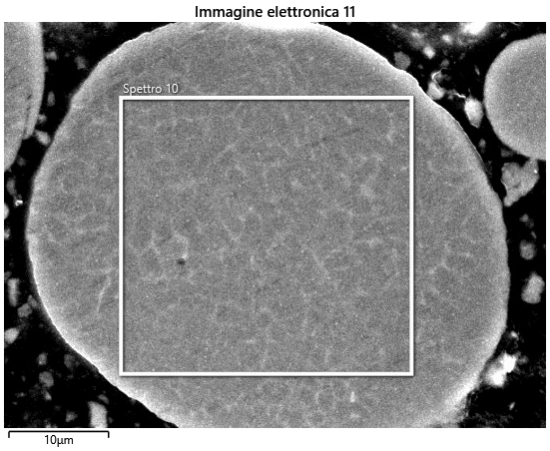
- **AlSi10Mg**: the microstructure mainly consists of an Al-rich matrix with Si-rich eutectic regions and intermetallic phases containing Fe and Mn. The relatively darker regions are associated with lower average atomic number, whereas the brighter features require EDS confirmation for phase assignment.
- **AlSi9Cu3**: the microstructure is broadly similar to that of AlSi10Mg, but with additional bright features attributable to Cu- and/or Fe-rich intermetallic phases. The assignment of these phases should be based on the local EDS spectra rather than on BSE contrast alone.

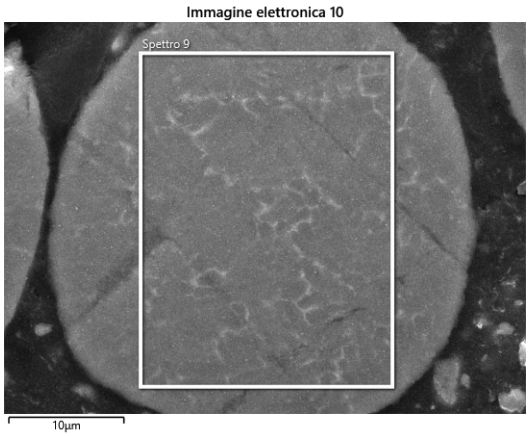
Table 21 - BSD analysis of the powders' cross-section

AlSi10Mg	*AlSi9Cu3*
	

EDS analysis of the powder cross-sections confirmed the presence of Mn and Fe in both alloys, as shown in Table 22.

Table 22 - EDS analysis of the powders' cross-section, one example for each alloy

<table>
<tr><th>Image</th><th>Composition</th></tr>
<tr><td>

5000x
AlSi10Mg</td><td>
<table>
<tr><th></th><th>Al</th><th>Si</th><th>O</th><th>Fe</th><th>Mn</th><th>Mg</th></tr>
<tr><td>wt. %</td><td>88.0</td><td>9.8</td><td>0.8</td><td>0.6</td><td>0.5</td><td>0.3</td></tr>
<tr><td>σ</td><td>0.2</td><td>0.2</td><td>0.1</td><td>0.1</td><td>0.1</td><td>0.0</td></tr>
</table>
</td></tr>
<tr><td>

6000x
AlSi9Cu3</td><td>
<table>
<tr><th></th><th>Al</th><th>Si</th><th>Cu</th><th>Zn</th><th>O</th><th>Fe</th><th>Mn</th><th>Mg</th></tr>
<tr><td>wt. %</td><td>83.6</td><td>9.7</td><td>2.9</td><td>1.0</td><td>1.0</td><td>1.0</td><td>0.4</td><td>0.3</td></tr>
<tr><td>σ</td><td>0.3</td><td>0.2</td><td>0.2</td><td>0.2</td><td>0.1</td><td>0.1</td><td>0.0</td><td>0.1</td></tr>
</table>
</td></tr>
</table>

The following tables report the average composition of each alloy, obtained by combining the values measured on both unpolished particles and polished cross-sections:

Table 23 - EDS results of the AlSi10Mg powder, Median values over 6 analyses

Value	*Al*	*Si*	*Fe*	*Mn*	*Mg*
Mean Content (wt.%)	88.4	10.3	0.683	0.517	0.35
Standard Deviation (SD)	0.37	0.69	0.069	0.090	0.05

Table 24 - EDS results of the AlSi9Cu3 powder, median values over 6 analyses

Value	*Al*	*Si*	*Cu*	*Zn*	*O*	*Fe*	*Mn*	*Mg*
Mean Content (wt.%)	83.7	9.58	3.02	1.27	0.9	1.02	0.13	0.43
Standard Deviation (SD)	1.20	0.36	0.43	0.23	0.43	0.069	0.14	0.047

The relative standard deviation indicates that Mn was detected with high uncertainty in both alloys, especially in AlSi9Cu3. This is consistent with the relatively low Mn content and the semi-quantitative nature of SEM-EDS analysis.

Within the uncertainty of SEM-EDS analysis, both atomized powders were broadly consistent with their corresponding UNI composition ranges (as reported previously in Table 9 and 10).

4.1.3 Rheological tests

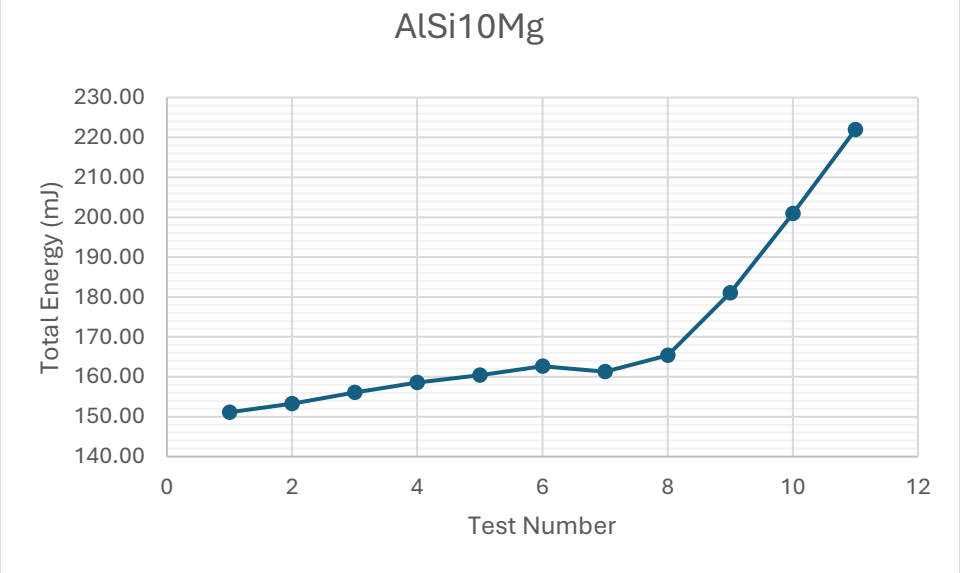
Although many studies report microstructural and mechanical properties for AlSi10Mg and AlSi9Cu3 alloys, complete rheological datasets for recycled gas-atomized powders are less frequently available in open literature and commercial datasheets: data such as the size ranges, SI and the employed shear cell are often excluded from commercial pamphlets and data tables.

Several standards and articles provide recommended ranges for parameters considered relevant to the suitability of metal powders for L-PBF processing. Table 26 summarizes typical values associated with good recoating behaviour.

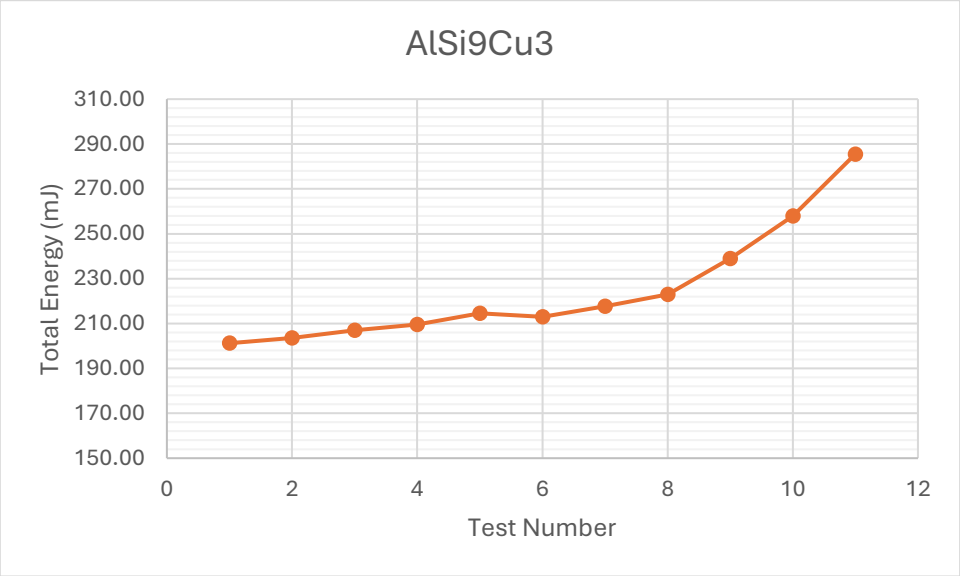
Table 25 - Typical value ranges for good recoating under L-PBF [90, 91]

BFE (mJ)	*SI*	*FRI*	*SE (mJ/g)*
< 200	0.95 – 1.10	1.0-1.3	< 10

Graphs 18 and 19 show the energy required during repeated stirring cycles for both powders.



Graph 18 - AlSi10Mg powder's energy expenditure over repeated stirring cycles



Graph 19 - AlSi9Cu3 powder's energy expenditure over repeated stirring cycles

The results of the rheological analysis are reported in Table 26.

Table 26 - Rheological analysis results for both atomized powders

Material	*BFE (mJ)*	*SI*	*FRI*	*SE (mJ/g)*	*CBD (g/ml)*
AlSi10Mg	161.2487	1.067073	1.342021	1.342021	2.73209
AlSi9Cu3	217.6624	1.081663	1.280393	1.280393	2.232059

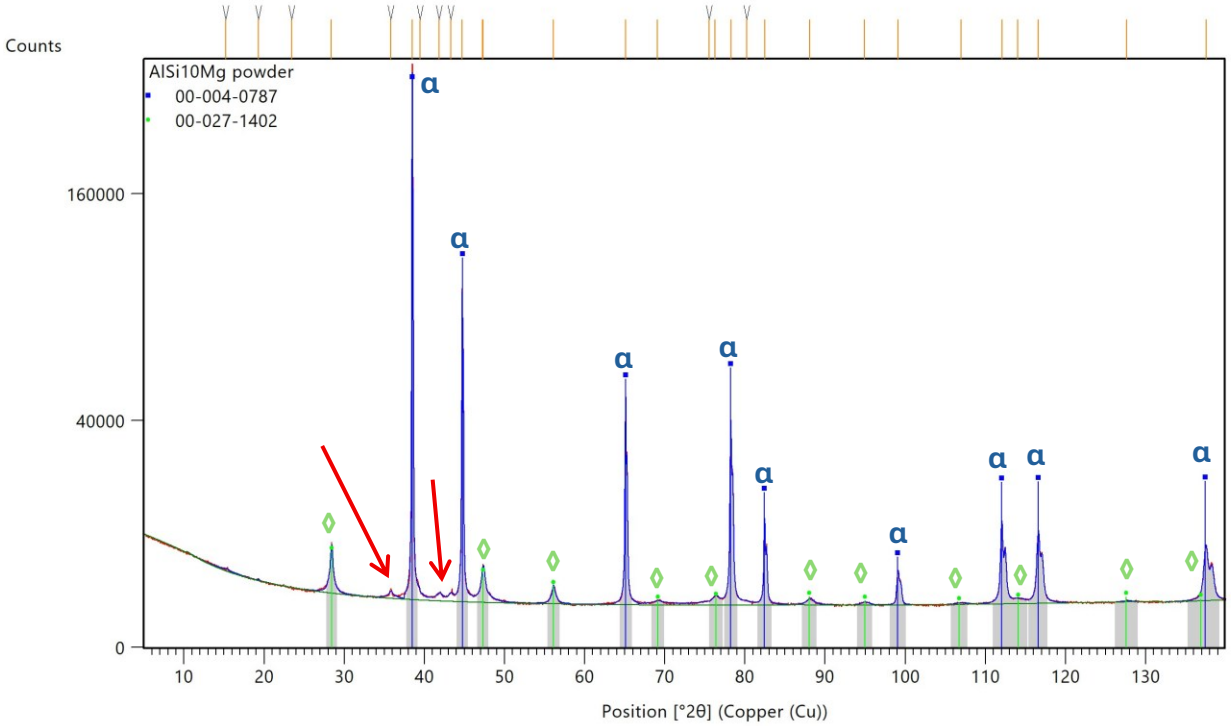
The AlSi10Mg powder exhibits an acceptable FRI, within the 1.3-1.6 range, whereas AlSi9Cu3 shows a lower value and therefore lower sensitivity to flow-rate changes.

The SE values are relatively low for both alloys, with AlSi10Mg slightly higher than AlSi9Cu3. Since SE is measured under low-stress conditions, these values provide an indication of interparticle cohesion and unconfined-flow behavior.

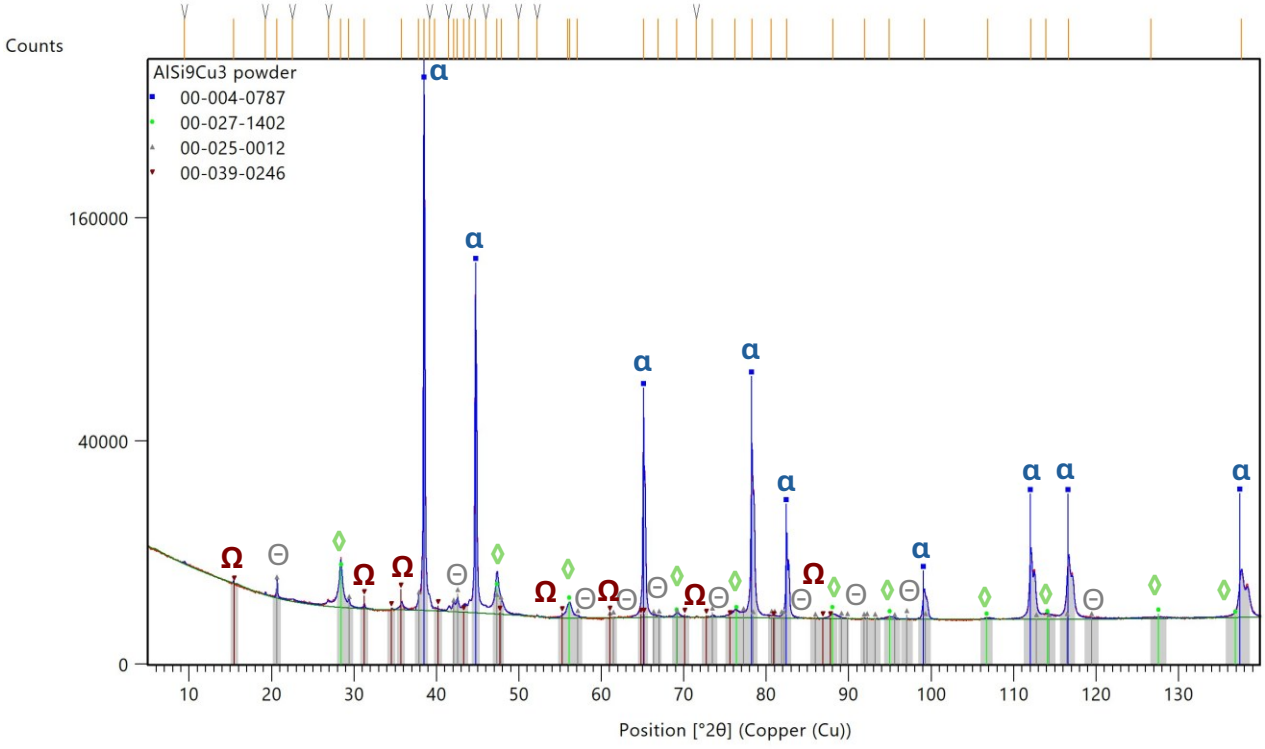
For both powders, the SI was close to 1.1: 1.067 for AlSi10Mg and 1.080 for AlSi9Cu3. These values indicate generally stable flow behavior under the repeated FT4 test cycles.

4.1.4 XRD

The XRD analyses produced a breakdown of the main crystalline phases found inside the two atomized alloys.



Graph 20 - AlSi10Mg Powder XRD spectrum plot: the red arrows indicate the unidentified peaks that were tentatively attributed to an oxide phase



Graph 21 - AlSi9Cu3 Powder XRD spectrum plot

Table 27 - List of encountered XRD peaks, powder samples

Peak Number	*Peak Code (ICDD)*	*Crystalline Phase*	*Reference Symbol*
1	00-004-0787	Aluminum, α-Al	α
2	00-027-1402	Si	◊
3	00-025-0012	θ-Al_2Cu	Θ
4	00-039-0246	$CuFeO_2$	Ω

From the XRD analysis of both powders, most of the crystalline structure appeared to be mainly comprised by the α-Aluminum and Silicon phases: this suggested that despite the presence of light amounts of ferrous contaminants (detected by the SEM-EDS analysis, see Section 4.1.2), the associated intermetallic phases fell below the detection threshold for the analyses.

The comparison with the database did not yield any satisfactory matches for the AlSi10Mg powder, with several secondary peaks remaining unidentified. Given that the sample was in powder form, it is reasonable to hypothesize that some of the unindexed peaks may be attributed to an oxide phase, particularly the first three weak peaks at low diffraction angles (see Graph 20). The remaining unindexed peaks are likely associated with an intermetallic phase.

Low amounts of θ-Al_2Cu were observed in the AlSi9Cu3 powder, with this species exhibiting the lowest recorded peaks of the analysis: this phase is commonly found inside untreated AlSi9Cu3 alloys and, as previously mentioned in Chapter 1.6.2.4, it can lead to an improvement of the mechanical behavior of the material (depending on the phase's morphology): this would seem to suggest that, if the phase were to be present after the L-PBF processing, novel thermal treatments could be employed in order to specifically improve both the mechanical and wear resistance of the AlSi9Cu3 parts.
In addition, the analysis indicated the presence of $CuFeO_2$: this suggests the possible formation of a Cu–Fe–O-containing phase during processing. In this context, the detection of $CuFeO_2$ may be associated with the interaction of residual Cu and Fe with oxygen present in the alloy during processing. The formation of this oxide could potentially be favored by the more complex chemical history and increased impurity content characteristic of secondary aluminum alloys. Nevertheless, $CuFeO_2$ is not generally reported as a primary constituent of secondary AlSi9Cu3 alloys, and its identification should therefore be considered with caution.

It was provisionally theorized that many secondary phases typical of aluminum's secondary processing, such as α-Fe and β-Fe intermetallic groups and the Mg_2Si phase in AlSi10Mg, were in such low amounts and sizes that their detection would require more sensitive techniques, like Scanning transmission electron microscopy (STEM) [92].

4.2 Printed components
4.2.1 Microstructural analysis
4.2.1.1 Optical Analysis, Porosity: AlSi10Mg

The following table presents the results for the first two samples of the AlSi10Mg alloy:

Table 28 - Porosity analysis results for the first L-PBF AlSi10Mg samples; the outlier value is highlighted in green

Plane	*Core Measurements*				*Edge Measurements*				*Mean Porosity Value*	*Standard Deviation (SD)*	
	(%)										
AlSi10Mg XY - 1	0.132	0.136	0.140	0.180	0.154	0.272	0.140	0.188	0.168	0.0470	
AlSi10Mg YZ - 1	0.155	0.150	0.105	0.153	0.171	0.220	0.147	0.150	0.157	0.0343	

The porosity measurements for XY plane yielded an average area fraction (porosity) of 0.168 ± 0.045 (SD).

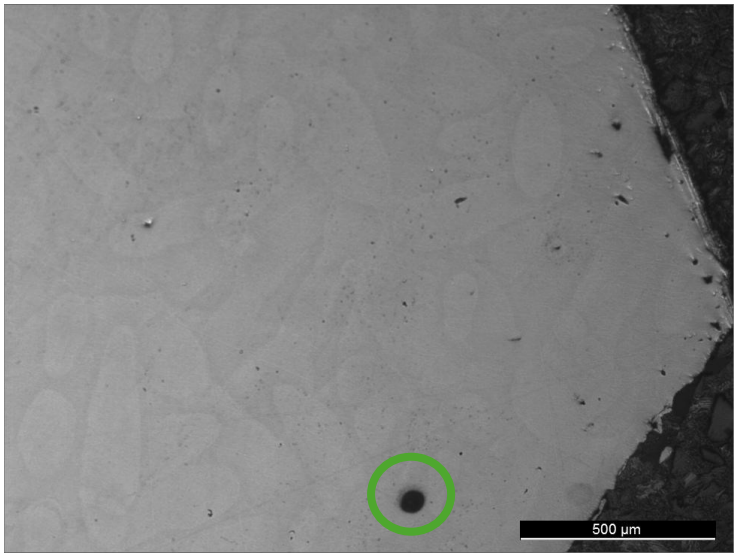


Figure 55 - AlSi10Mg XY – 1 sample, 50x; the gas porosity is highlighted by the green circle

The values obtained in the relative standard deviation for both planes are consistent with the spatial heterogeneity commonly reported for low-porosity L-PBF aluminum alloys; the following are typical factors behind this kind of result:

- In nearly-fully dense AlSi10Mg L-PBF prints optical/metallographic measurements still exhibit field-to-field variation because small pores are sparsely distributed. [94]

Both planes showed similar mean values porosity-wise, with the with the YZ plane presenting a negligibly higher surface area fill (99.84 versus 99.83%): this meant that the AlSi10Mg L-PBF print density was comparable with values commonly reported for industrial printing. [68,96]

It was observed that on both samples the shape of the melt-pools could be highlighted, thus displaying the typical general microstructure of an as-is L-PBF print: Figure 56 (a) showcases the elongated shape of the structures from the top-down view (XY plane), while Figure 56 (b)

illustrates the layering along the building direction (YZ plane). These melt pools can be easily distinguished by their lighter inner portion, coupled with a darker outline.

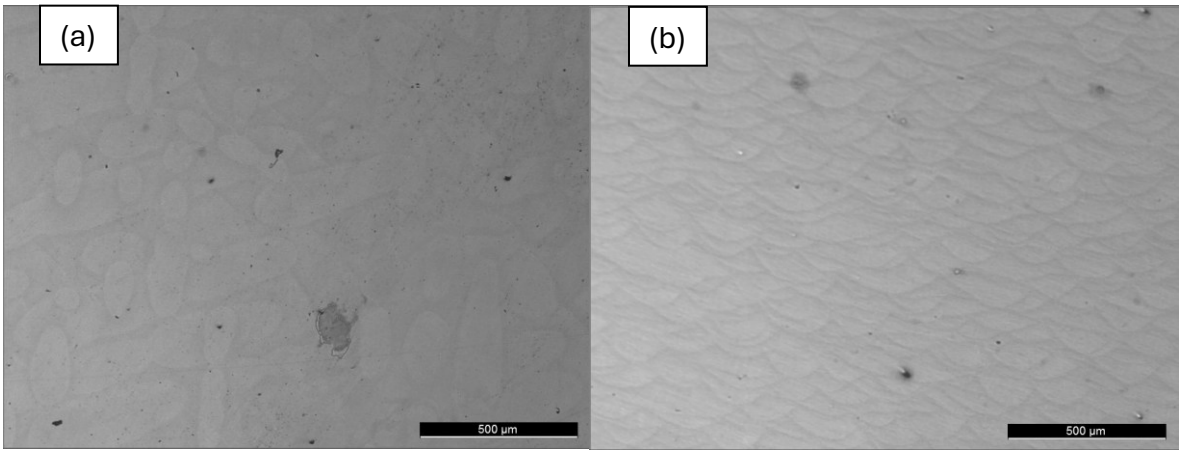


Figure 56 - Melt-pool appearance;
Image (a) displays the AlSi10Mg XY – 1 sample, where a Top-down view of the structure is seen
Image (b) displays the AlSi10Mg YZ – 1 sample, giving a clear view of the printing structure's layers

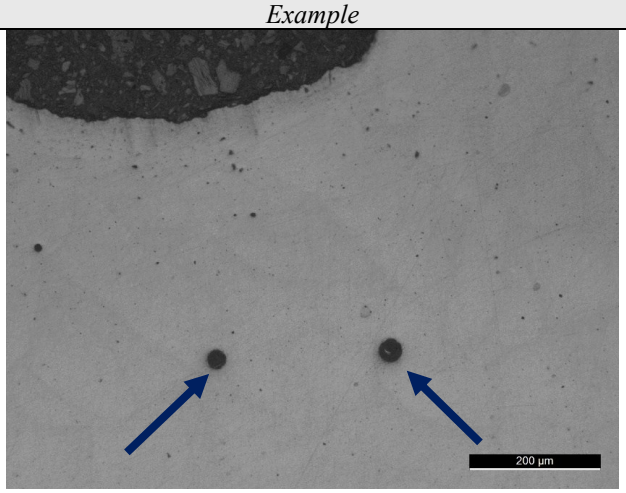
To obtain less uncertain results, a second batch of measurements was conducted for both directions of the AlSi10Mg alloy: the samples produced from the other halves of the printed cubes, which were subsequently employed in hardness testing.

Table 29 - Porosity analysis results for the second L-PBF AlSi10Mg samples

Plane	*Number of Core Measurements*	*Number of Edge Measurements*	*Mean core Porosity*	*Mean Edge Porosity*	Mean Porosity Value	Standard Deviation (SD)
			(surface area %)			
AlSi10Mg XY - 2	14	10	0.286	0.117	0.272	0.190
AlSi10Mg YZ - 2	10	10	0.117	0.126	0.123	0.0214

These samples showed comparable values to the previous ones considering the standard deviations.

Table 30 - Observed porosity types on the AlSi10Mg XY – 2's surface

Observed Defect Type	*Example*
Gas Porosities	 *Figure 57 - AlSi10Mg XY – 2 sample, highlighted by the blue arrows*

4.2.1.2 Optical Analysis, Porosity: AlSi9Cu3

The following table presents the results for the two samples of the AlSi9Cu3 alloy:

Table 31 - Porosity analysis results for the L-PBF AlSi9Cu3 samples

Plane	*Number of Core Measurements*	*Number of Edge Measurements*	*Mean core Porosity*	*Mean Edge Porosity*	Mean Porosity Value	Standard Deviation (SD)	
			(surface area %)				
AlSi9Cu 3 XY - 1	8	6	0.103	0.106	0.104	0.0229	
AlSi9Cu 3 YZ - 1	3	6	0.132	0.125	0.128	0.0222	

Both sets of measurements gave out values of mean porosity well inside the acceptable size range, with both samples presenting higher densities than their AlSi10Mg analogues. [68,96]

The obtained surfaces were shown to be more homogenous than the AlSi10Mg counterparts, exhibiting lower SD.
Less porosities were encountered, with gas porosities being the main type of observed defect (see Figure 58).

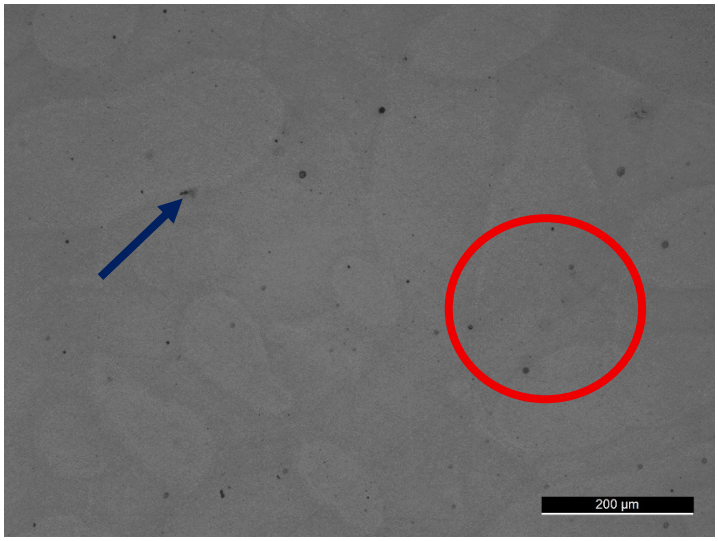
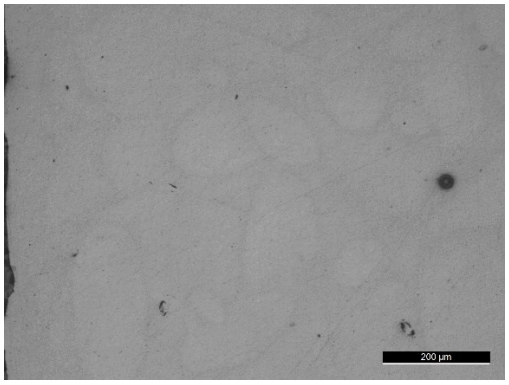
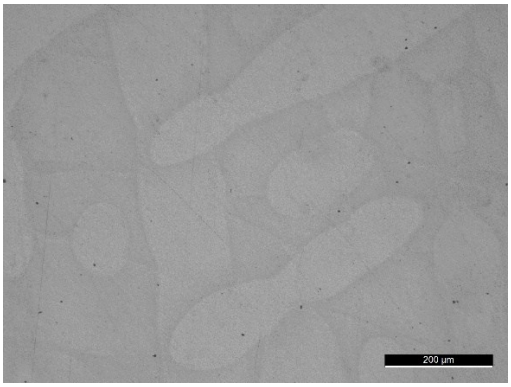
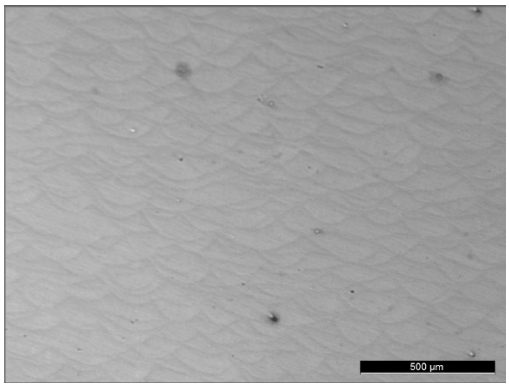
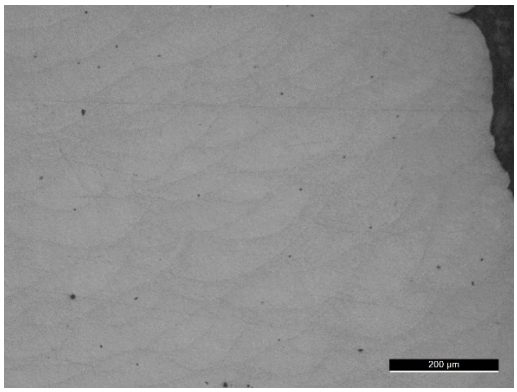


Figure 58 - AlSi9Cu3 XY – 1 sample; several gas porosities are highlighted by the red circle, while the blue arrow points at a lack-of-fusion defect

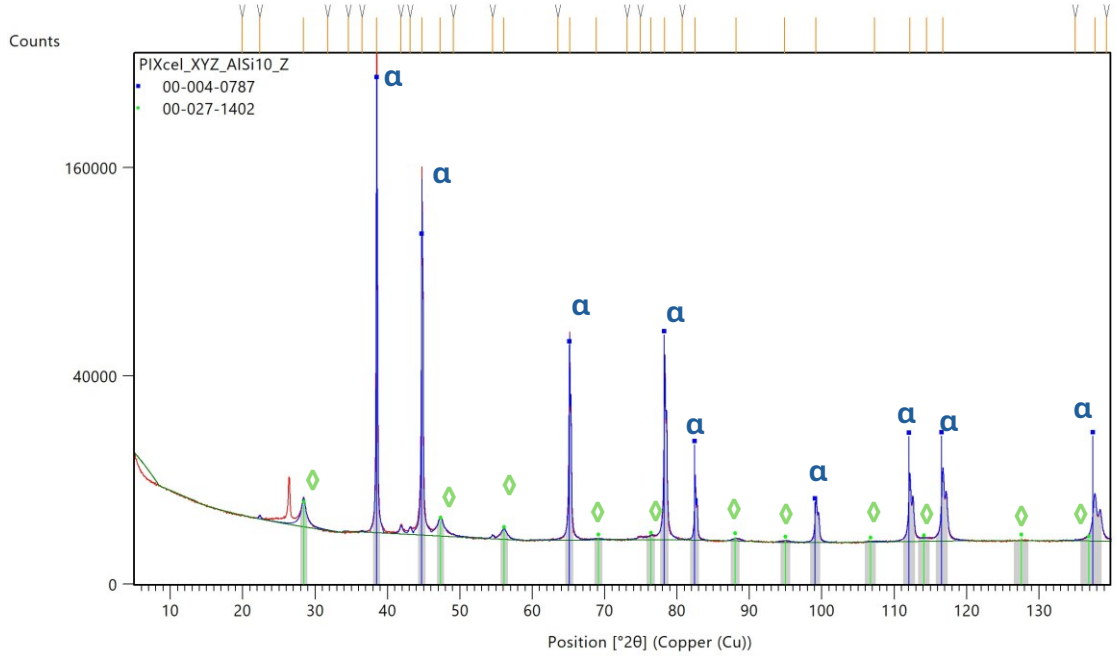
The melt-pools and layering structure are again clearly visible throughout the latter stages of the polishing process, having similar shapes to the ones encountered in the AlSi10Mg sample (see Table 32 for a direct comparison).

Table 32 - Melt-pool and layering comparison between the AlSi10Mg and AlSi9Cu3 alloys

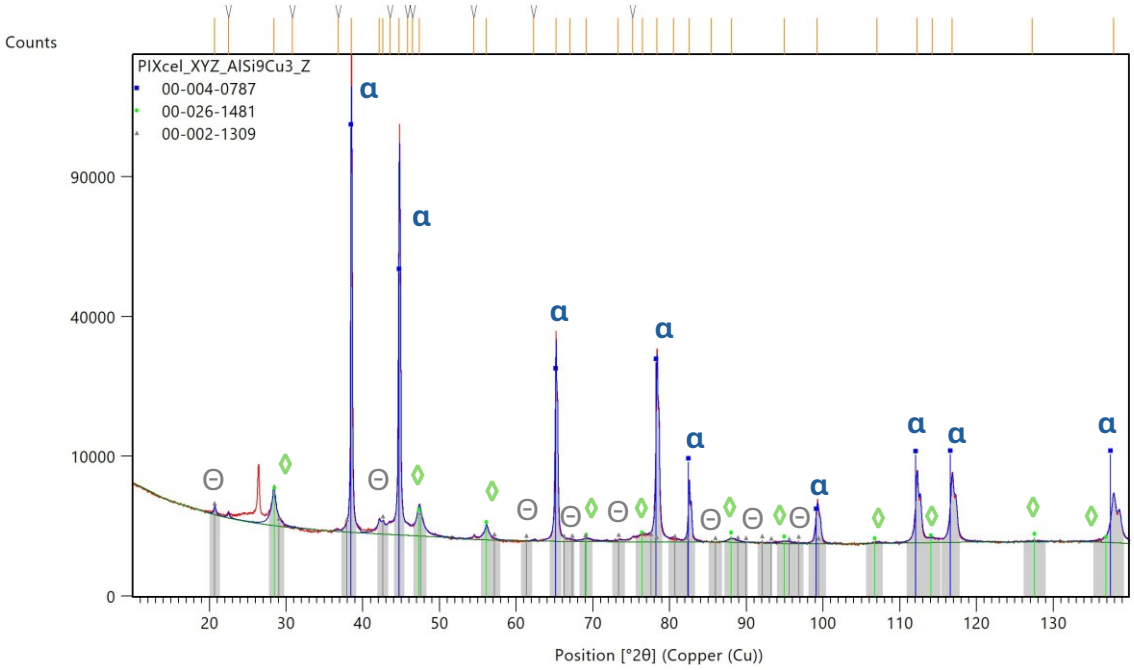
Reference Plane	*AlSi10Mg*	*AlSi9Cu3*
XY	 *AlSi10Mg XY – 2 sample*	 *AlSi9Cu3 XY – 1 sample*
YZ	 *AlSi10Mg YZ – 2 sample*	 *AlSi9Cu3 YZ – 1 sample*

4.2.2 XRD Analysis

A YZ sample of each alloy was analyzed, projecting a clearer picture on the phases contained inside each crystal lattice.
Graph 22 showcase the graph for the AlSi10Mg alloy:



Graph 22: AlSi10Mg YZ -1 XRD spectrum plot. The red peak is attributed to the mounting resin



Graph 23: AlSi9Cu3 YZ -2 XRD spectrum plot. The red peak is attributed to the mounting resin

Table 33 - List of encountered XRD peaks, L-PBF samples

Peak Number	*Peak code (ICDD)*	*Crystalline Phase*	*Reference Symbol*
1	00-004-0787	Aluminum, α-Al	α
2	00-025-0012	θ-Al_2Cu	Θ
3	00-027-1402	Si	◊

Both alloy samples were shown to be composed mainly by the Eutectic Aluminum-Silicon system (α-Al and Silicon phases), with lower quantities of the θ-Al_2Cu intermetallic phase detected in the AlSi9Cu3 sample.
To note, the Silicon phase appears much more infrequently as compared to the α-Al phase, having lower peaks that what was seen of the powders in Chapter 4.1.4; this can be explained in part by considering both the composition ranges of each alloy (both AlSi10Mg and AlSi9Cu3 are hypoeutectic species), and the thermal history of the samples: like previously mentioned in Chapter 1.7.1, it has been showed that at higher cooling rate ranges, such as between 10^6 and 10^8 °C/s, Si solubility in the Al matrix is extended up to 8 wt.% [99].
Considering that the cooling rates employed during the L-PBF printing process vary in the 10^5–10^6 K/s range this would lead us to suppose that a major fraction of the Silicon content inside both alloys was dissolved inside the α-Al aluminum phase. [100,101]
In both XRD patterns of both compositions, a peak is observed at approximately 26–27°. This peak, which is not included in the indexed peak list, originates from the resin used to embed the specimens.
Some unindexed peaks remain, which, as in the case of the AlSi10Mg powder, are tentatively attributed to the presence of an intermetallic phase
It was theorized that the scanning strategy managed to increase the solubilization of certain phases, such as θ-Al_2Cu, leading them to concentration below the detectable threshold of the scanning system.
As previously mentioned in Chapter 4.1.4, it was hypothesized that switching to a technique such as Scanning Transmission electron microscopy (STEM) in a further study would allow the detection of the lesser Intermetallic phases, such as the Chinese scripts.

The following Table notes the phase-makeup of several literature cast systems made from analogue alloys as the ones that were studied throughout this thesis project:

Table 34 -Main Phases of cast AlSi10Mg, ASi9Cu3

Alloy	*Phases*
Primary AlSi10Mg, as cast (gravity die casting)	• Primary α-Al • Needle Si particles • Al–Si eutectic • Mg_2Si [102,103,104,105]
Secondary AlSi10Mg (Fe >1 wt.%), as cast (high pressure die casting)	Same as above, with the addition of: • α-$Al_{15}(Fe,Mn)_3Si_2$ • β-Al_5FeSi • Fine intermetallic phases (IMP), like π-Al8FeMg3Si6 • $Al_{15}(FeMnCr)_3Si_2$ (sludge) [22, 106]
Secondary AlSi9Cu3 (Fe = 8 wt.%), as cast (sand casting)	• Primary α-Al • Needle Si particles • Al–Si eutectic • α-$Al_{15}Mn_3Si_2$ • β-Al_5FeSi

	• θ-Al_2Cu, $Al_5Mg_8Si_6Cu_2$ and Al-Al_2Cu-Si [107,108,109]

As it was previously mentioned in Chapter 1.6, Mn can lead to the formation of a "sludge" (comprised of larger intermetallics) if employed in tandem with an Iron content above 1 wt.% in a typical casting system: this phenomenon, known for its harmful effects on the mechanical behavior of casted secondary parts, was not observed in either of the L-PBF alloys.
This would suggest that less criticalities associated with Mn-doping would arise during an L-PBF print as compared to a traditional cast.
Several models have been produced, for casting systems, in order to deduce mathematically if an alloy is more or less susceptible towards Sludge formation: the process is known to occur at a critical concentration of Fe, Mn, and Cr; this can be estimated by use of a critical segregation factor (SF), which can be evaluated using the following formula: [110,111]

$$SF = Fe + 2Mn + 3Cr$$

In which each quantity is expressed using wt.%; each composition with an SF value reaching or exceeding 1.8 is known to lead to the formation of sludge.
Our L-PBF alloys were evaluated, using both the EDS measurements described in Chapter 4.2.3.1 (see Table 36 and 37), producing the following Table:

Table 35 - SF values for the L-PBF samples

Alloy	*SF value*
AlSI10Mg	1.64
AlSi9Cu3	1.51

Since both alloys had SF values beneath 1.8 the perceived link between the absence of the sludge and the L-PBF was considered nil.

To note, none of the typical intermetallics were observed during the course of this analysis, similarly as it was with the atomized powders (see Chapter 4.1.4): as is displayed in Table 33, no species such as α-$Al_{15}(Fe, Mn)_3Si_2$ and β-Al_5FeSi, typical for these systems, appeared consequently of this measurement. Since the subsequent EBSD testing managed to detect several α-Fe intermetallics (with α- $Al_{15}(Fe, Mn)_4Si_2$ as the general stoichiometry), it was assumed that these phases were to be present inside both alloys, but at such a concentration that they wouldn't be easily detectable through the use of a typical XRD analysis. As with the powders switching to a technique such as STEM could allow the precise detection of the presence of lesser Intermetallic phases, such as the Chinese scripts.

4.2.3 FE-SEM

4.2.3.1 EDS

For each alloy several surface sites were analyzed, in order then to evaluate a mean composition for both sample's surface; it was observed that by increasing the acquisition time of the measurement certain species, present in lower percentages and/or characterized by lower atomic weights, would be more easily detected.
As an example, in the AlSi10Mg sample analyses S and Ti peaks started appearing as soon as the acquisition time increased to be over 180 seconds long: these elements were determined to be in trace amounts, each amounting to a quantity below 0.1 wt.%.

The following tables present the extrapolated data for each sample, showcasing the observed compositional ranges and mean values for each detected element.

Table 36 - EDS composition results, AlSi10Mg YZ-1 prints

Statistic	*O*	*Mg*	*Al*	*Si*	*S*	*Ti*	*Mn*	*Fe*	*Cu*
	wt.%								
Max	1.53	0.36	88.06	9.74	0.08	0.06	0.50	0.77	0.18
Min	0.65	0.32	87.10	9.55	0.03	0.06	0.39	0.70	0.12
Mean	1.10	0.33	87.56	9.65	0.06	0.06	0.46	0.72	0.15
Standard Deviation (SD)	0.41	0.02	0.46	0.07	0.03	0.00	0.04	0.03	0.02

Table 37 -EDS composition results, AlSi9Cu3 YZ-2 print

Statistic	*O*	*Mg*	*Al*	*Si*	*Mn*	*Fe*	*Cu*	*Zn*
	wt.%							
Max	0.77	0.49	84.50	10.65	0.26	1.98	3.50	1.23
Min	0.56	0.34	82.52	9.18	0.00	0.84	2.99	0.97
Mean	0.67	0.40	83.59	9.65	0.18	1.15	3.32	1.09
Standard Deviation (SD)	0.06	0.04	0.65	0.46	0.10	0.33	0.14	0.08

Table 38 - EDS composition comparison; note that "Ex." means that the element was manually excluded from the analysis; the green backgrounds highlight apparent positive increments, while the red ones a loss in the elemental concentration

Alloy	*Mean Value*	*O*	*Mg*	*Al*	*Si*	*Mn*	*Fe*	*Cu*	*Zn*	*S*	*Ti*
		wt.%									
AlSi10Mg	*Powder*	*Ex.*	*0.35*	*88.4*	*10.3*	*0.517*	*0.683*	*0*	*0*	*0*	*0*
	L-PBF	*1.10*	*0.33*	*87.56*	*9.65*	*0.46*	*0.72*	*0.15*	*0*	*0.06*	*0.06*
	Difference	-	*-0.02*	*-0.84*	*-0.65*	*-0.057*	*-0.037*	*0.15*	-	*0.06*	*0.06*
AlSi9Cu3	*Powder*	*0.9*	*0.43*	*83.7*	*9.58*	*0.13*	*1.02*	*3.02*	*1.27*	*0*	*0*
	L-PBF	*0.67*	*0.40*	*83.59*	*9.65*	*0.18*	*1.15*	*3.32*	*1.09*	*0*	*0*
	Difference	*-0.23*	*-0.03*	*-0.11*	*0.07*	*0.05*	*0.13*	*0.3*	*-0.18*	-	-

Mn content varies substantially with acquisition time, reaching similar values as what was evaluated via EDS for both original powders (see Chapter 4.1.2).

O_2 and F_2 are both problematic species for this kind of analysis: they emit low-energy X-rays emissions, which can be easily absorbed by the detector window, sample surface contamination or air [92]. For this reason, light elements are typically evaluated using specific analyses, such as Electron Energy Loss Spectroscopy (EELS) and Wavelength-Dispersive X-

ray Spectroscopy (WDS). For the sake of this body of research, the focus was shifted more towards the rest of the chemical composition of each alloy.

The AlSi10Mg prints seemed to exhibit a small variation in their overall chemical composition, with a 0.84 wt.% drop in the Aluminum content and a slight decrease for several other elements (mainly Si): considering that these values are percentiles, it was assumed that the main bulk of these drops was to be pinned on the Oxygen content being measured only for the prints (while it was excluded in the powder's measurements) and the longer acquisition time employed in the analysis of the L-PBF prints, which for the detection of species such as Ti and S (thus reducing the apparent relative content of the phases that were already catalogued beforehand).

The AlSi9Cu3 saw a decrease in the overall Oxygen content after the printing: considering the inherent problems related to O detection for this kind of analysis, this variation was considered of no analytical significance. As for the other elements, the Cu wt.% seemed to decrease after the L-PBF processing, while the Fe fraction appeared instead to increase with a similar magnitude

In the case of the AlSi9Cu3 sample, the lighter-colored areas mentioned in Chapter 4.2.1.2 were analyzed to see if there was any significant compositional variation as opposed to the rest of the print's surface:

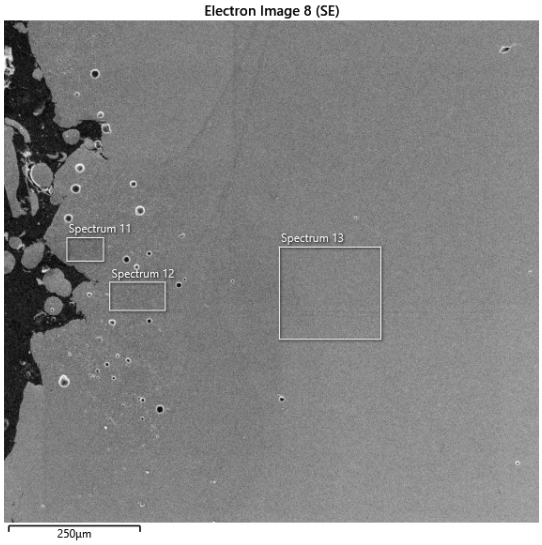


Figure 60 - EDS target sites, AlSi9Cu3 YZ-2 print; bottom portion

Table 39 - EDS composition results, AlSi9Cu3 YZ-2 print; bottom portion

Label	*O*	*Mg*	*Al*	*Si*	*Mn*	*Fe*	*Cu*	*Zn*
Spectrum 11	0.71	0.42	83.33	9.81	0.20	0.97	3.37	1.20
Spectrum 12	0.71	0.34	83.81	10.00	0.20	0.85	2.99	1.10
Spectrum 13	0.63	0.38	84.16	9.18	0.20	0.90	3.47	1.08

These areas seemed to possess a similar composition to the rest of the samples' surface, albeit with slightly lower amounts of Iron: this could mean that, during solidification, the growing α-Al dendrites reject Fe into the remaining liquid, causing the first lattice crystals to contain a lower ferrous content.

It was provisionally theorized that that both production steps, i.e. the atomization and printing of the powders, didn't affect in a substantial manner the chemical composition of the feedstock, outside of the removal of the superficial oxide-content as slag during the VIGA processing.

4.2.3.2 EBSD

The EBSD analysis produced colored and high-contrast maps highlighting both the size and orientation of the alloy's grains: several step sizes were employed to analyze the surface at different scales, permitting the study of both the smaller and largest lattice structures.
To better understand the impact of the building direction of the grain morphology of each alloy, only the YZ samples were studied using this method.

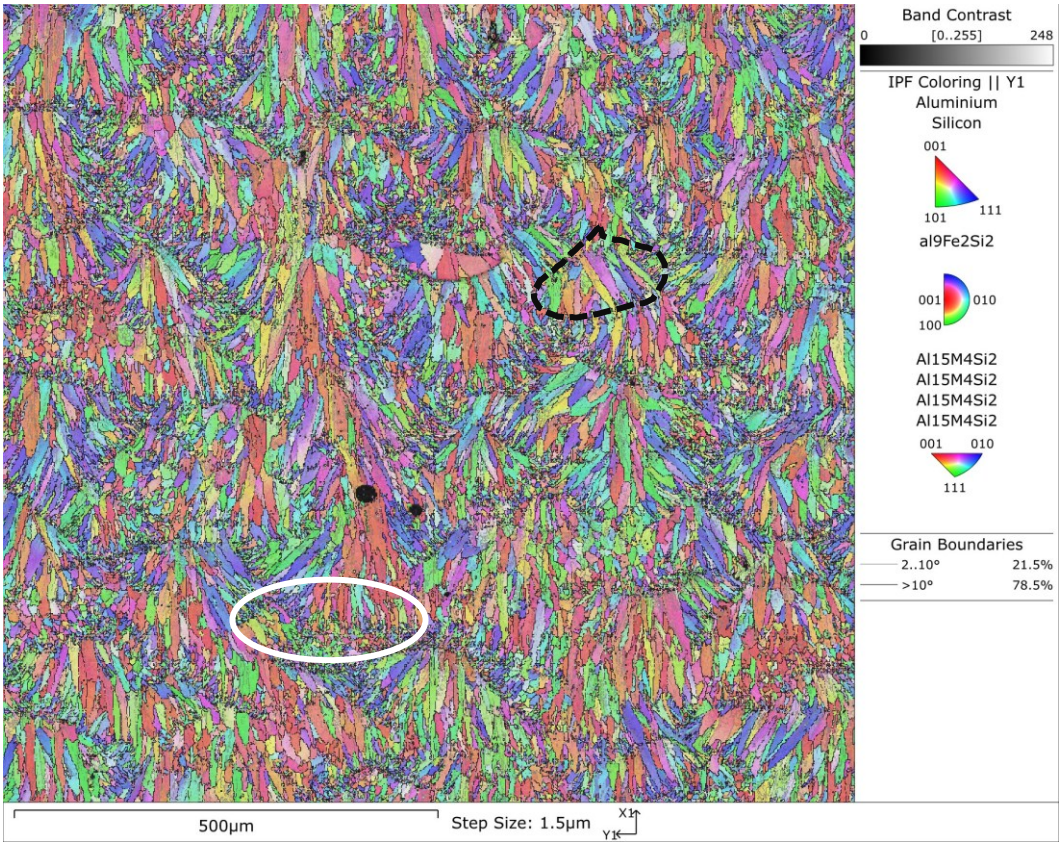


Figure 61 - AlSi10Mg YZ -1 EBDS grain orientation plot, site 6; the white circle highlights a cluster of equiaxial grains near a melt pool boundary, while the black dash line showcases the profile of a melt pool

Outside of the porosities present on the surface of each sample (represented by black pixels in the EBSD plots), the columnar eutectic structures appeared at differing sizes throughout the section paired with smaller-sized species: these grains appeared to be mainly oriented towards the building direction (BD) of the L-PBF print, highlighting the direct link between the forming process and the alloy's microstructure.
Coupled with these columnar species, smaller equiaxed grains can also be observed along the melt pool boundaries. Figure 64 highlights several of these different structures.
The grain size within the melting pools (MPs) was estimated through EBSD maps (see Figure 62).

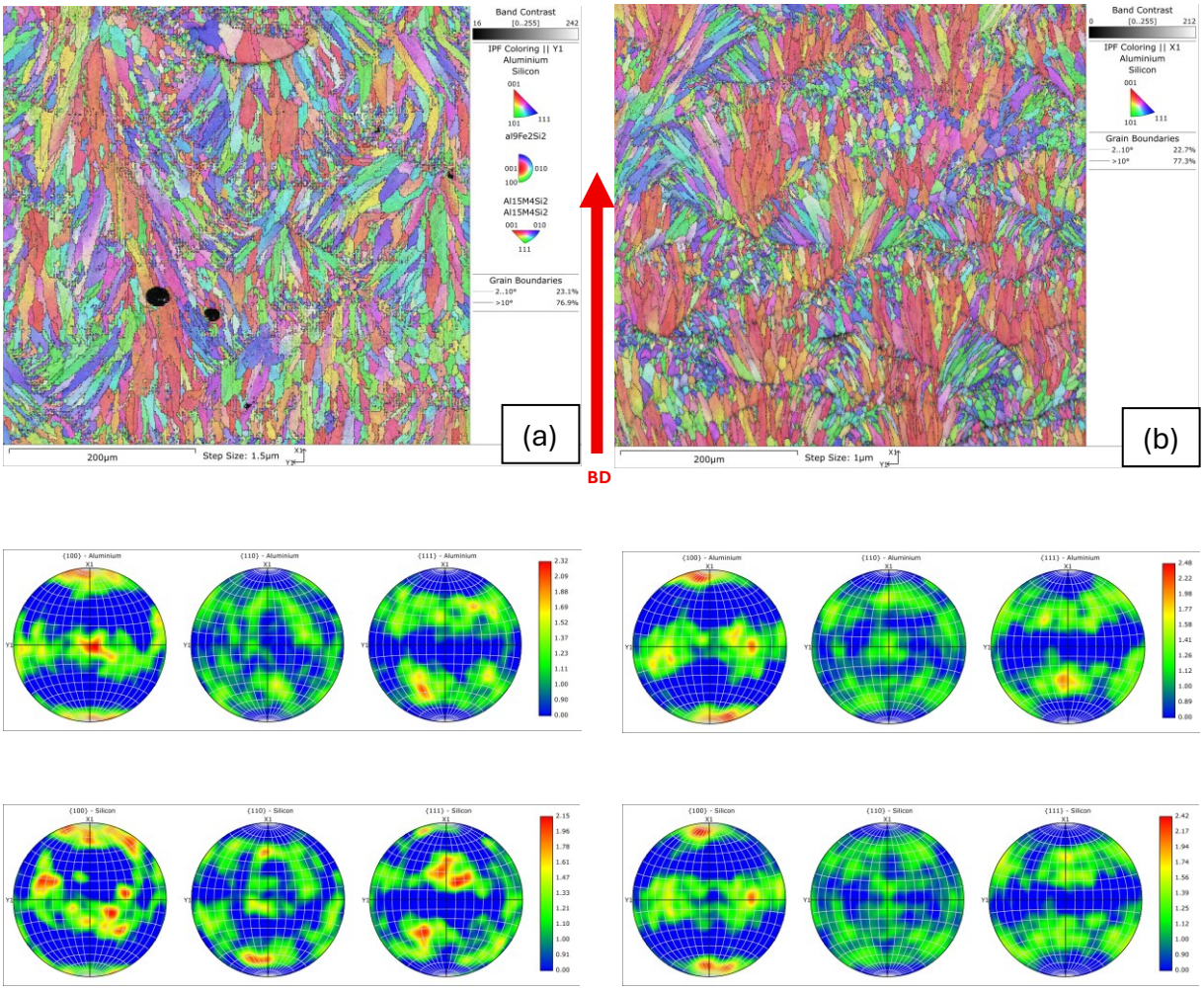


Figure 62 - EBSD maps and relative pole figures (Aluminum, Silicon) for both alloys: (a) AlSi10Mg YZ -1 Specimen Site 5 (Map Data 5-BC + IPF + GB_X1), (b) AlSi9Cu3 YZ -2 Site 10 (Map Data 1-BC + IPF + GB_Y1); the Building Direction (BD) is indicated by the red arrow.

The following step-size were employed:

- AlSi10Mg: for both sites 1.5 µm
- AlSi9Cu3:

Table 40 - AlSi9Cu3 EBSD step size list

Step Size (µm)	*Site 10*	*Site 11*	*Site 12*
	1	0.3	0.53

EBSD allowed also the detection of several intermetallic phases that hadn't been detected by either of the XRD analyses for the AlSi10Mg alloy:

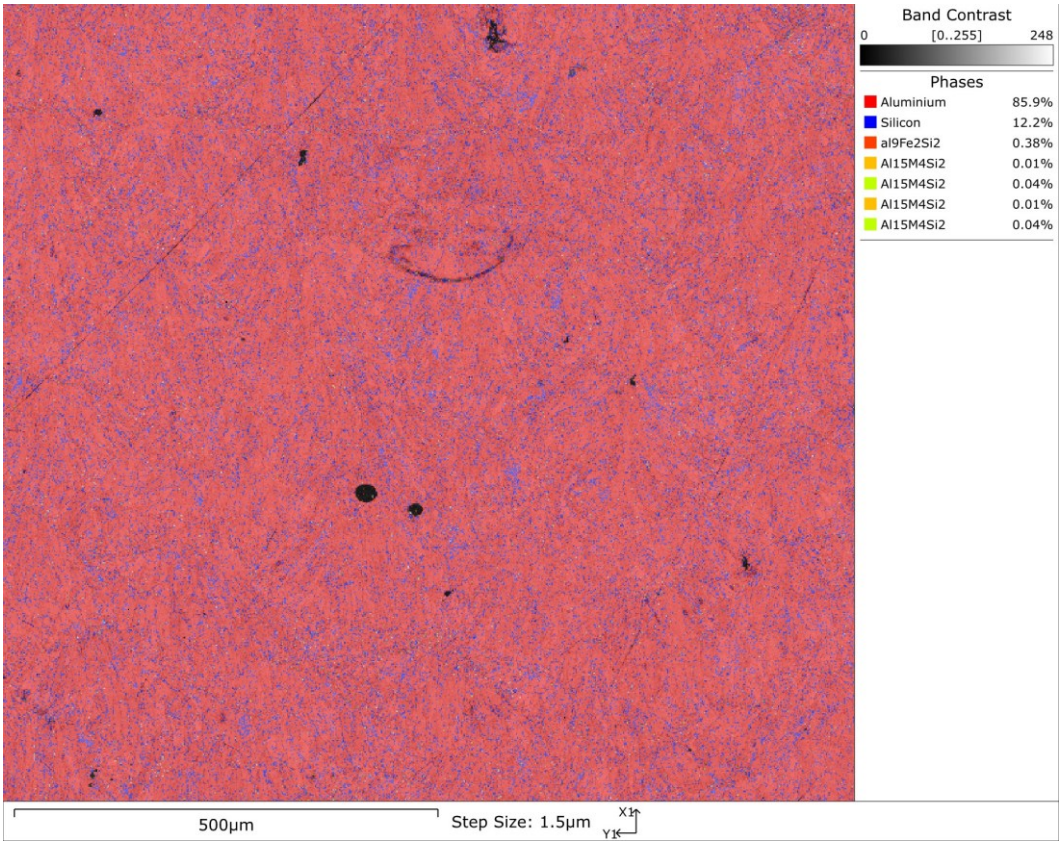


Figure 63 - EBSD phase map for the AlSi10Mg YZ -1, Site 6 (Map Data 6-BC + Ph).

Table 41 catalogues the detected phases:

Table 41 - AlSi10Mg YZ -1, phases detected through EBSD

	Aluminum, α-Al	*Silicon*	*β -$Al_9Fe_2Si_2$*	*α- $Al_{15}(Fe,Mn)_4Si_2$*
vol%	85.9	12.2	0.38	Four stoichiometries appear, 0.1 in total

Once again, it has been shown that the bulk of each alloy is comprised mainly by the α-Al and Si phases, with low amounts of secondary intermetallics phases dispersed near the contours of the melt pools: in the AlSi10Mg case, it was possible to distinguish several different stoichiometries of the α- $Al_{15}(Fe,Mn)_4Si_2$ Chinese Scripts dispersed throughout the section of a polished sample; higher amounts of the embrittling β-$Al_9Fe_2Si_2$ were also detected, demonstrating the impact of the recycling process on the AlSi10Mg sample's microstructure. In both cases, the morphology of each phase was difficult to evaluate, considering the relatively smaller size of each phase: it was suggested that a further study using FEM-SEM would allow a better understanding of the species' shape.
Meanwhile, the AlSi9Cu3 YZ -2 sample showed no noticeable traces of the intermetallic species, despite it containing higher recorded amounts of Fe, suggesting a vol% content below the EBSD's detector's minimum measurement threshold.
The grain boundary angles of the samples were also extrapolated from the maps, producing the following breakdown:

Table 42 - EBSD, grain boundaries angles

Sample	*Grain Boundaries Angles (%)*	
	2 – 10°	*>10°*
AlSi10Mg YZ -1 (site 5)	23.1	76.9
AlSi9Cu3 YZ -2 (site 10)	22.7	77.3

The two alloys exhibited similar values percentagewise, with both systems being mainly comprised of high-angle grain boundaries: this is typical for a polycrystalline fine-grained structure, such as one produced by L-PBF means, with L-PBF AlSI10Mg being typically reported as containing between 75 and 90% of HABG. [112,113]
In turn, this typically leads to several consequences, such as: [114]

- Different corrosion resistance
- Improved yield strength
- Increased surface hardness
- Less workability
- Different Creep resistance

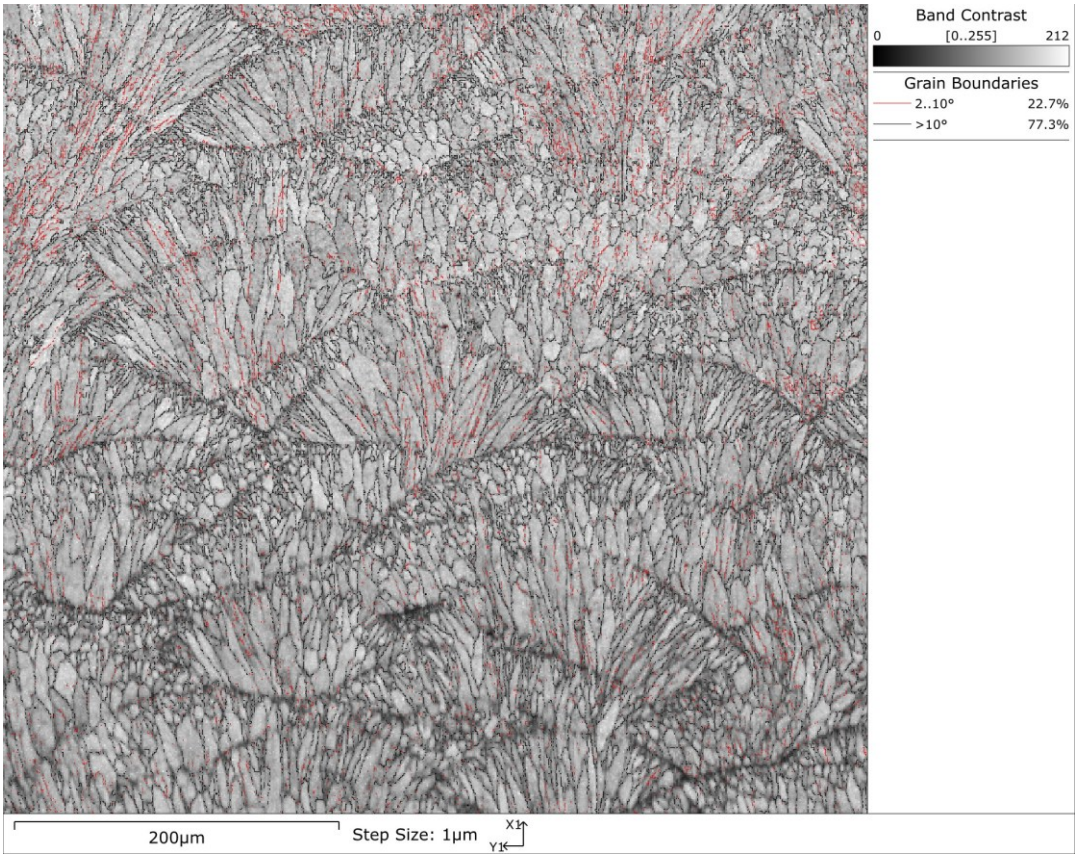


Figure 64 - EBSD Grain Boundary map for the AlSi9Cu3 Specimen 1 Site 10 (Map Data 6-BC + GB).

To modify this aspect of the prints, heat treatments are commonly employed: typical procedures aim at reducing the amount of HABG present in the lattice structure, thus improving the workability of the material.

Table 43 lists for each measurement the average Maximum Feret diameter (MFD): considering the raw analysis data, it was possible to clearly distinguish several different types of grains in different areas of the MPs. To note, the AlSI10Mg sample contained considerably fewer Silicon particles than its AlSi9Cu3 counterpart, despite both being hypoeutectic in

nature: this was already highlighted by the XRD analysis (see Graph 22 and 23 in Chapter 4.2.2)

Table 43 - MFD values observed in the AlSi10Mg YZ -1 and AlSi9Cu3 YZ- 2 samples

Sample	*Phase*	*Number of particles*	*Main MFD Ranges*	*Mean MFD*	*Maximum MFD*	*Minimum MFD*
			(µm)			
AlSi10Mg YZ -1 (site 6, 1436 particles)	Aluminum	1430	• 6.7–25 (1120 particles) • 25–133 (310 particles)	20.7	132.9	6.71
	Silicon	6	No discernible ranges	12.6	16.77	8.08
AlSi9Cu3 YZ- 2 (site 10, 1470 particles)	Aluminum	1260	• 4.4 – 10 (690 particles) • 10 – 30 (480 particles) • 30 – 110 (90 particles)	13.42	109.27	4.47
	Silicon	210	• 5.0 – 7.5 (140 particles) • 7.5 – 12.5 (70 particles)	7.42	12.53	5

Indeed, in each alloys the MP borders were characterized by clusters of smaller and equiaxed grains, exhibiting lower MFDs: these particles comprised the numerical majority of both system's grain count.
This clustering was theorized to be caused by the faster heat conduction in the liquid–solid interface during the course of the melting and solidification of the powder. At the same time, elongated grains were observed in the MP center, showcasing wider Feret ranges.

This has been reported in literature to be caused by the slower heat dissipation shown in this area, which lets the grains grow larger while following the thermal gradient. [115]
Several minor phases were observed by this means, showing a greater number of species than what was observed previously by EDS.

4.2.4 Mechanical analysis: microhardness

In the following table the HV values for the AlSi10Mg printed samples are showcased:

Table 44 - Vickers microhardness results for the AlSi10Mg printed samples

Sample	*Mean d (µm)*	*Mean HV*	*Standard Deviation*	
AlSi10Mg XY- 2	55.535	120	4	
AlSi10Mg YZ -2	57.949	111	5	

While Table 45 highlights the same values for the AlSi9Cu3 printed samples:

Table 45 - Vickers microhardness results for the AlSi9Cu3 printed samples

Sample	*Mean d (µm)*	*Mean HV*	*Standard Deviation*	
AlSi9Cu3 XY - 1	53.009	133	12	
AlSi9Cu3 YZ - 1	53.497	130	10	

The apparent increase in both Relative and Standard deviations between the two alloy types can be attributed to the user's inexperience: due to the instruments' measurements relying on the user's ability to line up a measuring gauge with the indent's profile, the first alloy set to be analyzed (in this case, the AlSi9Cu3 ones) yielded results more influenced by the operator's initial inexperience.
Despite so, since the relative standard deviation fell below the 10% mark, these initial analyses were still considered scientifically relevant for the analysis' sake.

The AlSi10Mg alloy showcased a small variation between the mean hardness values of the XY-2 and YZ-2 samples, reaching around 10 HV.
Several other factors influence the property, including: [118]

- Cooling rate
- Grain size/dislocation density
- Cellular/dendritic microstructure, including the grain orientation
- Precipitates
- Alloy chemistry
- Any additional post-processing (i.e. thermal treating).

Due to the variation in density between the samples AlSi10Mg YZ-2 and XY-2 amounting to 0.15 %, the porosity variation between the two was considered unimpactful in regards of the HV values.
This change in behavior was instead mainly attributed to the anisotropic lattice structure of the L-PBF; as hardness is a measurement of localized plastic deformation, the indentation may intersect melt pools differently:

- XY plane**:** predominantly across melt pool boundaries.
- YZ plane**:** across stacked melt pools.

This effectively changes the fraction of:

- fine cellular regions,
- heat-affected zones,
- remelted material,

beneath the indenter, meaning that the local resistance of the material may change.

Another facet that ought to be considered is the impact of the laser patterning along the building direction: the Z axis typically experiences repeated re-heating (as opposed to the XY planes), which in turn can lead to a partial coarsening of the Si network, a reduction dislocation density and slight softening of the structure [119]. This could also factor in the reduction of HV for the AlSi10Mg YZ -2 sample.

As for the AlSi9Cu3 prints, the alloy behaved in a more isotropic manner: the registered variation in the mean HV values for the two samples only amounted to around 3 HV.

Table 46 showcases several typical HV values for both alloy types, considering several production processes:

Table 46 - Typical HV values for both studied alloys

Alloy Type	*As Cast, Primary*	*L-PBF, Primary, as Built*	*Heat-treated L-PBF*
	HV		
AlSi10Mg	87 - 97	120 -140 [122,123]	• Solutionized: 90 -120 • Optimized Aging: 120 – 140 [124]
AlSi9Cu3	92 – 102 [121]	135 – 155 [120]	Aged, Cu precipitation: 150 -190 [126,127,128]

In both cases, the alloys microhardness values appeared to be slightly lower than what was reported in literature: this would suggest that further modulation of the printing parameters could help in furthering enhancing the HV values, with additional heat treatments being a worthwhile step to be taken into account.
The use of thermal treatments is widely reported on, with T4 and T6 being both typical procedures adopted for the AlSi9Cu3 alloy types: the combination of solution heat treatment, quenching and aging (natural in case of T4, artificial for T6; see Figure 2 in Chapter 1.3.1) has been shown to help in modifying the Fe-rich and Cu-rich intermetallic phases, with higher hardness achievable by means of the artificial aging (T6); this has been a subject of many studies, mainly focusing on how the as-built LPBF microstructure, which by its nature is already exceptionally fine and highly strengthened, requires highly specific parameters in order to achieve even higher mechanical performances. [128,129]
To note, the modulation of the typical ASTM heat treatments for cast parts is completely different from the analogues employed in the processing of L-PBF components, due to the wholly different microstructures.

As for the AlSi10Mg alloy, there is a strong body of literature showing that conventional post-process heat treatments generally do not increase the hardness (HV) of LPBF AlSi10Mg beyond the as-built condition [131,132,133], with the initial hardness of the LPBF as-built part only being restorable at best , but not exceeded, by T6-like treatments [134]: this suggests that the highest HV values obtainable for this alloy are mainly limited by the parameters chosen during the printing process itself, while several options can be pursued whenever enhancing workability is the goal.

5 CONCLUSIONS

Over the course of this thesis project the processability of secondary AlSi10Mg and AlSi9Cu3 powders was evaluated, by analyzing both the output of a gas atomizer VIGA and the quality of a set of L-PBF cubic samples made from each of the atomized alloys.

The atomization process for both alloys performed correctly, allowing the production of a seemingly high yield of fine, spherical powders with very few remnant gas porosities. Both alloys' compositions were analyzed, with each sample falling inside its typical nominal compositional ranges, although with varying low amounts of additional Fe and Mn contaminants.
Each alloy, once saved, showed a decent grade of flowability.
The printing process was subsequently evaluated, employing typical scanning strategies and L-PBF typically employed with primary powders: both sets of prints were shown to be dense enough to fall in the upper echelon of most industrial standards.
Composition wise, it was shown that both the atomization and printing process had a negligible effect on the chemical makeup of the two metal alloys, with the changes in elemental content mainly attributed to differences in the scanning parameters employed in the EDS analyses.
It was also observed how the L-PBF influenced the microstructure of both alloys.

As a mechanical property, Vickers Microhardness was measured for both printed sample types: this set of measurements gave a clearer look at the link between the and the mechanical behavior of both materials, showing how in both cases their performance slightly underperformed the standards commonly found in literature. It was further discussed how to modulate this property, by either working on the L-PBF themselves or by acting by means of subsequent thermal treating.

In the end, it was demonstrated that the combination between a tightly controlled atomization process and a specifically modeled L-PBF could aid in recovering production scrap and end-of-life components: as for the quality of the products, both alloy types seemed to contain low quantities of extremely fine intermetallics. It was concluded that further mechanical evaluation and phase identification would allow for a more complete prospective on the use of these secondary materials.

6 FUTURE DEVELOPMENTS

Throughout the process of this study, several possible future avenues of research were discovered, including:

- **Produce a comprehensive cost-analysis report for the whole production**: a study focusing on the costs related to material sourcing, energy expenditure and manufacturing could help in better evaluating the economic feasibility of this line of processing.
- **Additional testing**: several parameters have yet to be studied in dept for both of these completely recycled alloys; additional mechanical testing (like tensile tests and fatigue tests) and high magnification electron microscope analysis (such as TEM)) could help in further discovering any additional peculiarities and challenges related to these materials.
- **Improve the L-PBF parameters**: A study focused on the printing parameters themselves could lead to higher obtainable performances with this alloy, considering the impact associated with the contaminant's traces present in the feedstock.
- **Test different tailored-made heat treatment**: in combination with different recycled content-combinations, studying novel heat treatments to pair with the production processes could help in furthering expanding the field of use for these alloys; since literature on the topic for primary AlSi10Mg and AlSi9Cu3 is plentiful, a preceding literature review could help in directing the focus in this additional study towards the least-documented treatment alternatives.

7 REFERENCES

1.Norsk Hydro. (2021). *Global end use of aluminum products in 2020, by sector*. Statista, Online: https://www.statista.com/statistics/280983/share-of-aluminum-consumption-by-sector/ (Accessed: March 21, 2026)

2.Tisza M., Czinege I. (2018). *Comparative study of the application of steels and aluminium in lightweight production of automotive parts*. International Journal of Lightweight Materials and Manufacture, Volume 1, Issue 4, Pages 229-238, Pages 229-238, https://doi.org/10.1016/j.ijlmm.2018.09.001.

3. Polmear I.J., StJohn D., Nie J., Quien M. (2017). *Light Alloys: Metallurgy of the Light Metals.* 5th Ed, Butterworth-Heinemann, Pages 265-286, https://doi.org/10.1016/B978-0-08-099431-4.00005-1.

4.Davis J.R. (1998). *Metals Handbook Desk Edition*. ASM International, DOI: 10.31399/asm.hb.mhde2.9781627081993

5.Ferraro S. (2025). *Secondary aluminium alloys and innovative metallurgical processes for sustainable automotive applications*. PHD Thesis, Università degli Studi di Torino

6.Davis J.R. (1993) *Aluminum and Aluminum Alloys*, ASM International, 3th ed. https://doi.org/10.31399/asm.ash.aaa.9781627085120

7.Hind A., Bhargava S., Grocott S. (1998). *The surface chemistry of Bayer process solids: a review*. Colloids and Surfaces A: Physicochemical and Engineering Aspects, Vol 146, Pages 359–374, https://doi.org/10.1016/S0927-7757(98)00798-5

8.Boe R. (2012). *Luftbilder von der Nordseeküste 2012-05. - Rotschlamm-Becken der ehem. VAW Stade, Lage 10 km NW Stade*. Online, https://commons.wikimedia.org/wiki/File:Luftaufnahmen_Nordseekueste_2012-05-by-RaBoe-478_retusche_b.jpg, https://creativecommons.org/licenses/by-sa/3.0/de/legalcode (Accessed: December 13, 2026)

9.Al-Ghandoor A., Phelan P., et al. (2018). *Energy and Exergy Analyses of Different Aluminum Reduction Technologies*. Sustainability, Vol 10. DOI: 10.3390/su10041216.

10.International Aluminium Institute (2025). *Global Aluminium Cycle 2024*. Online, https://alucycle.international-aluminium.org/public-access/. (Accessed: April 13, 2026)

11.Raabe D., Tasan C.C., Olivetti E.A., (2019). *Strategies for improving the sustainability of structural metals*. Nature. 575 64–74. DOI:10.1038/s41586-019-1702-5.

12.Daehn K., Basuhi R., Gregory J., Berlinger M., et al. (2022) *Innovations to decarbonize materials industries*. Nature Review Materials, Vol 7, Pag 275–294. DOI: 10.1038/s41578-021- 00376-y

13.Brough D., Jouhara H. (2020). *The aluminium industry: A review on state-of-the-art technologies, environmental impacts and possibilities for waste heat recovery*. International Journal of Thermofluids, Volumes 1–2. DOI: 10.1016/j.ijft.2019.100007

14.Gutowski T. G., Sahni S., Allwood J., et al. (2013) *The energy required to produce materials: constraints on energy-intensity improvements, parameters of demand*. Phil. Trans. R. Soc. A ; Vol 371 (1986) DOI: 20120003.

15.Raabe D., D. Ponge, P.J. Uggowitzer, M. Roscher, et al. (2022). *Progress in Materials Science Making sustainable aluminum by recycling scrap : The science of "dirty " alloys*. Material Science, Vol 128. DOI:10.1016/j.pmatsci.2022.100947

16.The Aluminum Association. (2025) "Recycling" Online https://www.aluminum.org/Recycling (Accessed: April 13, 2026)

17.Metal Packaging Europe & European Aluminium. (2025). *Record Number of Used Aluminium Beverage Cans Recycled as Industry Drives Toward 100% Circularity by 2050.* Press Release, Online https://european-aluminium.eu/wp-

content/uploads/2025/02/EA-MPE-BevCan-2022-Recycling-Results-Press-Release-10-February-2025.pdf (Accessed: May 13, 2026)
18. Haraldsson J, Johansson M.T., (2018). *Review of measures for improved energy efficiency in production-related processes in the aluminium industry – From electrolysis to recycling*. Renewable and Sustainable Energy Reviews, Vol 93, Pag 525–548. DOI:10.1016/j.rser.2018.05.043.
19. Da Silva M., Pujante J. (2022) *Report with the results of the laboratory trials with partially recycled alloys*. Report, European Union's Horizon 2020 research and innovation programme under grant agreement No 101003785, 2022;
20. Bamberg P., Schiebahn A., Marzzona A., et al. (2024). *Optimization of weldability and joint strength of Al-Mg-Si with additional Al-Si cladding based on a design of experiments investigation* Journal of Advanced Joining Processes, Vol 9 https://doi.org/10.1016/j.jajp.2024.100206
21. B. Suárez-Peña, J. Asensio-Lozano, G. F. Vander-Voort (2010). *Colour metallography in commercial Al-Si alloys. Optimization of the microstructural characterization techniques in light optical microscopy*. Revista de Metalurgia, Vol. 46 No. 5 , https://doi.org/10.3989/revmetalm.1013
22. Bösch D., Pogatscher S., Hummel M. *et al.* (2015). *Secondary Al-Si-Mg High-pressure Die Casting Alloys with Enhanced Ductility*. Metallurgical and Materials Transactions A, Vol 46, 1035–1045 https://doi.org/10.1007/s11661-014-2700-8
23. European Committee for Standardization (CEN) (2014) *Aluminium and aluminium alloys — Classification of Defects and Imperfections in High Pressure, Low Pressure and Gravity Die Cast Products,* Standard CEN/TR 16749:2014
24. Fracchia E. (2024) *New Processes in Aluminium Alloys* PHD Thesis, Università degli Studi di Torino
25. Que Z., Wang Y., Mendis C., et al. (2022). *Understanding Fe-Containing Intermetallic Compounds in Al Alloys: An Overview of Recent Advances from the LiME Research Hub*. Metals, Vol 12., Pag 1677. DOI:10.3390/met12101677.
26. Mahta M., Emamy M., Cao X. & Campbell J. (2008). *Overview of B-Al5FeSi phase in Al-Si alloys*. Materials Science Research Trends, Pag 251-272
27. J. Kasińska D., Bolibruchová, Matejka M. (2020). *The influence of remelting on the properties of AlSi9Cu3 alloy with higher iron content*. Materials, Vol 13 https://doi.org/10.3390/ma13030575.
28. Becker H., Fankhänel B., Voigt C., Charitos A., et al. (2022). *Interaction of Fe-Containing, Secondary Al–Si Alloy with Oxide and Carbon-Containing Ceramics for Fe Removal.* Adv. Eng. Mater., Vol 24. https://doi.org/10.1002/adem.202100595
29. Taylor J.A.(2012) *Iron-Containing Intermetallic Phases in Al-Si Based Casting Alloys*. Procedia Mater. Sci. 1 19–33. doi:10.1016/j.mspro.2012.06.004
30. Qian D., Lan K., Yang Y. (2024) *Microstructure evolution of a novel low-silicon cast aluminum alloy modified with Mn and Cr during solution treatment*. Materials Characterization, Vol 217. https://doi.org/10.1016/j.matchar.2024.114319.
31. Mueller B.A., Perepezko J.H., (1988). *Microstructure development in undercooled Al Al_2Cu alloys*. Materials Science and Engineering, Vol 98, Pag 153-156, https://doi.org/10.1016/0025-5416(88)90145-0.
32. Hooper P. (2018). *Melt pool temperature and cooling rates in laser powder bed fusion*. in Additive Manufacturing, Vol 22, Pages 548-559. ISSN 2214-8604
33. Campbell J. (2015). *Complete Casting Handbook (Second Edition*). Chapter 5, Pages 163-222, Butterworth-Heinemann. ISBN 9780444635099

34. Anon (2008). *Thermodynamic Properties of Aluminum-Base and Copper-Base Alloys: Activities and Thermal Properties*. ASM Handbook, Vol. 15: Casting. Vol 15. ASM International. ISBN: 9780871707116
35. Li L. et al. (2020). *Effect of Cooling Rates on the Microstructure and Mechanical Property of La Modified Al7SiMg Alloys Processed by Gravity Die Casting and Semi-Solid Die Casting*. Metals (Basel), Vol.10 (4). ISSN: 2075-4701
36. Alghamdi F. et al. (2020). *Post heat treatment of additive manufactured AlSi10Mg: On silicon morphology, texture and small-scale properties*. Materials science & engineering. Structural materials: properties, microstructure and processing, Vol 783. ISSN: 0921-5093
37. Peng Q. et al. (2023). *Rapid solidification of Al-Si alloys using differential fast scanning calorimetry*. Journal of alloys and compounds, Vol. 965. ISSN: 0925-8388
38. Yang B. et al. (2021). *Nucleation behaviour and microstructure of single Al-Si12 powder particles rapidly solidified in a fast scanning calorimeter*. Journal of materials science, Vol. 56(22). ISSN: 0022-2461.
39. Peng Q. et al. (2021). *Nucleation Behavior of a Single Al-20Si Particle Rapidly Solidified in a Fast Scanning Calorimeter*. Materials, Vol.14 (11) [Online] ISSN: 1996-1944
40. Kessler O. et al. (2022) *Correlation between Differential Fast Scanning Calorimetry and Additive Manufacturing Results of Aluminium Alloys*. Materials, Vol 15 (20). ISSN: 1996-1944.
41. Takata N. et al. (2022). *Fast scanning calorimetry study of Al alloy powder for understanding microstructural development in laser powder bed fusion*. Materials & design, Vol 219. ISSN: 0264-1275
42. Shen X. et al. (2022). *Effect of Cooling Rate on the Microstructure Evolution and Mechanical Properties of Iron-Rich Al–Si Alloy*. Materials, Vol 15 (2). ISSN: 1996-1944
43. Mbuya T. O. et al. (2003*). Influence of iron on castability and properties of aluminium silicon alloys: literature review*. International journal of cast metals research, Vol.16 (5), pg. 451–465. ISSN: 1364-0461
44. Wang L. et al. (1999). American Foundry Society Trans., Vol 107, pg 231-238
45. Timpel M. et al. (2012) *The role of strontium in modifying aluminium–silicon alloys.* Acta Materialia, Vol. 60 (6), pg 3930 – 3928. ISSN: 1359-6454
46. Jenkinson D.C. (1975). *The modification of aluminium-silicon alloys with strontium.* Journal of Crystal Growth, Vol 28 (2), pg. 171-187. ISSN 0022-0248.
47. Kasprzak W. et al. (2009). *The Effect of the Melt Temperature and the Cooling Rate on the Microstructure of the Al-20% Si Alloy Used for Monolithic Engine Blocks*. International journal of metalcasting, Vol 3 (3), pg. 55–71. ISSN: 1939-5981
48. M. Žbontar et al. (2021) *The influence of cooling rate on microstructure and mechanical properties of alsi9cu3*, Metals (Basel), Vol. 11(2). ISSN: 2075-4701
49. Zhang X. et al. (2024*). Effect of cooling rates and heat treatment time on Si phase of AlSi10Mg alloy manufactured by selective laser melting: Microstructure evolution and strengthening mechanism*. Journal of alloys and compounds, Vol. 1007. ISSN: 0925-8388
50. Leis, A. et al. (2022). *Tuning the Hardness of Produced Parts by Adjusting the Cooling Rate during Laser-Based Powder Bed Fusion of AlSi10Mg by Adapting the Process Parameters*. Metals (Basel). Vol.12 ISSN: 2075-4701
51. Blue Powder Metallurgy (2024) *What is Atomization in Powder Metallurgy?* Online: https://powdermetallurgy.com/atomization-in-powder-metallurgy/ (Accessed: January 13, 2026)

52. Neikov, Oleg. (2009). *Chapter 5. Atomization and granulation*. Institute for Problems of Materials Science (IPMS), Pag 14, DOI: 10.1016/B978-1-85617-422-0.00005-7
53. US Patent 2,997,245, Aug 1961
54. Persson F., Hulme C., Jönsson P. (2022) *Particle morphology of water atomised iron-carbon powders.* Powder Technology, Vol 397, https://doi.org/10.1016/j.powtec.2021.11.037.
55. Zhou Z., Sun W., Lu W., Zhang S. and Wang, J. (2025). *Advancements in Understanding the Characteristics of Gas Atomized Powders: A Review*. Advanced Engineering Materials, Vol 27. https://doi.org/10.1002/adem.202500270
56. Boes J., Röttger A., Theisen W., Cui Cet al. (2020). *Gas atomization and laser additive manufacturing of nitrogen-alloyed martensitic stainless steel.* Additive Manufacturing, Vol 34, https://doi.org/10.1016/j.addma.2020.101379.
57. Özbilen S. (2013). *Satellite formation mechanism in gas atomised powders Powder Metallurgy*. Vol 42. DOI: 10.1179/pom.1999.42.1.70.
58. Rabin B., Smolik G., Korth G. (1990) *Characterization of entrapped gases in rapidly solidified powders.* Materials Science and Engineering, Vol 124 (1) https://doi.org/10.1016/0921-5093(90)90328-Z.
59. Wang P., Li X., Zhou X., Chen Z., et al. (2024) Trans. Nonferrous Met. Soc. China, Vol 34
60. Luo S., Wang H., Gao Z., et al. (2021). *Interaction between high-velocity gas and liquid in gas atomization revealed by a new coupled simulation model.* Materials and Design, Vol 212, DOI: 10.1016/j.matdes.2021.110264
61. Wei M., Chen S., Sun M., (2021). Powder Technology, Vol 367, 724.
62. Ji W., Zhou R., Viveganantha P., Mao See Wu, et al. (2023). *Recent progress in gradient-structured metals and alloys*. Progress in Materials Science, Vol 140, https://doi.org/10.1016/j.pmatsci.2023.101194.
63. Huang Y., Fleming T., Clark S., et al. (2022). *Keyhole fluctuation and pore formation mechanisms during laser powder bed fusion additive manufacturing*, Nature Communication, Vol 13. https://doi.org/10.1038/s41467-022-28694-x.
64. Kramer S., Wexel H., Purwitasari, A. *et al.* (2025) *Impact of different pore types on the tensile and fatigue properties of AlSi10Mg parts produced by laser powder bed fusion*. Progress in Additive Manufacturing Vol 10. https://doi.org/10.1007/s40964-025-01288-x
65. Guillen, D., Wahlquist, S., & Ali, A. (2024). *Critical Review of LPBF Metal Print Defects Detection: Roles of Selective Sensing Technology.* Applied Sciences, Vol 14(15). https://doi.org/10.3390/app14156718
66. Felix H. Kim Shawn P. Moylan (2018) *Literature Review of Metal Additive Manufacturing Defects*. NIST Advanced Manufacturing Series 100-16, https://doi.org/10.6028/NIST.AMS.100-16
67. Kaess, M., Werz, M., & Weihe, S. (2023). *Residual Stress Formation Mechanisms in Laser Powder Bed Fusion—A Numerical Evaluation*. Materials, Vol 16(6). https://doi.org/10.3390/ma16062321
68. Piedra, S., Gómez-Ortega, A., Félix-Martínez, C. et al. (2026) *Experimental and numerical study of single-track formation in the laser powder bed fusion process of AlSi10Mg*. The International Journal of Advanced Manufacturing Technology**,** Vol 142. https://doi.org/10.1007/s00170-025-17344-3
69. UNI (2021). EN 1706 *Alluminio e leghe di alluminio - Getti - Composizione chimica e proprietà meccaniche,* Standard
70. MEP (2026). *SEMI-AUTOMATIC band sawing machines.* Online https://mepsaws.it/en/saws/semi-automatic-band-saws (Accessed: 23/11/2025)

71. Malvern Panalytical (2026) *Mastersizer 3000+ Malvern laser diffraction technology The smartest way to measure particle size* Online https://www.malvernpanalytical.com/en/assets/malvern_panalytical_mastersizer_3000_plus_brochure_pn14530_tcm50-103002.pdf (Accessed: 17/8/2026)
72. Junfeng W., Min X., Jialun W., et al. (2024). *Precise control of atomization initial stage to address nozzle clogging issue in the vacuum induction-melting gas atomization process*. Journal of Materials Research and Technology, Vol 30, Pages 1505-1517. https://doi.org/10.1016/j.jmrt.2024.03.095
73. Freeman Technology (2026). *About the FT4 Powder Rheometer® Powder Flow Testing with the FT4 Powder Rheometer*, Online website https://www.freemantech.co.uk/powder-testing/ft4-powder-rheometer-powder-flow-tester (Accessed: 10/5/2026)
74. Bourot P., Weiss L., Boisselier D., Laheurte P. (2024). *Effect of bimodal size distribution on the behavioural properties of powders used in the LPBF process.* Powder Technology, Vol 439, https://doi.org/10.1016/j.powtec.2024.119670.
75. EOS GmbH (2010). "Technical Description EOSINT M 280", Technical manual
76. Rafieazad M.et al. (2021). *Effects of Laser-Powder Bed Fusion Process Parameters on the Microstructure and Corrosion Properties of AlSi10Mg Alloy.* Journal of The Electrochemical Society*, Vol* 168, DOI:10.1149/1945-7111/abdfa8
77. Remet (2026). *IPA 30 - 40 - 50 – 60*. Online https://remet.it/en/products/ipa-30 (Accessed : 2/5/2026)
78. QATM (2024). *PRECISION CUT-OFF MACHINE BRILLANT 220*, Online https://www.qatm.com/files/104163/brillant-220.pdf (Accessed: 2/5/2026)
79. Leica (2026). *DMI5000 M Inverted Research Microscope for Materials Testing*. Online https://www.leica-microsystems.com/products/light-microscopes/p/leica-dmi5000-m/media/ (Accessed: 2/5/2026)
80. Mahanta T., Kumar S., Kanjilal D. *et al.* (2022). *Exploring the effect of varying regimes of ion fluence on the optical and surface electronic properties of graphene*. Applied Physics A, Vol 128. https://doi.org/10.1007/s00339-022-06051-5
81. Tescan (2026) *TESCAN S9000G: New generation of FIB-SEM microscope* Online https://www.atomikateknik.com/uploads/belgeler/s9000-g-brosur-32921.pdf (Accessed: 7/5/2026)
82. Callister W., Rethwisch D. (2018). *Materials Science and Engineering: An Introduction* Wiley, 10th edition, Pag 125. ISBN: 9781119405498
83. Schwartz A. J. et al (2009). *Electron Backscatter Diffraction in Materials Science.* 2nd ed., Springer,
84. Blue Powder Metallurgy (2025). *Vickers Hardness Test*. Online, https://powdermetallurgy.com/vickers-hardness-test/ (Accessed: 17/6/2026)
85. Made-in-China (2026). *Hvs-1000 Digital Micro Vickers Hardness Testing Machine*. Online, https://esttest.en.made-in-china.com/product/kOcAhkVWAbYz/China-Hvs-1000-Digital-Micro-Vickers-Hardness-Testing-Machine.html (Accessed: 17/6/2026)
86. EPMA (2026). *Metal Injection Moulding (MIM)*, Online website https://www.epma.com/what-is-pm/powder-metallurgy-process/metal-injection-moulding-mim/ (Accessed: 15/5/2026)
87. Marinucci F., Aversa A., Manfredi D., et al. (2022). *Evaluation of a Laboratory-Scale Gas-Atomized AlSi10Mg Powder and a Commercial-Grade Counterpart for Laser Powder Bed Fusion Processing*. Materials (Basel), Vol 15(21). DOI: 10.3390/ma15217565.
88. ThyssenKrupp AG (2018) *Powder Metals Additive Manufacturing*. Online website https://ucpcdn.thyssenkrupp.com/_legacy/UCPthyssenkruppBAMXSchweiz/assets.file

s/loesungen/additive-manufacturing/033_additive_manufacturing_powder_metals.pdf (Access: 15/7/2026)
89. Goodge J. (2007). *Energy-Dispersive X-Ray Spectroscopy (EDS)*. Integrating Research and Education
90. Li M., Leturia M., Saleh K. (2018). *Analysis of the Periodic Motion in a Powder Rheometer and Development of a New Flowability Testing Method* KONA Powder and Particle Journal, Vol 35 https://doi.org/10.14356/kona.2018002
91. ASTM (2021). *ASTM F3049-14 Standard Guide for Characterizing Properties of Metal Powders Used for Additive Manufacturing Processes*. Standard. DOI**:** 10.1520/F3049-14R21
92. Goldstein J., Newbury D., Michael J., et al. (2017) *Scanning Electron Microscopy and X-Ray Microanalysis*, Springer New York, 4th edition https://doi.org/10.1007/978-1-4939-6676-9
93. Murakami Y. (2019). *Metal Fatigue: Effects of Small Defects and Nonmetallic Inclusions*. Academic Press, 2nd edition. DOI: 10.1016/C2016-0-05272-5
94. Hyer H., Zhou L., Park S. et al. (2020) *Understanding the Laser Powder Bed Fusion of AlSi10Mg Alloy*. Metallography, Microstructure, and Analysis, Vol. 9, https://doi.org/10.1007/s13632-020-00659-w
95. Rehman A., Mahmood M. A., Ansari, P., et al. (2021). *Spatter Formation and Splashing Induced Defects in Laser-Based Powder Bed Fusion of AlSi10Mg Alloy: A Novel Hydrodynamics Modelling with Empirical Testing*. Metals, Vol 11(12). https://doi.org/10.3390/met11122023
96. Argyrou A., Gargalis L., Karavias L., et al. (2026). *LPBF AlSi10Mg at the Nanoscale: A Critical Review of Processing–Microstructure–Property Correlations via Nanoindentation*. Applied Sciences, Vol *16*(6). https://doi.org/10.3390/app16062730
97. Huang Y., Fleming T.G., S.J. Clark, et al. (2022) *Keyhole fluctuation and pore formation mechanisms during laser powder bed fusion additive manufacturing*. Nature Communications, Vol 13. https://doi.org/10.1038/s41467-022-28694-x.
98. Brennan M.C., Keist J.S. and Palmer T.A. (2021). *Defects in Metal Additive Manufacturing Processes.* Journal of Material Engineering and Performance, Vol 30, 4808–4818 (https://doi.org/10.1007/s11665-021-05919-6
99. Alghamdi F., Song X., Hadadzadeh A., et al. (2020). *Post heat treatment of additive manufactured AlSi10Mg: On silicon morphology, texture and small-scale properties*. Materials Science and Engineering: A , Vol 783 https://doi.org/10.1016/j.msea.2020.139296.
100. DebRoy T., Wei H.L., Zuback J.S., et al. (2018). *Additive manufacturing of metallic components – Process, structure and properties* Progress in Materials Science, Vol 92, pag 112-224 https://doi.org/10.1016/j.pmatsci.2017.10.001.
101. Fiocchi J., Tuissi A., Biffi C.A. (2021) *Heat treatment of aluminium alloys produced by laser powder bed fusion: A review* Materials & Design, Vol 204, https://doi.org/10.1016/j.matdes.2021.109651.
102. Beder M., Akçay S.B. Varol, T. et al (2024). *The Effect of Heat Treatment on the Mechanical Properties and Oxidation Resistance of AlSi10Mg Alloy*. Arabian Journal for Science and Engineering**,** Vol 49, 15335–15346 https://doi.org/10.1007/s13369-024-08971-1
103. Sarkar A.D., Clarke J. (1980). *Friction and wear of aluminium-silicon alloys*. Wear, Vol 61, 157–167 https://doi.org/10.1016/0043-16 48(80)90120-9
104. Jasim K.M., Dwarakadasa E.S. (1987). *Wear in Al–Si alloys under dry sliding conditions*. Wear, Vol 119, 119–130 https://doi.org/10. 1016/0043-1648(87)90102-5

105.Dwivedi D.K. (2010). *Adhesive wear behaviour of cast aluminium–silicon alloys: overview*. Materials & Design, Vol 31, 2517–2531. https:// doi.org/10.1016/j.matdes.2009.11.038 8.
106.Ye H. (2003). *An overview of the development of Al–Si-alloy based material for engine applications*. Journal of Materials Engineering and Performance, Vol 12, 288–297 https://doi.org/10.1361/105994903770343132
107.Tillov E., Chalupov M. and Hurtalov L. (2012). *Evolution of Phases in a Recycled Al-Si Cast Alloy During Solution Treatment*. Scanning Electron Microscopy. doi:10.5772/34542.
108.Krupiński M., Labisz K., Rdzawski Z., Pawlyta M. (2011) *Cooling rate and chemical composition influence on structure of Al-Si-Cu alloys*. Journal of Achievements in Materials and Manufacturing Engineering, Vol 45
109.Tillova E., Chalupova M. (2009) *Structural analysis of Al-Si cast alloys*. EDIS Žilina
110.Shabestari S.G. (2004) *The effect of iron and manganese on the formation of intermetallic compounds in aluminum–silicon alloys* Materials Science and Engineering: A, Vol. 383, https://doi.org/10.1016/j.msea.2004.06.022
111. J.L. Jorstad 81986) *Understanding sludge* Die casting engineer*,* Vol. 30, pp. 30–36.
112.Snopiński, P. (2024). *Effects of KoBo-Processing and Subsequent Annealing Treatment on Grain Boundary Network and Texture Development in Laser Powder Bed Fusion (LPBF) AlSi10Mg Alloy*. Symmetry, Vol 16(1). https://doi.org/10.3390/sym16010122
113.Snopiński, P., Kotoul, M., Petruška, J. et al (2023). *Revealing the strengthening contribution of stacking faults, dislocations and grain boundaries in severely deformed LPBF AlSi10Mg alloy.* Scientific Reports, Vol 13. https://doi.org/10.1038/s41598-023-43448-5
114.Hull D., Bacon D.J., (2011). *Introduction to Dislocations (Fifth Edition)," Chapter 10 - Strength of Crystalline Solids*, Butterworth-Heinemann, Pages 205-249, https://doi.org/10.1016/B978-0-08-096672-4.00010-4.
115.Fousova M., Dvorsky D., Vronka M., et al. (2018). *The use of Selective Laser Melting to increase the Performance of AlSi9Cu3Fe Alloy*, Materials, Vol. 11 https://doi.org/10.3390/ma11101918.
116.Carlton H., Haboub A., Gallegos G., et al. (2016) *Damage evolution and failure mechanisms in additively manufactured stainless steel*, Materials Science and Engineering: A, Vol 651, Pages 406-414, https://doi.org/10.1016/j.msea.2015.10.073.
117.DebRoy T., et al. (2018)**.** *Additive manufacturing of metallic components – Process, structure and properties.* Progress in Materials Science**,** Vol 92,pag 112–224. https://doi.org/10.1016/j.pmatsci.2017.10.001
118.Zuback J. S., DebRoy, T. (2018). *The Hardness of Additively Manufactured Alloys.* Materials, vol 11(11). https://doi.org/10.3390/ma11112070
119.Takata N., Kodaira H., Sekizawa K., et al. (2017) *Change in microstructure of selectively laser melted AlSi10Mg alloy with heat treatments*. Materials Science and Engineering: A, Volume 704, Pages 218-228, https://doi.org/10.1016/j.msea.2017.08.029.
120.Xihe L., Congcong Z., Xin Z., et al. (2019) *Microstructure of selective laser melted AlSi10Mg alloy*," Materials & Design, Vol 168, https://doi.org/10.1016/j.matdes.2019.107677.
121.Ansys, Inc (2025) Granta Software, Edu Pack 2025 revision 2.0
122.Wang, Z., Ummethala R., Singh N., et al. (2020). *Selective Laser Melting of Aluminum and Its Alloys*. Materials, Vol *13*(20). https://doi.org/10.3390/ma13204564

123.Snopiński, P., Król, M., Pagáč, M. et al. (2021). *Effects of equal channel angular pressing and heat treatments on the microstructures and mechanical properties of selective laser melted and cast AlSi10Mg alloys.* Archives of Civil and Mechanical Engineering, Vol 21. https://doi.org/10.1007/s43452-021-00246-y
124.Maeshima T., Oh-ishi K., Kadoura H. (2024). *Microstructural evolution and hardening phenomenn caused by aging of AlSi10Mg alloy by laser powder bed fusion*. Heliyon, Vol 10 (6), https://doi.org/10.1016/j.heliyon.2024.e28006
125.Ramesh R., Gairola S., Jayaganthan R., Kamaraj M.(2026). *Microstructural evolution, mechanical behaviour and strengthening mechanisms of additively manufactured AlSi9Cu3 alloy* Journal of Materials Research and Technology, Vol 40, Pages 1738-1752, https://doi.org/10.1016/j.jmrt.2025.12.221.
126.Fiocchi J., Colombo C., Vergani L. M., et al. (2021). *Heat Treatments for Stress Relieving AlSi9Cu3 Alloy Produced by Laser Powder Bed Fusion*. Materials, Vol *14*(15), 4184. https://doi.org/10.3390/ma14154184
127.Vašákováa K., Judasa J., Čuperaa J., Pantělejeva L., Koutnýa D. (2025). *Effects of heat treatment on microstructure and mechanical properties of LPBF AlSi9Cu3 alloy* Eleventh International Conference on Materials Structure and Micromechanics of Fracture, https://doi.org/10.1016/j.prostr.2025.10.040
128.Fabrizi A., Capuzzi S., De Mori A., Timelli G. (2018). *Effect of T6 Heat Treatment on the Microstructure and Hardness of Secondary AlSi₉Cu₃(Fe) Alloys Produced by Semi-Solid SEED Process*. Metals, Vol 8(10). https://doi.org/10.3390/met8100750
129.Tonelli L., Martucci A., Lagalante I. et al. (2026). *Study on aging and overaging behavior of the AlSi9Cu3 alloy processed by PBF-LB*. Journal of Materials Science, Vol 61, Pag 26474–26496 https://doi.org/10.1007/s10853-026-13203-y
130.Kristýna Vašáková, Jakub Judas, Jan Čupera, Libor Pantělejev, Daniel Koutný, (2025) "Effects of heat treatment on microstructure and mechanical properties of LPBF AlSi9Cu3 alloy," Procedia Structural Integrity, Volume 74, https://doi.org/10.1016/j.prostr.2025.10.040.
131.Megahed S., Bühring J., Duffe T., et al. (2022). *Effect of Heat Treatment on Ductility and Precipitation Size of Additively Manufactured AlSi10Mg.* Metals, Vol 12(8), 1311. https://doi.org/10.3390/met12081311
132.Merino J., Ruvalcaba B., Varela J., et al. (2021) *Multiple, comparative heat treatment and aging schedules for controlling the microstructures and mechanical properties of laser powder bed fusion fabricated AlSi10Mg alloy* Journal of Materials Research and Technology, Vol13, https://doi.org/10.1016/j.jmrt.2021.04.062.
133.Kempf A., Hilgenberg K. (2021). *Influence of heat treatments on AlSi10Mg specimens manufactured with different laser powder bed fusion machines*," Materials Science and Engineering: A, Vol 818, https://doi.org/10.1016/j.msea.2021.141371.
134.Hitzler L., Hafenstein S., Mendez M. F., et al. (2020). *Heat Treatments and Critical Quenching Rates in Additively Manufactured Al-Si-Mg Alloys*. Materials (Basel), Vol 13(3). DOI: 10.3390/ma13030720